SNOWMELT RUNOFF PROCESSES IN A SUBARCTIC AREA

by

Anthony G. Price

A dissertation submitted to the Faculty of Graduate Studies

and Research, McGill University, in partial fulfilment of the

requirements for the degree of Doctor of Philosophy.

Department of Geography   March 1975

McGill University

Montreal, Quebec

SNOWMELT RUNOFF PROCESSES IN A SUBARCTIC AREA

A.G. Price

Doctor of Philosophy

ABSTRACT

The study attempts to define the physical processes involved
in the generation of daily snowmelt hydrographs in Subarctic boreal
forest and on the tundra, near Schefferville, P.Q. Melting at the
surface of the snowpack is predicted using a physically based heat-
flow, or energy balance, model. Correspondence between observed
daily flows and daily predicted heatflow totals confirms the accuracy
of the energy balance approach.

Surface melt predicted on an hourly basis, using the energy
balance approach, is then routed down through the snowpack to the
ground as unsaturated flow, and subsequently along the ground in a
thin saturated layer. The similarity of observed hydrographs and
those predicted using the model suggest that the theory of water
flow through snow is a realistic one.

A. G. Price

Docteur en Philosophie

Département de Géographie
Université McGill
Montréal, Québec

Résumé

Les processes de fonte nivale dans une région subartique

L'étude cherche a apprehender les processes physique responsables de la forme des hydrogrammes de fonte nivale fournalière dans la forêt boréale et sur la toundra près de Schefferville, P.Q. Un modèle de flux thermique, on bilan énergétique, établi sur des bases physiques, sert a la prévision de la fonte à la surface de la neige. La correlation entre les debits d'eau de fonte observés, et les flux thermiques totaux prévus pour chaque jour confirme la précision de l'approche fondée sur la bilan energetique.

Un fois que ce model de flux thermique a évalué, sur une base horaire, la quantité d'eau de fonte en surface de la couverture nivale, un modèle d'écoulement liquide à travers le banc de neige assume que l'eau percole à travers la neige vers le sol sous forme d'écoulement non-saturé, puis au contact du sol sous forme d'une mince pellicule d'écoulement saturé. La similarité entre les hydrogrammes observés et ceux produits d'après le modèle suggère que la theorie d'écoulement liquide a travers la neige est vraisemblable.

This study is part of an overall snowmelt hydrology program undertaken at McGill Subarctic Research Laboratory, a designated International Hydrological Decade Station. The main snowmelt work was undertaken in the Springs of 1972 and 1973. The purpose of the study was to elucidate snowmelt processes at three different scales. The present study was at the most detailed level, that of hillsides in different situations of inclination, aspect, and cover type. John Fitzgibbon and Stan Matthewson carried out parallel studies at the basin and inter-basin scale, respectively. Dr. R. G. Wilson and Don Petzold studied the radiation balance in the forest, and supplied the bulk of the radiation data used in this thesis.

The original contribution of this study is in the application of physical modelling to both the prediction of daily and hourly melt rates, and to the prediction of daily slope snowmelt hydrographs resulting form diurnal snowmelt cycles. Within the prediction of rates of snowmelt, the corrections for the effects of the stability of the air over the snow on turbulent exchanges are applied, and are shown to be of great importance in the Schefferville environment. Within the hydrograph prediction, a model of porous-medium flow is tested for the first time, and is shown to be a good representation of the processes involved in hydrograph formation. The study is, to the author's knowledge, the most complete snowmelt study to date, since it treats

the whole process of snowmelt, from melting at the surface to discharge from the slope base. In order to perform this study, data were collected on a 24 hour basis for two field seasons. The data are very extensive, and unusual, particularly in the completeness of the runoff and meteorological records.

TABLE OF CONTENTS

- v -

LIST OF FIGURES

LIST OF TABLES

SYMBOLS		UNITS
A	Area of unit	cm^2
A'	Slope area	cm^2
a	Albedo or reflectivity	
a'	Regression constant	
b	Regression constant	
C_1	Constant	
C_2	Constant	
C_3	Constant	
C'	Constant	
C''	Constant	
C_p	Specific heat of air at constant volume	$cal/gm/^{o}C$
C_s	Velocity of travel in the saturated layer	cm/hr
C_w	Specific heat of water	$cal/gm/^{o}C$
c	Mean zenith path transmissivity	
D_h	Transfer coefficient for heat	cm/hr
D_m	Transfer coefficient for momentum	cm/hr
D_w	Transfer coefficient for water vapour	cm/hr
d	Molecular diffusivity of water vapour in air	cm^2/hr
$(\frac{dz}{dt})_{v_w}$	Rate of vertical propagation of a constant flux rate v_w	cm/hr
$d\theta/dz$	Ground heat gradient	$^{o}C/cm$
$d\xi/dt$	Rate of propagation of shock front	cm/hr
e_a	Vapour pressure of the air	mb
e_s	Vapour pressure of the surface	mb
g	Gravitational constant	cm/hr^2

H_c	Sensible heat flow	$cal/cm^2/hr$
H_e	latent heat flow	$cal/cm^2/hr$
H_g	Ground heat flow	$cal/cm^2/hr$
H_m	Heat available for snowmelt	$cal/cm^2/hr$
H_p	Precipitation heat flow	$cal/cm^2/hr$
H_R	Radiation heat flow	$cal/cm^2/hr$
H_{Ro}	Net allwave radiation in the open	$cal/cm^2/hr$
H_{Rf}	Net allwave radiation in the forest	$cal/cm^2/hr$
H_θ	Heat deficit	cal/cm^2
$(H_c)_{neut}$	Sensible heat flow under neutral conditions	$cal/cm^2/hr$
$(H_c)_{stable}$	Sensible heat flow under stable conditions	$cal/cm^2/hr$
h_1	thickness of saturated layer	cm
h_2		
$h*$	Effective obstacle height	cm
I	Vertical input to saturated layer	$cm^3/cm^2/hr$
I_o	Total incoming shortwave radiation on horizontal surface at the outer edge of the atmosphere	$cal/cm^2/hr$
I_m	Value of direct beam radiation on horizontal	$cal/cm^2/hr$
I_s	Slope value of direct solar radiation	$cal/cm^2/hr$
I_{od}	Direct shortwave radiation on a horizontal surface at the outer edge of the atmosphere	$cal/cm^2/hr$
K_g	Ground thermal conductivity	$cal/hr/^{o}C/cm$
K_h	Eddy diffusivity for heat in air	cm^2/hr
K_m	Eddy diffusivity for momentum in air	cm^2/hr
K_w	Eddy diffusivity for water vapour in air	cm^2/hr
k	von Karman's constant	
k_h	Molecular diffisivity of heat in air	cm^2/hr

k_s	Permeability of saturated layer	cm^2
k_w	Permeability of snow at saturation S^*	cm^2
k'	Permeability of unsaturated layer at $S^* = 1.0$	cm^2
L	Latent heat of vapourisation of water	cal/gm
L_n	Net longwave Balance	$cal/cm^2/hr$
L_s	Length of saturated path (slope length)	cm
$L\downarrow$	Sky-emitted longwave radiation	$cal/cm^2/hr$
m	Optical air mass	
N	Sample number	
n	Constant	
P_r	Precipitation intensity	cm/hr
P_w	Pressure in the water phase	gm/cm^2
p	Barometric pressure	mb
Q	Direct solar radiation	$cal/cm^2/hr$
q	Diffuse solar radiation	$cal/cm^2/hr$
q_a	Specific moisture of air	gm/gm
q_s	Specific moisture of surface	gm/gm
Ri	Bulk Richardson number	
RH_a	Relative humidity derived from Assman psychrometer	$\%$
RH_L	Relative humidity from thermohygrograph	$\%$
r	Correlation coefficient	
r^2	Correlation explanation	
S	Silhouette area	cm^2
S'	Basal area	cm^2

S''	Unit coordinate vector expressing height and position of sun	
S_c	Solar constant	$cal/cm^2/hr$
S_w	Actual saturation	
S_{wa}	Absorbed shortwave radiation	$cal/cm^2/hr$
S_{wi}	Irreducible water saturation	
$S*$	Effective saturation	
$S\uparrow$	Snow-emitted longwave radiation	$cal/cm^2/hr$
T_a	Air temperature	^oC
T_s	Surface (snow) temperature	^oC
T_w	Wet-bulb temperature	^oC
T_{aA}	Temperature from Assman psychrometer	^oC
T_{aL}	Temperature from thermohygrograph	^oC
T_{abs}	Absolute temperature	^oK
t'	Time	hr
t'_o	Initial time	
t'_L	Total travel time in the saturated layer	hr
u_z	Windspeed at height z	cm/hr
u_*	Friction velocity	cm/hr
u_-	Lower flux level in shock front	cm/hr
u_+	Upper flux level in shock front	cm/hr
v_1	Flux rates	$cm^3/cm^2/hr$
v_2		
v_s	Volume flux in saturated layer	$cm^3/cm^2/hr$
v_w	Volume flux of water in unsaturated layer	$cm^3/cm^2/hr$

W	Monin-Obuchov stability length	cm
X'	Unit coordinate vector orthogonal to slope	
x'	Moving coordinate system	
z	Height of measurement	cm
z_o	Roughness length	cm
α	Constant	
β	Slope inclination	o
Δ	Declination of sun	o
ΔT	Increment in temperature over height Δz	^oC
Δt	Change in time.	hr
Δu	Increment in windspeed over height Δz	cm/hr
Δx	Width of unit	cm
$\Delta T/\Delta z$	Gradient of air temperature with height within the boundary layer	$^oC/cm$
$\Delta q/\Delta z$	Gradient of specific moisture with height within the boundary layer	gm/gm/cm
$\Delta u/\Delta z$	Gradient of velocity with height within the boundary layer	cm/hr/cm
μ	Viscosity of water	gm/ hr/cm
ν	Kinematic viscosity of air	cm^2/hr
ρ_a	Density of air	gm/cm^3
ρ_i	Density of ice	gm/cm^3
ρ_s	Density of snow	gm/cm^3
ρ_w	Density of water	gm/cm^3
ΣRO	Sum of daily runoff	litres
σ	Constant	
σ'	Stephan-Boltzman constant	$cal/cm^2/hr/^oK^4$

σ_e	Standard error of the estimate	
τ	Shear stress	dynes/cm^2
$\emptyset$	Total porosity	
$\emptyset_e$	Effective porosity	
ψ	Latitude	o
Ω	Hour angle	o

CHAPTER 1

INTRODUCTION

The Study

This study is concerned with the analysis, understanding, and prediction of snowmelt runoff hydrographs generated by diurnal melt cycles on hillside plots located in subarctic lichen woodlands and tundra. The aim of the study is to compute hourly melt rates from the energy balance of the snowpack, and then to predict slope hydrographs by routing the computed meltwater wave down through the snowpack, and along the ground to the base of the hillslope. The theoretical predictions are then tested against field measurements of melt and of runoff hydrographs.

The primary justification for the study is the lack of precise quantitative knowledge of the factors controlling the generation of snowmelt hydrographs, and the lack of efforts to analyse them. There is a lack of good working models for hourly and daily snowmelt prediction based on physical principles. The relative magnitudes of the various controls and their interaction are particularly poorly understood. Numerous statistical and index methods of prediction exist, but few have an adequate physical base. Other works, such as that of the U.S. Army Corps of Engineers (1956), are more soundly based on physical principles, but still fall short of an adequate treatment of the processes of heat exchange between the snowpack and its environment. Earlier works are reviewed in Chapter 2.

No work has been attempted which combines melt prediction with the routing of meltwater through the snowpack on a rigorous physical basis. The present study does this, and also tests predictions against field observations. The study was carried out in two different environments: boreal forest and tundra. In both of these environments measurements were made on several hillslopes with differing gradients and aspects.

Apart from the academic justifications, it is obvious that in an area such as the subarctic where hydroelectric power is being developed, a knowledge of the mechanisms by which runoff is produced from a snowpack is of great practical importance.

Field Area for the Study

The study area is in the vicinity of Schefferville, P.Q. There are two main reasons for the choice of area. First, there are sound economic reasons for work on snowmelt runoff prediction in the subarctic. Second, the snowfall in the Schefferville area is heavy (about 35 cm water equivalent per annum). This heavy snowfall, combined with a thaw which is swift and predictable within a few weeks make data collection much easier than areas to the south with less snow and more variation in the time of thaw. In the Schefferville area, the occurrence of winter thaws is most unusual. The structure of the snowpack is almost completely uniform, and ice layers are exceptional. This is an advantage for a first attempt at modelling the vertical percolation of water through a snowpack. In the three years of field work, no winter melt occurred.

Another factor favouring research in the area is that the ground
usually freezes to a considerable depth during the fall, while the
soil is wet. The ground remains frozen under the snowpack until
late in the thaw, when snow has melted from most of the area. The
frost is of the "concrete" type (Post and Dreibelbis, 1942), and the
impermeability of the frozen soil makes the computation of a water
balance simpler, since infiltration of water into the soil has been
eliminated.

Physical Geography of the Study Area

The Schefferville region is within the structural-geologic unit
known as the Labrador Trough, which consists of a belt of Proterozoic
rocks trending roughly north-northwest to south-southeast. The Pro-
terozoics lie unconformably on the Archean basement, and
have been intensely folded and thrusted by pressure from the northeast.
As a result of cross-faulting, the stratigraphic sequence is repeated
many times across the trough. A common repetition is: iron formation,
slate, dolomite, chert breccia and quartzite, all with northerly dips.
The topography is related closely to the structure. Strike ridges of
the more resistant quartzites, dolomites and slates form elongate ridges,
while the valleys are underlain by the less resistant slates, dolomites,
and iron formation.

Local relief within the basin is generally less than 200 m. The
most extreme relief differences in the area, between the bottoms of
valleys and the highest ridges is in the order of 600 m.

One group of experimental sites used in this study is situated in an area of boreal forest just outside the Knob Lake drainage basin (see Figure 1.1). This basin is one of the International Hydrological Decade experimental watersheds. Another group of three sites is situated on the tundra some 22 km from the Schefferville townsite. Schefferville, at the outlet of the drainage basin is at 536 m.a.s.l. Knob Lake (within the townsite) is near the maximum height of land between the Altantic and Hudson's Bay drainage systems. The lake drains northwards to Ungava Bay, through the Kaniapiskau-Koksoak system. The Howells River, and lakes in the Schefferville depression drain southwards to the Atlantic via the Ashuanipi-Hamilton (Churchill Falls) system.

The drainage system is irregular because of the cover of till deposited by Pleistocene glaciers. On the ridges surrounding the Schefferville depression, till is very thin (less than 1 m), or non-existent, whereas in the depression it is thicker (2 - 10 m). The slopes on which the study was performed reflect the general pattern of till distribution, having generally thicker till cover at their bases than at their tops. The small-scale irregularity of the till cover combined with the form of underlying bedrock gives the slopes a generally stepped appearance (see Figures 5.3 and 5.7). Some of the valleyside slopes have glacial meltwater channels cut into them, but since these channels are usually approximately at right angles to the slope direction, they seldom form channels for present drainage.

basin outlet

FIGURE 1.1

Lakes

basin limits

1 km

Scale

LABRADOR-UNGAVA PENINSULA

N

SCHEFFERVILLE

0   50   100 m!s
0   50   160 kms
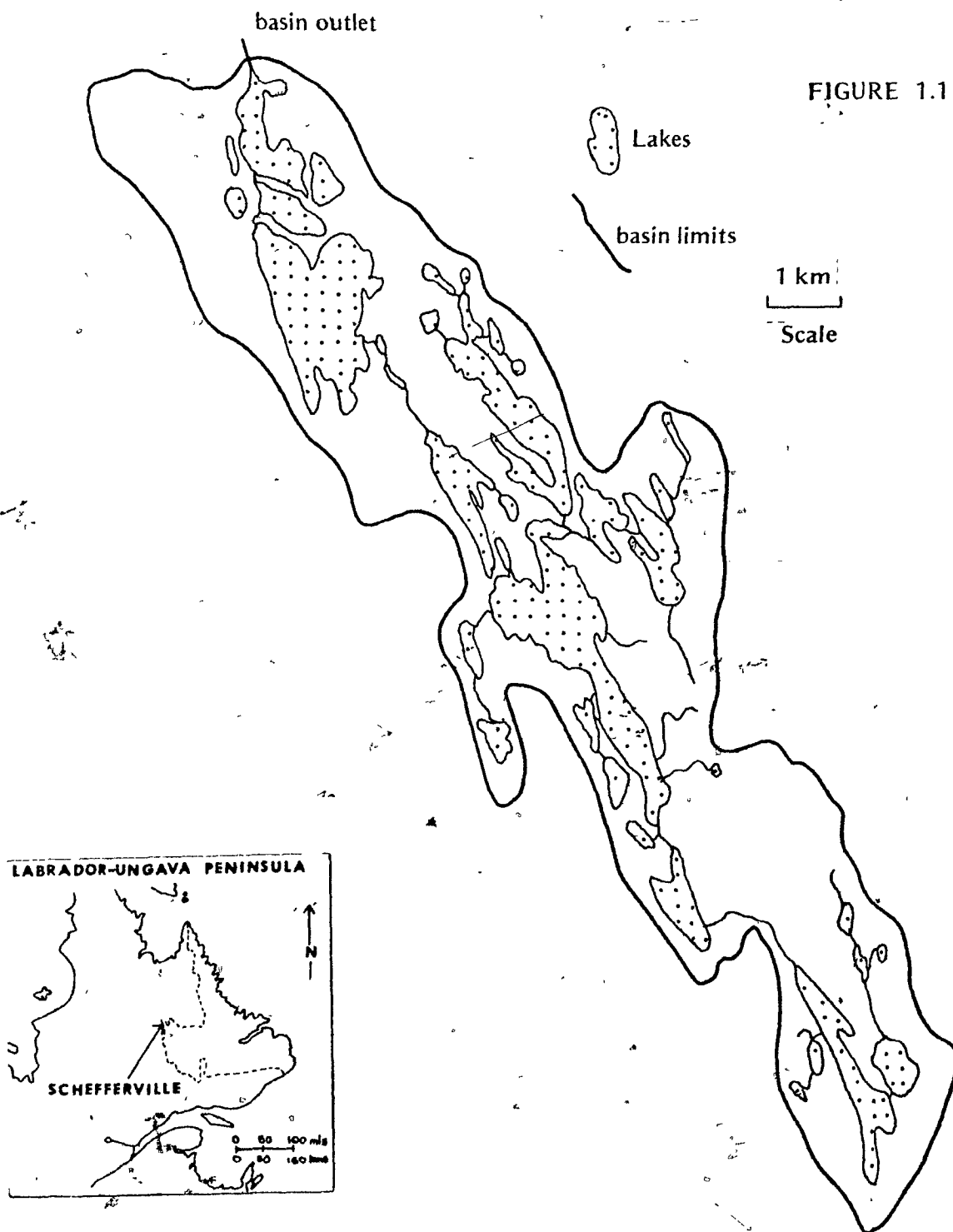
Location of Schefferville.

The Knob Lake Drainage Basin

The climate of the area is typical of the Eastern Canadian
subarctic type, with only the months of July and August having mean
temperatures above 10°C. The annual mean temperature is -4.7°C.
May and June are the months when mean temperatures first rise above
freezing. Most nights in May have frost, but in June this occurs
on only 25 percent of the nights. Annual snowfall in the area is in
the order of 35 cm water equivalent, with a record high of 41 cm in
1969, and a record low of 27.2 cm in 1960. Snow usually forms almost
half of the 74 cm average annual precipitation in the area. The
weather record at Knob Lake extends from 1955 to the present (1974),
and a summary of the relevant parameters is given in Figure 1.2.

The area lies between two vegetation zones: the lichen woodlands,
(see Figure 1.3) and the tundra (see Figure 1.4). Since the local
limit of tree growth is at about 750 m. a.s.l/, the tundra occurs on
high ridgetops, and forest covers the lower hillslopes and valleys
(see Figure 1.5). The tundra vegetation includes some dwarf spruce
but is essentially treeless. In the lower wooded areas, the forest
varies in density, and may be classified into closed crown lichen wood-
land and open lichen woodland. The latter is the dominant type. The
average canopy cover for open lichen woodland is approximately 15 per-
cent; while closed lichen woodland has a crown cover of up to 100 per-
cent. Both within the basin and around it, a commonly occurring vegetation
type is regenerating burnt areas. Figure 1.6 shows a typical burn. No
investigation of snowmelt was made in these burnt areas, which are very
similar to the tundra type. Fitzgibbon (in press) makes a comparison of
average daily melt rates in various cover types, including burn.

FIGURE 1.2
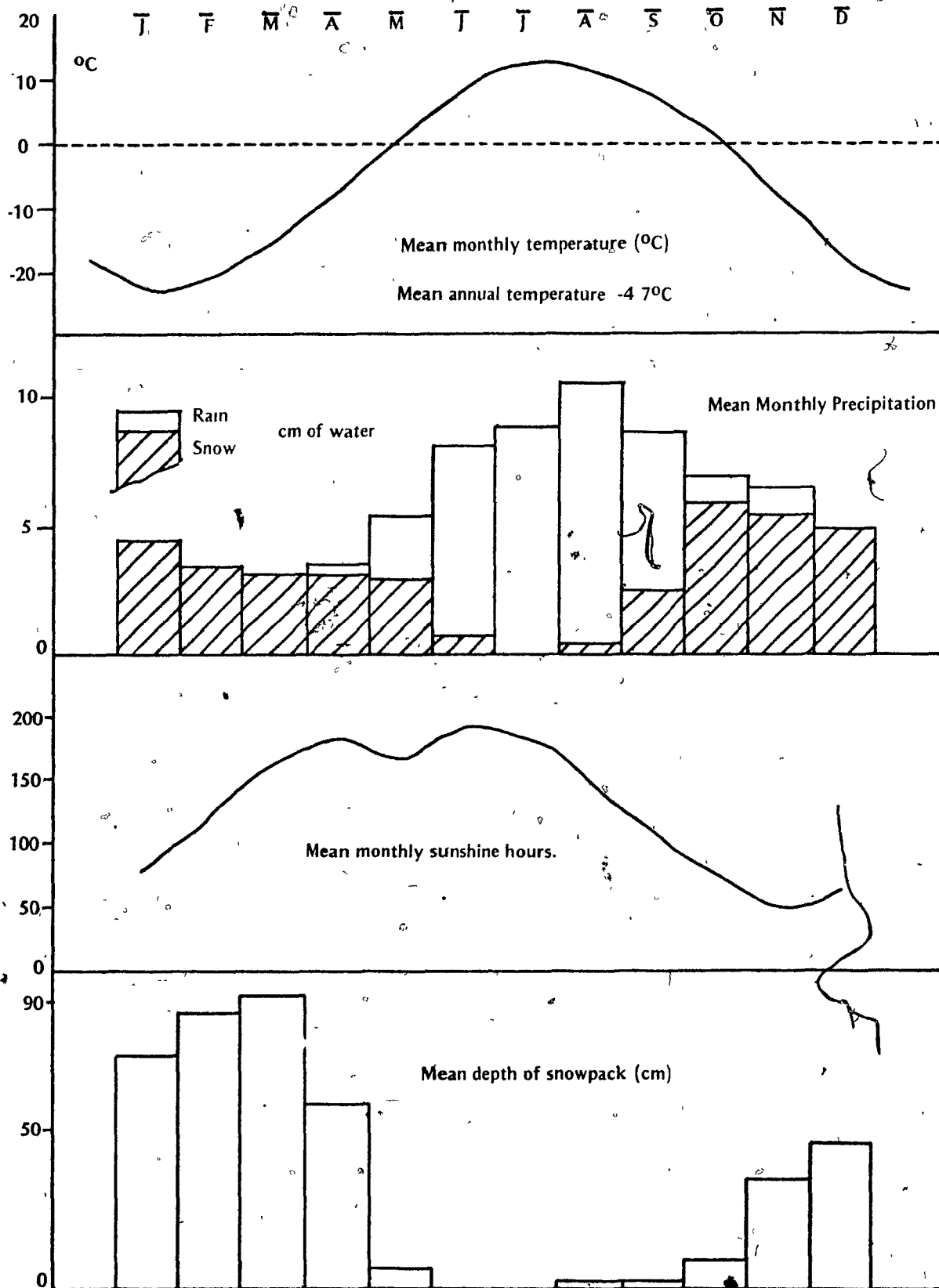
Summary Of Schefferville Meteorological Parameters, 1954–1974

Photograph of woods sites area

This photograph was taken before the excavation of the trench
on Site 'E'. Note the lichen mat and alder underbrush.

Photograph of tundra sites area

The tundra can be seen on the ridge-top in the foreground, and the one in the background. In the valley between the ridges, forest can be seen.

FIGURE 1.4

General aerial view of the basin

This view of the basin was taken from the south. The Scheffer-
ville townsite can be seen in the upper left of the photograph.

FIGURE 1.5

FIGURE 1.6
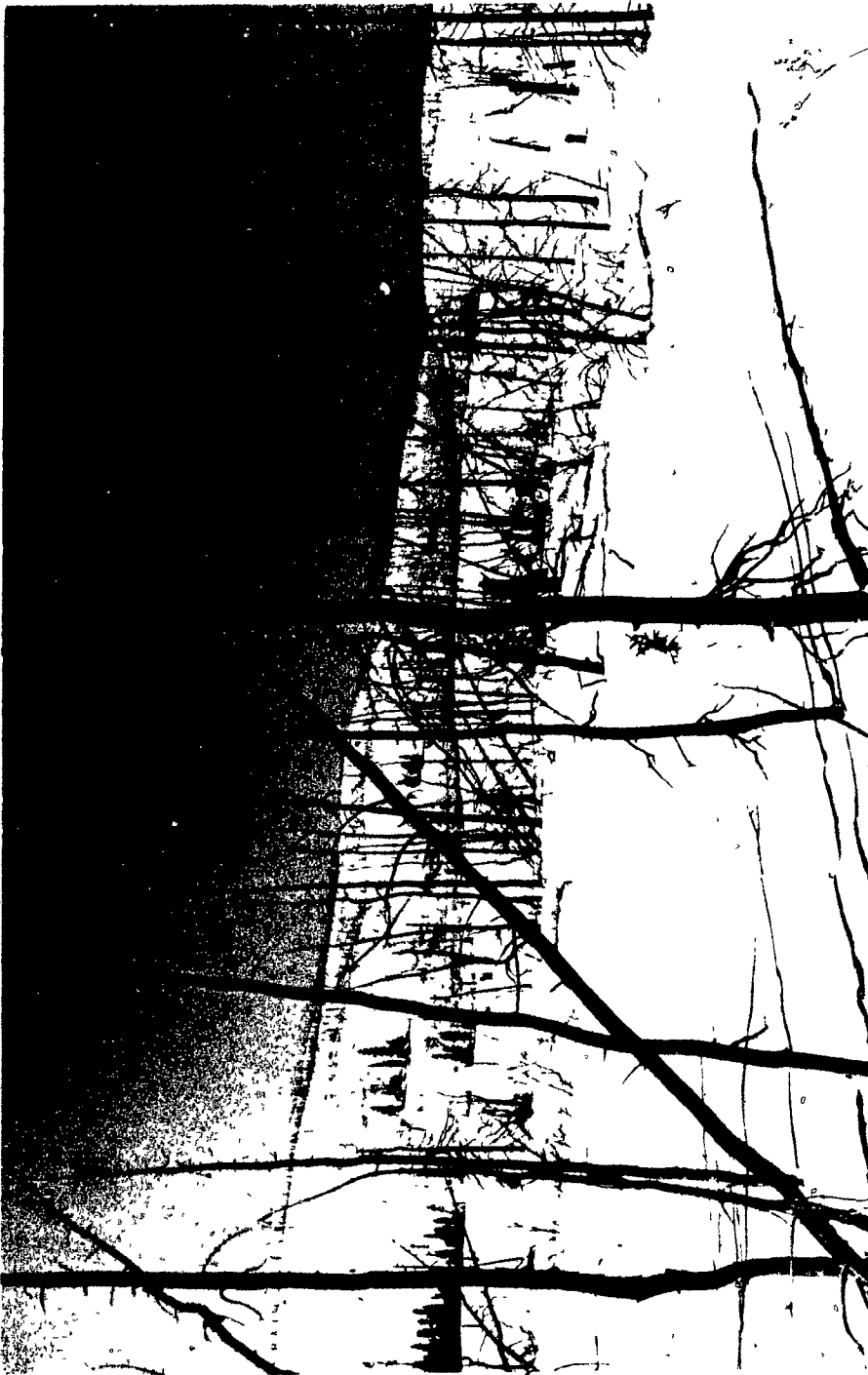
Typical burnt-over area

A description of the soils of the area and their hydrological properties is given in the section on detailed site descriptions, in Chapter 5.

CHAPTER 2

REVIEW OF PREVIOUS WORK

There are two problems in predicting snowmelt runoff:

a) the melting of the snow at the surface of the snowpack has to be considered; and b), runoff resulting from this melt has to be predicted.

Previous Work on Snowmelt

This section is not meant to be a comprehensive literature review. Rather than consider the whole history of snowmelt studies, different types of model will be considered in order of increasing sophistication.

Conceptually the simplest type of snowmelt model is termed the index method. This also is the oldest and most commonly used method. Some index of the heat budget is computed and regressed against whatever aspect of snowmelt is of interest. The most usual combination (see Figure 2.1) is to regress daily melt, measured by either total daily runoff or snowstake measurements of melt, against the number of degree-days, defined as the difference between the mean daily air temperature and some base temperature (often 0°C.), (Collins, 1934). Then future predictions of melt are made using the regression equation with an estimate of the degree-day total for the future season or day. The next most sophisticated type of technique involves the use of multiple regression with daily snowmelt as the dependent variable, and the components of the energy budget as the independent variables. This approach

FIGURE 2.1

Mean Daily Temperature versus Daily Runoff, Forest Sites 1973.
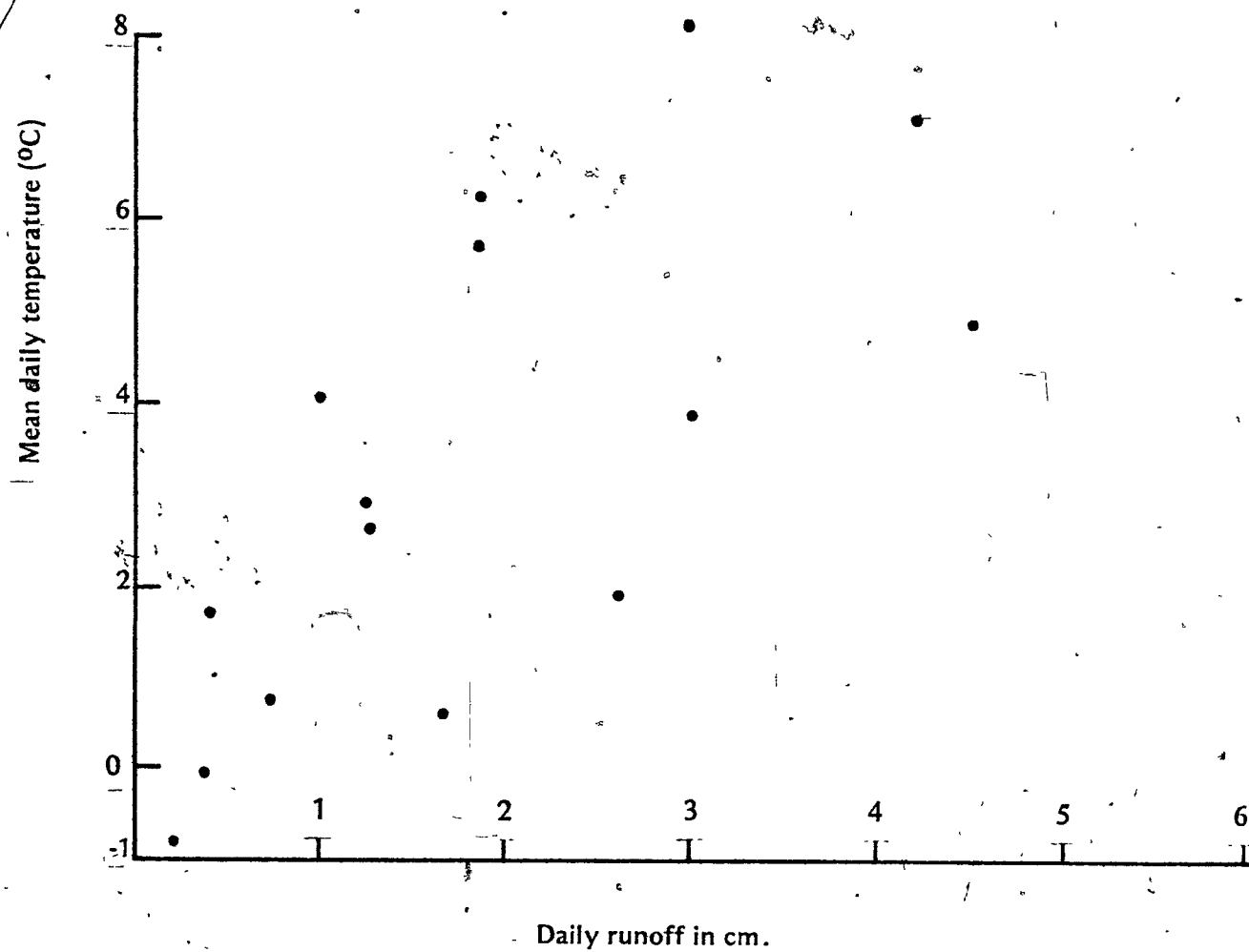
is used by Pysklywec, Davar and Bray (1968) who use as independent variables measures of net radiation, vapour pressure, windspeed and air temperature.

The number of variables considered increases still further in the work of the U.S. Army Corps of Engineers (1956), which treats the physics of the heat budget. The physical theory employed, however, involves many approximations, especially in the treatment of the turbulent exchanges of energy between the snow and the atmosphere. Although an attempt is made at a satisfactory physical treatment, some of the basic assumptions made by the authors in the development of the theory of turbulent exchange are unrealistic, and prevent a full treatment of the processes involved. The failure of this work to deal adequately with the physical theory is particularly unfortunate in view of the fact that this is one of a very few studies that involve substantial testing of theory against field measurements of snowmelt. Failure to test theory against observation has been persistent throughout the last 20 years of snowmelt and snowmelt runoff work. Workers, such as Wilson (1941), who made significant theoretical contributions on the thermodynamics of snowmelt, often did not test theory against field data.

Physically the most complete approach to predicting snowmelt (Wilson, 1941; Anderson, 1968; Fohn, 1973) is to define all the exchanges of heat between the ground, atmosphere, surrounding vegetation and snow. The most satisfactory study of this type to date is that of Anderson (1968). Anderson tests his equations against measurements of

water draining from the snowpack into a lysimeter, but since runoff and energy balance are measured at widely separated points, good testing of the melt prediction of the equations is difficult. In addition, Anderson does not consider the question of the damping of atmospheric turbulence by the development of conditions of stable stratification over the snow surface. Nevertheless, this paper, together with that of Fohn (1973) stand as the most successful attempts to date at a complete statement of the snowmelt problem. Fohn compares melt predicted by the energy balance equations with melt collected in a lysimeter. The scale of the study however, is very small. His lysimeter was approximately 50 cm in diameter, and consisted of a container set under the snow surface. Runoff was intercepted during 6-hour periods, and the energy balance over the lysimeter computed for the same periods. The results of Fohn's work show that the energy balance technique, rigorously applied, can be an excellent predictor of short-term snowmelt at a point.

It is the author's belief that the best of the choice of methods is to adopt as rigorous a physical approach as possible, not withstanding the attendant difficulties. This gives better insight into processes of energy exchange and the interaction of the various controlling factors. Then, in order to make the predictions of snowmelt required by agencies (electric utility agencies, engineers and other water resource managers), other, simpler quasi-physical or statistical techniques may be used. One of the main purposes of the present study is to apply the purely physical energy balance approach to snowmelt estimation, and to examine some of the problems encountered in using such an approach.

Previous Work on Snowmelt Runoff

Remarks similar to those above may be made in relation to the
synthesis of snowmelt hydrographs; there has been very little physi-
cally based work. Viessman (1968) applied unit hydrograph techniques
to the problem of prediction of basin snowmelt hydrographs. This
type of synthesis may yield results which can be used for flood design
work, but are unlikely to elucidate the processes involved in the
generation of snowmelt hydrographs at the scale of a hillside. In
addition, the unit hydrograph technique assumes linearity of the
system, or that response is a linear function of input. This is not so,
as is demonstrated in the treatment of the theory of snowmelt runoff
in Chapter 4. Satisfactory application of the unit hydrograph technique
also requires that duration of the input should be less than one-third
of the total travel time in the system being considered. This is ob-
viously not satisfied in the case of snowmelt on small plots.

There is, to the author's knowledge, only one series of papers
describing a physical model of snowmelt runoff resulting from daily
snowmelt waves. These are the works of Colbeck (1971,1972,1974), and
are physically complete, but also simple enough for use with accessible
data. Colbeck's treatment (to be described later in detail) is a model
of porous medium flow through the unsaturated path from snow surface
to ground, and then through the saturated path downslope to the channel.
The unsaturated flow portion of the model has been tested, (Colbeck and
Davidson (1972), with some uncertainties due to the presence of ice
lenses in the deep snow packs of the Cascade Mountains, Washington. The
combined model incorporating the saturated flow path has not been tested.

It is generally acknowledged that the physical modelling of the generation of snowmelt hydrographs is a very desirable development in snowmelt hydrology (National Research Council, 1971; Canada National Committee - International Hydrological Decade, 1968). The present study, through the application of the energy balance to the snowmelt problem, and the application of the Colbeck model to the problem of hydrograph generation, is an attempt to move in the direction of the physical modelling of snowmelt hydrographs.

CHAPTER 3

THE THEORY OF SNOWMELT

Heat Sources for Snowmelt

Although there are many sources and sinks for energy within the snow-vegetation-air system, some of them may be ignored. Such things as heat storage in vegetation, or the kinetic energy of rain could be computed, but they are so small that they are much less than the errors involved in the computation of the five major sources. The first term to be considered in the heat balance of the snowpack is the heat deficit.

a. Heat deficit (H_θ)

The change in heat storage in the snowpack is included in the energy balance because the temperature of the snowpack varies up to a maximum of $0^\circ C$. In particular, a heat deficit occurs from radiative, evaporative, and sensible heat losses during most nights and on some days during the melt season. When computing the hourly or daily heat balance of the snowpack, these negative heat flows are accumulated. At the onset of the next day's melt, this heat deficit has to be satisfied be fore any heat is available for melting of the snowpack. H_θ is not considered before the first melt, that is, during the "ripening" of the snowpack. This process has been discussed by others (see Bader et al., 1954). Ripening involves the gaining of heat by the snowpack, and the increase of snow crystal size as water resulting from surface melt flows over the crystals. The most important effect of ripening on water flow is the increase in crystal size and its effect on the overall permeability of the snow.

The thermal ripening of the snowpack involves the raising of its temperature until it becomes isothermal at $0^\circ C$. Only then can water flow from the bottom of the pack. The process of heat gain is a combination of the conduc-

tion of heat from the surface down into the snowpack, and the transport of heat into the snowpack by meltwater. This process is rapid once liquid water starts to percolate into the snowpack because of the large amounts of latent heat released by the percolating meltwater as it re-freezes in the pack.

A rough estimate of the maximum total heat deficit of a 2 m snowpack may be made by assuming a value of 0.3 gm/cm³ for the density of the snow, and 0.5 cal/gm/°C for the specific heat of snow. If we assume a snowpack base temperature of approximately -5°C, and a surface temperature of -25°C, the heat deficit under these conditions is 450 cal/cm²; the equivalent of 5.6 cm of melt. This is an estimate of the winter maximum heat deficit. Maximum heat deficits on the tundra reached values of over 4 cm of melt during cold periods on the tundra in the 1972 melt season. The maximum overnight heat deficit in the woods was 0.13 cm (10.4 cal/cm²).

Once the heat deficit has been reduced to zero, the overall heat balance of the snowpack may be written:

$$H_m = H_R + H_c + H_e + H_p + H_g \qquad (3.1)$$

where H_m is the heat available for melting snow   (cal/cm²/hr)

H_R is the radiation heat flow   (cal/cm²/hr)

H_c is the sensible heat flow   (cal/cm²/hr)

H_e is the latent heat flow   (cal/cm²/hr)

H_p is precipitation heat flow   (cal/cm²/hr)

H_g is heat flow from the ground   (cal/cm²/hr)

b. Ground heat flow (H_g)

Heat flow from the ground surface into the snowpack is given by

$$H_g = \frac{d\theta}{dz} \cdot K_g \qquad (3.2)$$

where $\frac{d\theta}{dz}$ = temperature gradient in the ground (°C/cm)

K_g = ground thermal conductivity (cal/cm/hr/$^{\circ}$C)

The ground heat flow is generally small, except near large underground heat sources, such as springs. In most cases it is assigned a small positive constant value through the melt. In the Schefferville area during the time of the study, frozen ground persisted under the thin snowpack at the end of the thaw, and so although the ground heat flow may not be zero, it is insufficiently large to cause any melting at the base of the snowpack. Thus for the purposes of this study, the ground heat flow is assumed to be zero.

c. Precipitation heat flow (H_p)

Rain contains heat which can melt snow by virtue of the elevation of its temperature above 0°C, thus

$$H_p = \rho_w \cdot C_w \, (T_w - T_s) P_r \tag{3.3}$$

where ρ_w = density of water (gm/cm^3)

C_w = specific heat of water (cal/gm/$^{\circ}$C)

T_w = wet-bulb temperature ($^{\circ}$C)

T_s = snow surface temperature ($^{\circ}$C)

P_r = rainfall intensity (cm/hr)

The wet-bulb temperature is equivalent to the temperature of the rain. The precipitation heat flow is small except in the case of heavy precipitation, and in this case, the amount of actual precipitation water is much larger than the melt water produced by the input of heat. In the two years of fieldwork, rainfall was negligible and so this heat flow was not computed.

d. Radiation heat flow (H_R)

The radiation heat flow is expressed as the balance of incoming and outgoing radiation.

$$H_R = (D + q) (1 - a) \pm L_n \tag{3.4}$$

This page deliberately left blank in order to preserve pagination.

where

$(Q + q)$ = incoming shortwave radiation. Q represents the direct solar beam, and q the diffuse component of solar radiation $(cal/cm^2/hr)$

a = albedo (dimensionless)

L_n = net longwave radiation $(cal/cm^2/hr)$

Measurements of net allwave radiation can be made with a net allwave radiometer with polyethylene domes. It is however, unusual to have a continuous record of such measurements, partly because of the expense of the instruments, and partly because they require sophisticated electrical recorders, unsuited to moderately severe field conditions.

Global, or total incoming shortwave radiation is best measured with an Eppley pyrheliometer, but, again because of the expense of these instruments, they are not used routinely. Measurements of global radiation are usually made with a Belfort type pyrheliograph with a clockwork-driven recording mechanism. This instrument is both reliable and easy to use. In the present study all three types of instrument were used.

Albedo may may be measured using two solarimeters, one facing up measuring incoming shortwave radiation, and one facing down measuring reflected shortwave radiation.

Computations of net radiation (as opposed to measurement) made in the past rely on the fact that sky longwave emission may be computed as a function of atmosphere vapour pressure and temperature. Examples of this type of analysis using the Brunt equation are given by USACE (1956), and U.S.

Geological Survey(1954). There are many problems with this technique. They relate primarily to the difficulty of using near-surface observations of temperature and vapour pressure to characterize the vertical distribution of airmass properties. This is only an approximation, and may be inappropriate for some airmasses. Clouds also cause large errors in the estimation of net allwave radiation, because they affect sky emission. The technique of computing H_R from its components was attempted during the present study, using various empirical relationships between sky emission, vapour pressure, and temperature (Sellers, 1965). These techniques seem to work well over periods of 24 to 48 hours, as demonstrated in the Lake Hefner study (U.S. Geological-Survey, 1954), but for hourly values the results were almost completely unsatisfactory. On some hours the estimates were within 15 percent of measured values. On the other hours, the estimates of net allwave radiation ranged from 10 to 400 percent of measured values. Consideration of the size of the terms in Equation 3.4 shows why this is so. Generally the absorbed shortwave term $(Q + q)(1 - a)$ is in the order of $0 \rightarrow 25$ cal/cm^2/hr. A melting snow surface emits longwave radiation at a rate of 26.7 cal/cm^2/hr, and sky emission calculated by the Brunt equation varies from 20 to 30 cal/cm^2/hr . Since the value of the outgoing radiation from the snow is fixed, this means:

where

$$H_R = (Swa) \pm (L\downarrow - S\uparrow)$$

Swa $=$ absorbed shortwave radiation (cal/cm^2/hr)

L$\downarrow$ $=$ sky longwave emission (cal/cm^2/hr)

S$\uparrow$ $=$ snow longwave emission (cal/cm^2/hr)

the absorbed shortwave term may be well defined, but the numerical
size of the term ($L\downarrow$ - $S\uparrow$) means that if Swa is small, then gross
overestimates or underestimates of H_R can result from the small difference
between the two relatively large values $L\downarrow$ and $S\uparrow$.

It is therefore not surprising that estimates of H_R derived using
Brunt-type calculations of sky emission are so poor. Because of the
inaccuracy of the Brunt method, net radiation was estimated by a
technique described in Chapter 7.

(e,f) Turbulent Heat Fluxes (H_c and H_e)

The two remaining heat fluxes are the turbulent transfer heatflows:
those energy inputs of sensible and latent heat driven by gradients of
temperature and water vapour, and by turbulence in the lower atmosphere.
The following derivation follows Sellers (1965). The transfer of heat,
water vapour, and momentum is caused by the action of eddies in the stream
of air passing over a surface. In turbulent flow, parcels of air do not
pass constantly parallel to the surface. Occasionally, parcels of air of
higher velocity and differing moisture or temperature penetrate down to-
wards the surface, resulting in the transfer of moisture or heat to or
from the surface. The total amount of heat or moisture which is transported
to or from the surface depends on how effective these eddies are in pene-
trating the air towards the surface.

Although the air in the lower 2m of the atmosphere is nearly always
turbulent, there is a thin layer immediately above the ground (or snow)
surface into which turbulence cannot penetrate. This layer, probably less

than 2mm thick, is called the laminar boundary layer. Within this
layer, transport of heat, momentum, and moisture are by the pro-
cesses of molecular diffusion, the rate at which these transfers take
place being proportional to the vertical gradients of temperature,
velocity, and moisture. The expression for the flux of sensible heat
through the laminar boundary layer is

$$H_c = - \rho_a \cdot C_p \cdot k_h \left(\frac{\Delta T}{\Delta z} \right) \qquad \qquad 3.5$$

where

ρ_a = air density (gm/cm^3)

C_p = specific heat of air at constant pressure ($cal/gm/^oC$)

$\frac{\Delta T}{\Delta z}$ = gradient of temperature with height within the boundary layer($^oC/cm$)

k_h = molecular diffusivity of heat in air (cm^2/hr)

For latent heat, the transport through the laminar boundary layer is

$$H_e = - \rho_a \cdot L \cdot d \left(\frac{\Delta q}{\Delta z} \right) \qquad \qquad 3.6$$

where

L = latent heat of vapourisation of water (cal/gm)

d = molecular diffusivity of water vapour in air (cm^2/hr)

$\left(\frac{\Delta q}{\Delta z} \right)$ = gradient of moisture with height within the boundary layer
(gm/gm/çm)

The corresponding expression for momentum is

$$\tau = \rho_a \cdot v \cdot \left(\frac{\Delta u}{\Delta z} \right) \qquad \qquad 3.7$$

where

τ = shear stress (dynes/cm^2)

ν = kinematic viscosity of air (cm^2/hr)

$\dfrac{\Delta u}{\Delta z}$ = gradient of velocity with height within the boundary layer (cm/hr/cm, or hr^{-1})

The flows of latent and sensible heat are conventionally regarded as negative if they are directed downwards. This convention is adopted for this development of the theory of snowmelt.

It would not be possible to measure the appropriate gradients and properties within the boundary layer, and so these equations are not useful in assessing the exchanges between the surface and the air. We may, however, by analogy with the above equations, write out the following identities for the turbulent regime, where the molecular diffusivities k_h, d and ν are replaced by their equivalents in the turbulent layers; that is the eddy diffusivities for heat, moisture, and momentum; K_h, K_w and K_m. Thus

$$H_c = - \rho_a \cdot C_p \cdot K_h \cdot \frac{\Delta T}{\Delta z} \qquad 3.8$$

where

K_h = eddy diffusivity for heat in air (cm^2/hr)

$$H_e = - \rho_a \cdot L \cdot K_w \cdot \frac{\Delta q}{\Delta z} \qquad 3.9$$

where

K_w = eddy diffusivity of water vapour in air (cm^2/hr)

and

$$\tau = \rho_a \cdot K_m \cdot \frac{\Delta u}{\Delta z} \qquad\qquad 3.10$$

where

K_m = eddy diffusivity for momentum in air (cm^2/hr)

These equations are difficult to use in assessing the exchanges of heat, moisture and momentum because the eddy diffusivity will vary with atmospheric conditions and with height. We need to derive an exchange coefficient which is constant with height, and which can be easily assessed. We can assume that total exchange does not vary with height - that is, if a flow of (e.g.) 10 units of heat directed down to the snow surface passes an imaginary boundary at 0.1 mm above the surface, then that same flow of 10 units must also have passed imaginary boundaries at 10 cm, 1 m, and 2 m above the snowpack. This assumption of constancy of flux with height also implies that no sinks for heat, moisture, or momentum exist in the air layers above the snow. This is not true for conditions of extreme stability, but is an acceptable approximation for most atmospheric conditions. We can fix the surface temperature of a melting snowpack at $0^o C$, and its vapour pressure at 6.11 mb. If we now combine the molecular and eddy equations, and use the snow surface to define $\Delta q, \Delta T$ and Δu , we obtain expressions for the total transfers by molecular diffusion and turbulent exchange

$$H_c = - \rho_a \cdot C_p \ D_h (T_a - T_s) \qquad\qquad 3.11$$

where

D_h = transfer coefficient for heat (cm/hr)

T_s = snow surface temperature (^{o}C)

T_a = air temperature (^{o}C), at a height z above the snow surface.

$$H_e = - \rho_a \cdot L \cdot D_w (q_a - q_s) \qquad 3.12$$

where

D_w = transfer coefficient for water vapour (cm/hr)

q_a = specific moisture of air (gm/gm)

q_s = specific moisture of surface (gm/gm)

and

$$\tau = \rho_a \cdot D_m u_z \qquad 3.13$$

where

τ = shear stress (dynes/cm^2)

D_m = transfer coefficient for momentum (cm/hr)

u_z = windspeed at height z (cm/hr)

For normal magnitudes of atmospheric humidity, q_a can be expressed to a suitable approximation (Rose, 1966) as

$$q_a = \frac{.622 \, e_a}{p} \qquad 3.14$$

where

p = barometric pressure (mb)

e_a = vapour pressure of air (mb)

The latent heatflow may thus be written

$$H_e = - \frac{0.622}{p} \cdot \rho_a \cdot L \cdot D_w (e_a - e_s) \qquad 3.15$$

The exchange coefficient (for example) D_m, then, is the integrated effect of molecular and eddy diffusivities over the total height z, or

$$D_m = \left[\int_o^z \frac{1}{\nu + K_m} \, dz \right]^{-1} \qquad 3.16$$

The value of the exchange coefficients may be derived as follows. We know

$$\tau = \rho_a \cdot D_m \cdot u_z \qquad 3.17$$

or

$$\left(\frac{\tau}{\rho_a}\right) = D_m \cdot u_z \qquad 3.18$$

since

$$\left(\frac{\tau}{\rho_a}\right) = u_*^2$$

where $u_* =$ friction velocity (cm/hr)

$$D_m = \frac{u_*^2}{u_z}$$

Now, since

$$u_z = \frac{u_*}{k} \, \ell n \left(\frac{z}{z_o}\right) \qquad (\text{Rose, 1966}) \qquad 3.20$$

$$D_m = \frac{k^2 u_z}{[\ell n \left(\frac{z}{z_o}\right)]^2} \qquad 3.21$$

We may, finally, assume that the exchange coefficients D_m, D_w and D_h are equal. The rationale for this assumption is that all of the processes of transfer from the atmosphere to the surface rely on the action of eddy penetration to carry energy (heat, vapour or momentum). Since all three properties are being carried at the same time by the same eddy, it is reasonable to assume that the eddy conductivity of the air is the same for all three properties in the eddy Although recent work has shed some doubt on the validity of this assumption, particularly under conditions of extreme stability, it is probably valid for heights of less than 2m under normal stability conditions, so we may now write out the exchange equations as follows :

$$H_c = - \frac{k^2 u_z}{[\ell n (\frac{z}{z_o})]^2} \cdot \rho_a \cdot C_p \cdot (T_a - T_s) \qquad 3.22$$

and

$$H_e = - \frac{0.622}{p} \cdot \frac{k^2 \cdot u_z}{[\ell n (\frac{z}{z_o})]^2} \cdot \rho_a \cdot L \cdot (e_a - e_s) \qquad 3.23$$

or, by re-arranging and combining constants, for any single roughness length z_o and height z,

$$H_e = - C_1 (e_a - e_s) \cdot u_z \qquad 3.24$$

$$H_c = - C_2 (T_a - T_s) \cdot u_z \qquad 3.25$$

One difficulty encountered in applying these equations is assessing the boundary conditions; that is the temperature and vapour pressure of the surface. Over normal surfaces (grass, earth, water)

these are variable quantities liable to change in response to the temperature and moisture of the atmosphere. In the case of melting snow, however, the surface cannot respond to changes either in air temperature or vapour pressure. The temperature of a melting snow surface is 0°C., and its vapour pressure is the saturated vapour pressure of water at 0°C.: that is 6.11 mb. Using these boundary conditions, the exchange equations may be used directly, knowing u_z, the wind-speed at a fixed height and e_a the air vapour pressure and T_a the air temperature at that height.

At night, if the snow surface stops melting, the above remarks are no longer true. The solution to this problem is discussed later.

Effects of Stability on Heatflows.

In all the preceding derivations, a neutral atmosphere has been assumed, i.e. conditions were neither stable nor unstable. Stable conditions occur when the surface is cooler than the airstream In this situation, the air most intimately in contact with the surface is cooled. This air then assumes a higher density, and so tends to remain in its lower position. If displaced upwards, by virtue of its higher density it will tend to return to its original position. In conditions like this, turbulence tends to be damped, and the exchanges of heat and water vapour between the atmosphere and the surface are reduced. In unstable conditions, the surface temperature is higher than the airstream temperature. Air in contact with the surface will be warmed, will assume a lower density and thus tend to rise. At zero windspeed, in the absence of mechanically caused turbulence, some

exchange will still take place by the process of free convection. These unstable conditions, therefore, tend to increase fluxes, and will augment the exchanges of heat and water vapour.

The term used to describe degrees of stability and instability of the lower atmosphere is the dimensionless bulk Richardson number Ri, (Szeicz et al., 1969)

$$Ri = \frac{g \cdot \Delta z \cdot \Delta T}{Tabs \, (\Delta u)^2} \qquad\qquad 3.25$$

where

g = acceleration due to gravity (cm/hr^2)

$Tabs$ = air temperature $(^\circ K)$

ΔT = Temperature difference $(^\circ K)$ over height difference Δz

Δu = windspeed difference (cm/hr) over a height difference of Δz.

For stable conditons, the surface is colder than the air, and ΔT is positive, giving a positive Ri. Under neutral conditions, ΔT is zero, and Ri is zero. Under unstable conditions, ΔT is negative, since the surface is at a higher temperature than the air, and thus Ri is negative. The effects of differing stability is shown qualitatively in Figure 3.1. As Ri increases, the observed flux becomes increasingly less than the neutral flux. Taking the example of sensible heat, an equation of the general form

$$(H_c)_{stable} = (H_c)_{neut} \left[\frac{1}{(1 + \sigma \cdot Ri)}\right] \qquad\qquad 3.26$$

where

FIGURE 31

General Effects of Positive Stability on Heatflow.
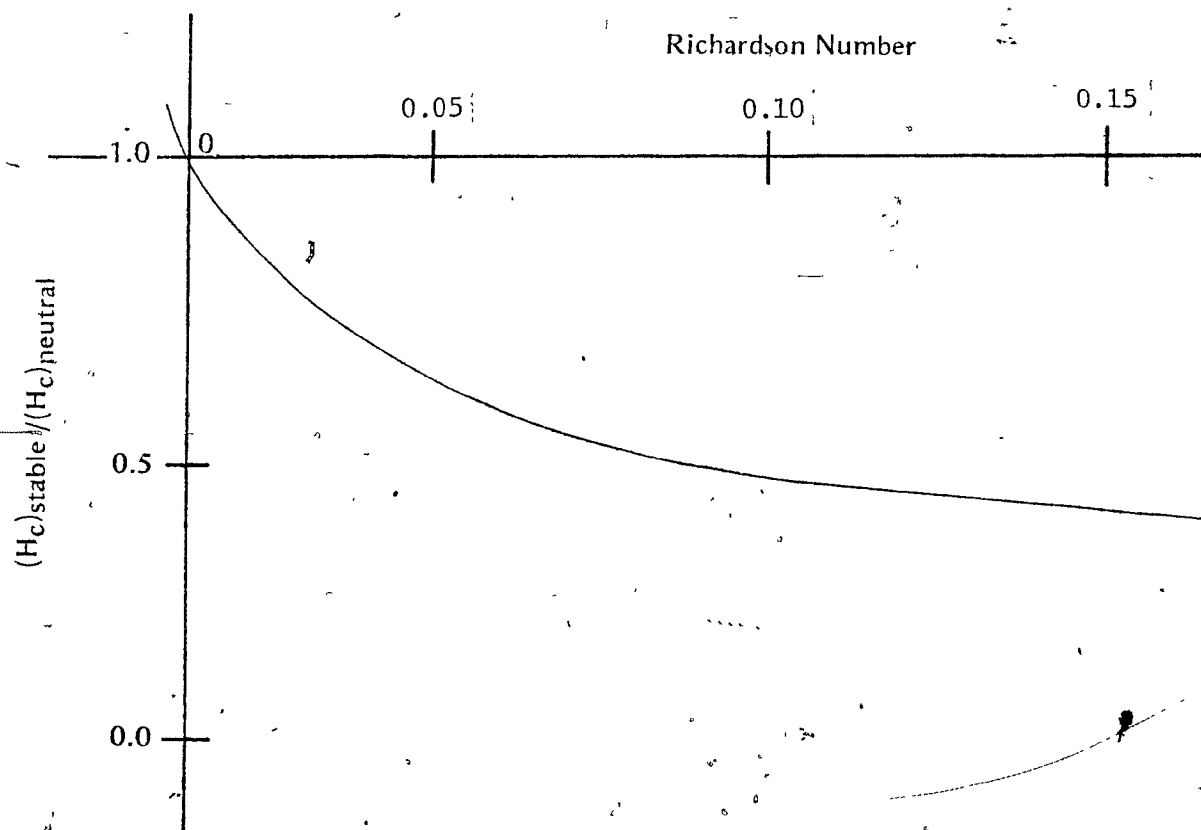
Based on generalised results

$(H_c)_{stable}$ = observed sensible heatflow under stable conditions

$(H_c)_{neut}$ = sensible heatflow under neutral conditions

Ri = Bulk Richardson number

σ = empirical constant

would describe the decrease in exchange with increasing stability. A similar equation for the unstable case might be written

$$\frac{(H_c)_{unstable}}{(H_c)_{neutral}} = (1 - \sigma \, Ri)$$

where

$(H_c)_{unstable}$ = sensible heatflow under unstable conditions

As Ri is negative in these unstable conditions, $(H_c)_{unstable}$ will be greater than $(H_c)_{neutral}$.

In most applications, it is difficult to measure the temperature of a surface, and so Ri is generally measured over an interval $\triangle z$ within the atmosphere. In the case of melting snow however, the surface forms an excellent constant boundary condition with e_s and T_s both known, since melting snow has a temperature of 0^oC and a vapour pressure of 6.11 mb. In this case, the value of Ri for the whole atmosphere under 2m is easily computed.

The Richardson number is only one index allowing an assessment of stability conditions in the atmosphere. An alternative is the Monin-Obuchov stability length W, where from Webb (1965)

$$W = - \left[\frac{u_*^3}{\left[\frac{k \cdot g}{\rho_a \cdot C_p \cdot Tabs} \right] H_c} \right] \qquad 3.27$$

We can show that this formulation and its use are equivalent to the bulk Richardson number.

From Equation 3.11, H_c is given by

$$H_c = - \rho_a \cdot C_p \, D_h \, \Delta T$$

and using Equation 3.22, substituting for D_h

$$H_c = - \frac{\rho_a \, C_p \, k^2 u_z \, \Delta T}{[\ell n(z/z_o)]^2}$$

The form of the wind profile under neutral conditions (from Equation 3 20) is:

$$u_z = \frac{u_*}{k} \, [\ell n(z/z_o)]$$

For stable conditions Webb (1965) gives, after Monin and Obuchov

$$u_z = \frac{u_*}{k} \, [\ell n(z/z_o) + \alpha \frac{(z-z_o)}{W}] \qquad 3.28$$

where α is an empirical constant.

From Equation 3.27, if $\Delta T = 0$, that is if conditions are neutral, W becomes indefinitely large, since $H_c = 0$ Equation 3.28 then collapses

to the neutral case, as the term $\dfrac{\alpha(z - z_o)}{W}$ becomes zero. In the case of stable conditions, with T_a greater than T_s, H_c is negative (i.e. directed downwards), and thus W becomes positive. The term $\dfrac{\alpha(z - z_o)}{W}$ thus becomes positive. As is shown in the following derivation, this reduces the effective exchanges between the air and the surface. with this modification for stability, Equation 3.21 becomes

$$\frac{u_*^2}{u_z}\bigg|_{stable} = (D_h)_{stable} = \frac{k^2 \cdot u_z}{\left[\ln\left(\dfrac{z}{z_o}\right) + \alpha \dfrac{(z-z_o)}{W}\right]^2} \qquad 3.29$$

and so

$$\frac{(D_h)_{neutral}}{(D_h)_{stable}} = \frac{\left[\ln'\left(\dfrac{z}{z_o}\right) + \alpha \dfrac{(z-z_o)}{W}\right]^2}{\ln\left(\dfrac{z}{z_o}\right)^2}$$

expanding the numerator, we obtain

$$\frac{(D_h)_{neutral}}{(D_h)_{stable}} = \frac{\left[\ln\left(\dfrac{z}{z_o}\right)\right]^2 + \dfrac{2\alpha(z-z_o)\ln\left(\dfrac{z}{z_o}\right)}{W} + \left[\dfrac{\alpha(z-z_o)}{W}\right]^2}{\ln\left(\dfrac{z}{z_o}\right)^2} \qquad 3.31$$

$$= 1 + \frac{2\alpha\,(z-z_o)}{W\ln\left(\dfrac{z}{z_o}\right)} + \left[\frac{\alpha(z-z_o)}{W\ln\left(\dfrac{z}{z_o}\right)}\right]^2 \qquad 3.32$$

The squared term is so small that it can be ignored. Webb (1970) gives a value of $\alpha = 5.0$ from good experimental data, so Equation 3.32 becomes

$$\frac{(D_h)_{neutral}}{(D_h)_{stable}} = 1 + \frac{10(z - z_o)}{W \ln(\frac{z}{z_o})} \qquad 3.33$$

Taking the example of heat, since

$$H_c = - \rho_a \cdot C_p \, D_h \, (T_a - T_s)$$

$$\frac{(H_c)_{neutral}}{(H_c)_{stable}} = 1 + \frac{10(z - z_o)}{W \ln(\frac{z}{z_o})} \qquad 3.34$$

or

$$(H_c)_{stable} = (H_c)_{neutral} \; 1 \Big/ 1 + \frac{10(z - z_o)}{W \ln(\frac{z}{z_o})} \qquad 3\ 35$$

Equation 3.35 has the same general form as Equation 3.26, if

$$Ri = \frac{(z - z_o)}{W \ln(\frac{z}{z_o})} \qquad 3.36$$

we know from Equation 3.27 that

$$W = - \frac{u_*^3 \, \rho_a \cdot C_p \cdot Tabs}{H_c \cdot k \cdot g}$$

and since for the stable case, with H_c directed downwards $(T_a > T_s)$,

$$H_c = - \rho_a \cdot C_p \cdot D_h \cdot \Delta T$$

then

$$W = \frac{u_*^3 \cdot Tabs}{D_h \cdot \Delta T \cdot k \cdot g}$$

3.37

From Equation 3.20

$$u_*^3 = \frac{k^3 u_z^3}{[\ln(\frac{z}{z_o})]^3}$$

or

$$W = \frac{k^3 \cdot u_z^3 \cdot Tabs}{D_h \Delta T \cdot k \cdot g \cdot [\ln(\frac{z}{z_o})]^3}$$

3.38

Substituting for W in Equation 3.36, we obtain

$$Ri = \frac{(z-z_o) \cdot D_h \cdot \Delta T \cdot g \cdot [\ln(\frac{z}{z_o})]^2}{k^3 u_z^3 \ Tabs}$$

Substituting for D_h, from Equation 3.21, gives

$$Ri = \frac{(z - z_o) \cdot \Delta T \ g}{u_z^2 \ Tabs}$$

3.39

This is the bulk Richardson number for the whole layer of atmosphere between the surface and height z, and may be written

$$R_i = \frac{\Delta z \cdot \Delta T \cdot g}{(\Delta u)^2 \cdot Tabs}$$

Therefore, Equation 3.36 is satisfied, and substituting Ri from Equation 3.36 into Equation 3.35 gives

$$(H_c)_{stable} = (H_c)_{neutral} \cdot [\ 1/(1 + 10\,Ri\ )]$$

which is identical to equation 3.26 if $\sigma = 10$.

Although Webb (1970) derived his results over surfaces other than snow, the results hold regardless of this. It only matters that Ri should be correctly defined. If we know the temperature, vapour pressure, and windspeed at any height above a melting snowpack it is possible to write out correct turbulent heatflow terms regardless of the conditions of stability.

In the field study when the snow surface was melting, and under high temperature and low windspeed conditions, Ri rose to values of up to +0.10, causing a calculated reduction of flux of about 50 percent from the neutral case. In the application of the heatflow model in this study, snow surface temperatures are fixed at $0^{o}C$ for periods when melting was known to be occurring, and for periods when melting was known to have ceased, T_s was fixed at the wet-bulb temperature. Since over a melting surface T_a is usually greater than T_s, and because of the use of T_w as surface temperature at night when melting had ceased, $(T_a - T_s)$ is generally positive. Thus the Ri positive or stable case is normal over the snowpack. Occasional Ri negative conditions do occur, but the correction for these unstable conditions is not attempted. The case of negative Ri values usually occurs when the snow surface temperature is

least well known - usually at night since the snow surface temperature is neither fixed, nor measured, but only approximated by the wet-bulb temperature (T_w). Because of this uncertainty, the value for Ri is not precisely known, and the correction for negative Ri (unstable conditions),

$$(H_c)_{unstable} = (H_c)_{neutral} (1 - 10 \cdot Ri)$$

is prone to large variations. For this reason, the corrections for stability are not computed. For negative ΔT values (i.e. T_s greater than T_a, or H_c directed upwards), the value of Ri is assumed to be zero; that is, neutral conditions. This approximation is in accordance with the observations of de La Casinière (1974) who notes that negative Ri values occur only rarely over snow.

It should be noted at this point that in the preceding derivations, the normal convention of heatflows being negative if directed down to the surface was followed. In the remainder of the text, the heatflows will all be regarded as positive if they are directed down into the pack (heat gain by the pack), and negative if they are out of the pack (heat loss from the pack).

The effects of stable stratification are mentioned by Wilson (1941), but he rejects them as insignificant, as does Light (1941). Anderson (1968) in a work with similar objectives to the present study, fails to mention the problem. The U.S.A.C.E. (1956) work does not discuss the problem, nor does Fohn (1974). De La Casinière (1974) gives a thorough analysis of stability effects over snow, but fails to present any substantial testing of his computed heatflows against observed snowmelt.

The importance of the turbulent heatflow terms is very great under some conditions, and since the corrections for stability may be easily applied and require no data additional to that usually available, the application of the theory described above is both easy and valuable.

The only variable which has to be estimated in the heatflow equations is the roughness length z_o . According to Lettau (1969), the roughness length may be estimated from the following description of roughness elements (see Figure 3.2)

$$z_o = \frac{h^* S}{2S'}$$
3.40

where

z_o = roughness length (cm)

h^* = effective height (cm) of obstacles

S = silhouette area (cm^2)

S' = basal area (cm^2)

Lettau (1969) notes that estimates made using Equation 3.40 agree closely with measured values of z_o. In using this approach, it is assumed that the form roughness of the snow is dominant over skin roughness. For the wind velocities of $\simeq$ 9 km/hr (2.5 m/s) encountered in this study, the assumption is probably good. Reference to Equation 3.21 will show that as z_o increases, so does the exchange coefficient D_m, and thus the total exchange. For the field study, an approximate ratio of basal to silhouette area was arrived at from the following figures. A typical

FIGURE 3.2

Wind Direction

A

Basal Area (S')

A'
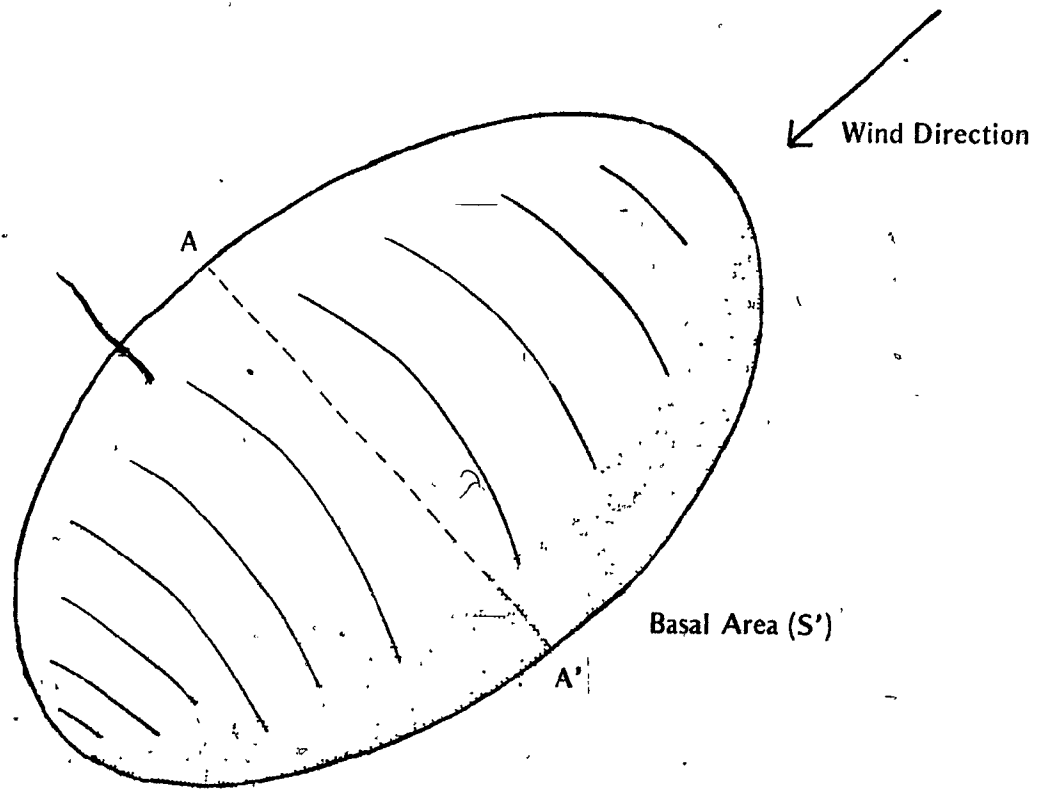
Diagrammatic Representation of a Snowbank, with dimensions used in estimating z_0 (Roughness length)

A

A'

H^*
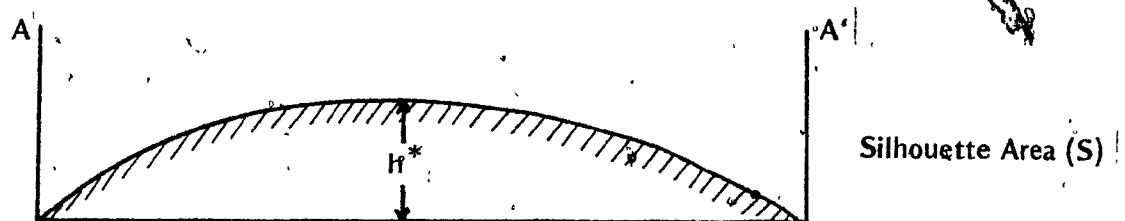
Silhouette Area (S)

snowdrift within the woods has a basal area of approximately 100 m^2, and a silhouette area of approximately 1 m^2. The effective obstacle height can be approximated by the difference in height between "crest" and "trough" on the snow surface. The value for this may be derived from the maximum difference between snowstake depths, and this is always approximately 1m, so from Equation 3.40

$$z_o = \frac{100 \times 1 \times 10^4}{2 \times 100 \times 10^4} \quad cm$$

$$= 0.5 \; cm$$

This roughness length estimate can only be regarded as approximate, since conditions vary from site to site, and the basal and silhouette areas were arrived at by sketching drifts and estimating their area. Although the z_o estimate is important, the calculated melt is relatively insensitive to it. The exchanges computed using $z_o = 1.0$ cm (for example) are 1.28 times greater than the exchanges computed using $z_o = 0.5$ cm. It is felt that $z_o = 0.5$ cm is a good estimate, and it is in the same order as figures conventionally used for snow surfaces, which vary from 0.1 cm to 0.5 cm. In any case, variations in the 2 m. windspeed between sites is likely to cause much greater differences in the heatflows than differences or changes in the z_o estimate.

The preceding calculations make it possible to define the overall heat balance of the snowpack. The definition of night-time heat flows is only approximate because the snow surface temperature is not known,

and has to be equated to the wet-bulb temperature. This poor definition does not allow the computation of the Richardson number during the night and thus night-time turbulent heat-flows are only approximate. The heatflows during the day, when melt is occurring, are satisfactorily defined, so that the total positive heatflow for each day, and thus the daily melt, is well defined.

CHAPTER 4

THEORY OF SNOWMELT RUNOFF

In Chapter 3 a method was outlined for predicting melt at the surface of the snowpack. The present chapter is directed towards routing the predicted surface melt from the snow surface to the base of the slope.

The problem falls naturally into two sections: vertical percolation via the unsaturated path from the snow surface to the ground(path A → B in Figure 4.1), and subsequent flow in a thin saturated layer at the base of the snowpack to the slope base (path B → C) A model describing the unsaturated flow was developed by Colbeck (1971) and tested in the field by Colbeck and Davidson (1972). The model was finally linked with flow along an impermeable boundary (Colbeck,1974). This model has not yet been tested against field measurements. A derivation of the equations governing the distortion of waves of melt-water flux as they travel through the snowpack and down the slope is given below.

The Unsaturated Zone

First let us consider flow through a small volume of the snow-pack in the unsaturated layer. The continuity equation describing flow through this volume is,

$$\text{Input rate - Output rate} = \frac{\text{change in storage}}{\text{time interval}}$$

or, from Figure 4.2

FIGURE 4.1

Path of Water through the Snowpack.
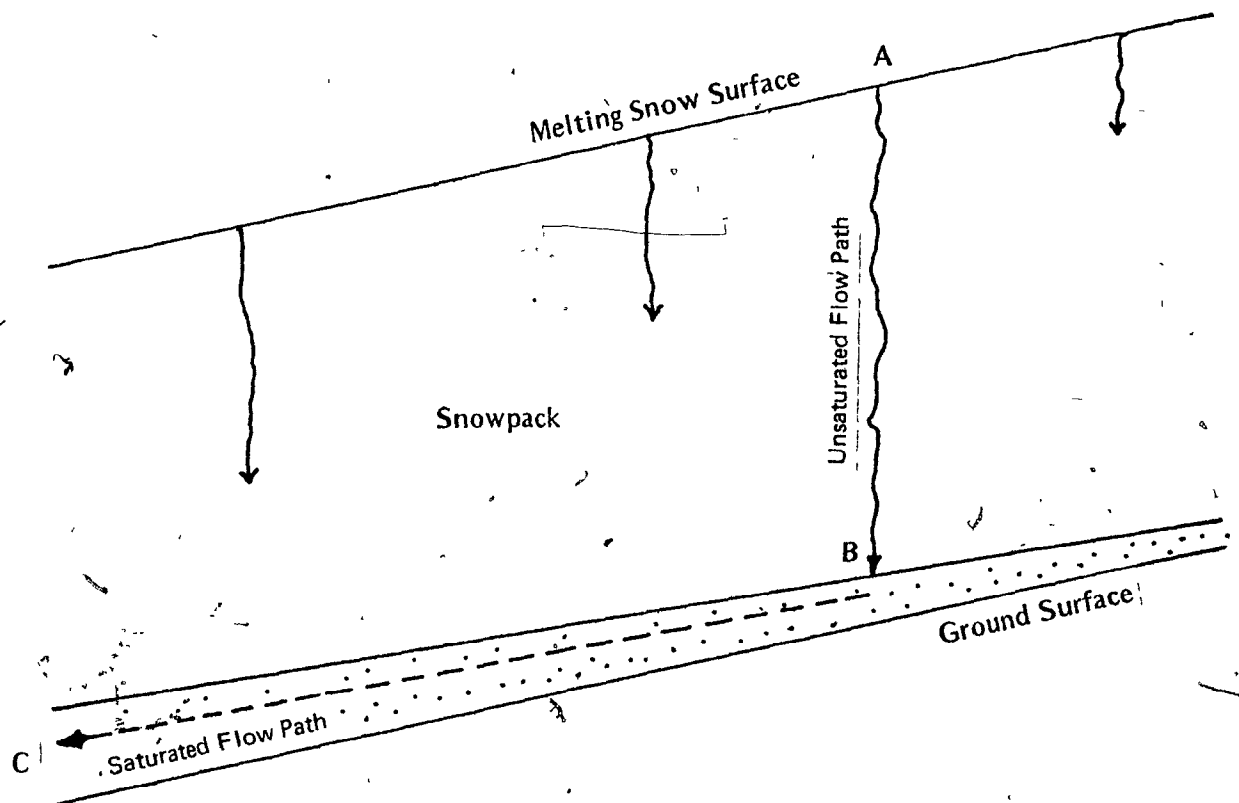
$$Av_1 - Av_2 = \frac{\Delta S^* \cdot \emptyset_e \cdot \Delta z \cdot A}{\Delta t} \qquad 4.1$$

where

$S^* = $ effective saturation $= \left[\dfrac{Sw - Swi}{1 - Swi}\right]$

$S_w = $ actual saturation

$Swi = $ irreducible saturation

$\emptyset_e = $ effective porosity $= \emptyset(1 - Swi)$

$\emptyset = $ total porosity

$A = $ cross-sectional area of the small volume (cm^2)

$v_1, v_2 = $ flux rate of water per unit area $(cm^3/cm^2/hr)$

or

$$\frac{A(v_1 - v_2)}{A\Delta z} = -\emptyset_e \cdot \frac{\Delta S^*}{\Delta t} \qquad 4.2$$

Taking limits as Δz and Δt tend to zero,

$$\frac{\partial v_w}{\partial z} = -\emptyset_e \frac{\partial S^*}{\partial t} \qquad 4.3$$

where

$v_w = $ the flux rate of water per unit area $(cm^3/cm^2/hr)$.

For snowpacks of small depth, the effective porosity may be assumed to be constant with depth. For very deep packs such as the firn zone of a glacier, Colbeck (1971) found it necessary to express $\emptyset_e$ as a function of depth.

The continuity equation for the unsaturated layer may be written

FIGURE 4.2

Input = A.v$_1$

Continuity Diagram for the Unsaturated Layer

Δz

Output = A.v$_2$
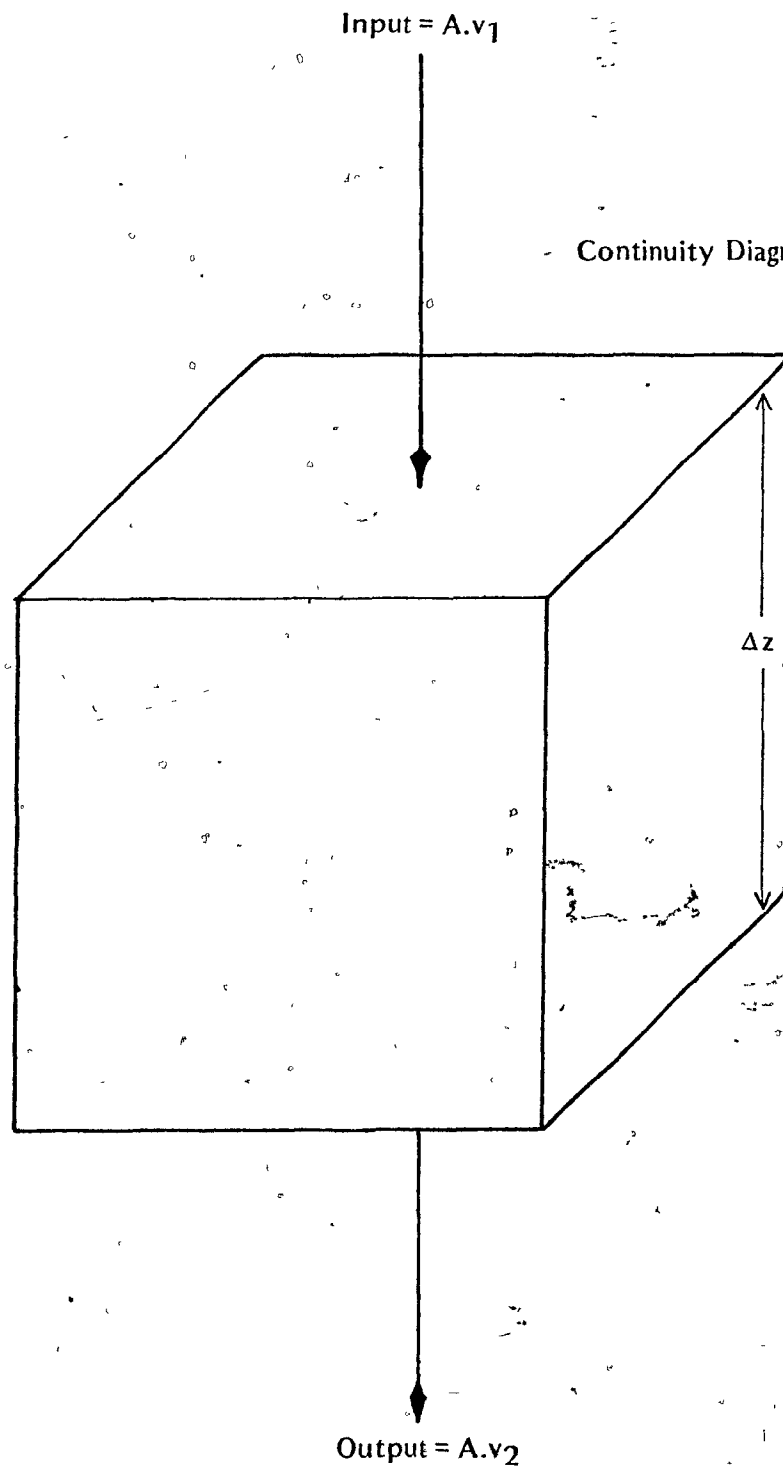
z = thickness of unit considered, positive downwards.

$$\frac{\partial v_w}{\partial z} + \emptyset_e \frac{\partial S^*}{\partial t} = 0 \qquad\qquad 4.4$$

To evaluate the first term, we must first define v_w. Darcy's Law may be written (Scheidegger, 1957)

$$v_w = -\frac{k_w}{\mu}\left(\frac{\partial P_w}{\partial z} - \rho_w \cdot g\right) \qquad\qquad 4.5$$

where

k_w = permeability of snow to water at some fixed value of S^* (cm^2)

$\dfrac{\partial P_w}{\partial z}$ = capillary gradient $(gm/cm^2/hr^2)$

ρ_w = density of water (gm/cm^3)

μ = viscosity of water $(gm/cm/hr)$

The capillary gradient $\dfrac{\partial P_w}{\partial z}$ is small relative to the term $\rho_w \cdot g$, and thus the equation may be written

$$v_w = \frac{k_w}{\mu} \cdot \rho_w \cdot g \qquad\qquad 4.6$$

For snow and coarse textured soils an empirical relationship between permeability k' (at a saturation of $S^* = 1.0$), S^*, and k_w (the permeability at S^*), may be written

$$k_w = k' S^{*n} \qquad\qquad 4.7$$

The value of k' is a constant characteristic for a snowpack in a given condition, and is chiefly determined by crystal size. It may vary with depth in the snowpack if significant variations of crystal size and snow density occur, but the uniformity of the Schefferville snowpacks suggests that a constant value of k' should be used. Substituting for k_w in equation 4.6, we obtain

$$v_w = \frac{\rho_w \cdot g \, k' \cdot S^{*n}}{\mu} \qquad 4.8$$

where S^* and therefore v_w are functions of both z and t. Since v_w is a function of z (depth) and t(time), we can use the chain rule to define the total differential of v_w as

$$dv_w = \frac{\partial v_w}{\partial z} dz + \frac{\partial v_w}{\partial t} dt \qquad 4.11$$

The term dv_w is the change in flux for some change dz in depth and dt in time. If we consider a constant flux (that is, a constant rate of water input at the surface), $dv_w = 0$. We can therefore write

$$\frac{\partial v_w}{\partial z} dz = - \frac{\partial v_w}{\partial t} dt \qquad 4.12$$

then

$$\left(\frac{dz}{dt} \right)_{v_w} = - \frac{\partial v_w}{\partial t} \bigg/ \frac{\partial v_w}{\partial z} \qquad 4.13$$

where

$\left(\dfrac{dz}{dt} \right)_{v_w}$ = vertical velocity of a parcel of vertically percolating water at constant flux v_w

We must now obtain an expression for $\frac{\partial v_w}{\partial t}$. Since, from Equation 4.8, v_w is a function of S^*, $\frac{\partial v_w}{\partial t}$ is a function of $\frac{\partial S^*}{\partial t}$. From Equation 4.8

$$S^* = \left(\frac{\rho_w \, g \, k'}{\mu} \right)^{-1/n} v_w^{1/n}$$

Therefore

$$\frac{\partial S^*}{\partial t} = \left(\frac{\rho_w \, g \, k'}{\mu} \right)^{-1/n} \frac{1}{n} v_w^{(\frac{1}{n}-1)} \frac{\partial v_w}{\partial t} \qquad 4.14$$

Substituting for $\frac{\partial S^*}{\partial t}$ in the continuity Equation 4.4 gives

$$\frac{\partial v_w}{\partial z} + \frac{\emptyset_e}{n} \left(\frac{\rho_w \, g \, k'}{\mu} \right)^{-1/n} v_w^{(\frac{1}{n}-1)} \frac{\partial v_w}{\partial t} = 0 \qquad 4.15$$

and

$$\frac{\partial v_w}{\partial t} = - \frac{n}{\emptyset_e} \left(\frac{\rho_w \, g \, k'}{\mu} \right)^{1/n} v_w^{(1-\frac{1}{n})} \frac{\partial v_w}{\partial z} \qquad 4.16$$

Substituting this value into Equation 4.13 yields

$$\left(\frac{dz}{dt} \right)_{v_w} = \frac{\frac{n}{\emptyset_e} \left(\frac{\rho_w \cdot k \cdot g'}{\mu} \right)^{1/n} v_w^{(1-\frac{1}{n})} \cdot \frac{\partial v_w}{\partial z}}{\frac{\partial v_w}{\partial z}} \qquad 4.17$$

or,

$$\left(\frac{dz}{dt} \right)_{v_w} = \frac{n}{\emptyset_e} \left(\frac{\rho_w \cdot g \cdot k'}{\mu} \right)^{1/n} v_w^{(\frac{n-1}{n})} \qquad 4.18$$

This equation gives the rate of vertical travel of a flux of constant magnitude v_w This means that if we consider a parcel of water flux, or melting, at the surface whose magnitude is known (for example 0.5 cm/hr), then we can predict using Equation 4.18, its rate of travel vertically into the snowpack. This completes the analysis for the unsaturated layer.

The Saturated Layer

For the saturated layer, the continuity equation is derived as follows: consider a small volume of unit width and length Δx (see Figure 4.3). The continuity equation is

$$\text{Input rate} - \text{Output rate} = \frac{\text{change in storage in the saturated layer}}{\text{change in time}}$$

or

$$(I \cdot 1 \cdot \Delta x + h_1 \cdot v_1 \cdot 1) - h_2 v_2 \cdot 1 = \frac{\emptyset_e \cdot \Delta h \cdot \Delta x \cdot 1}{\Delta t} \qquad 4.19$$

dividing through by Δx, we obtain

$$I - \frac{(h_2 v_2 - h_1 v_1)}{\Delta x} = \emptyset_e \frac{\Delta h}{\Delta t} \qquad 4.20$$

Taking limits as Δx and Δt tend to zero, we obtain

$$I - \frac{\partial(h \cdot v_s)}{\partial x} = \emptyset_e \frac{\partial h}{\partial t} \qquad 4.21$$

where

v_s = volume flux in the saturated layer ($cm^3/cm^2/hr$)

FIGURE 4.3
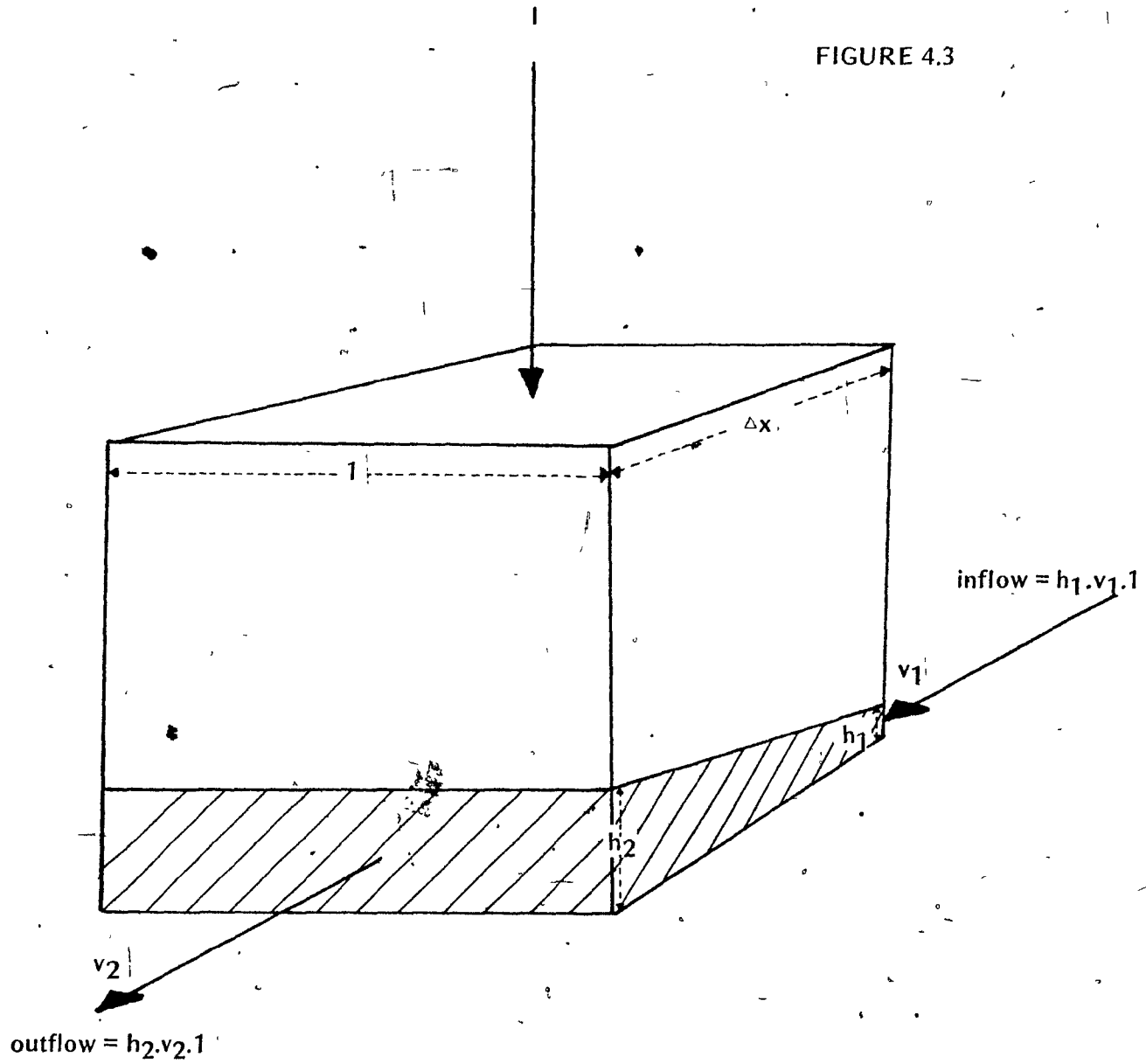
Continuity Diagram for the Saturated Layer.

or

$$\frac{\partial(h v_s)}{\partial x} + \phi_e \frac{\partial h}{\partial t} = I \qquad\qquad 4.22$$

Darcy's Law for the saturated layer may be written (see Bear, et al., 1968), for small values of β (the slope inclination in Figure 4.1),

$$v_s = -\frac{k_s}{\mu}\left(\frac{\partial P_w}{\partial x} - \rho_w \cdot g \cdot \beta\right) \qquad\qquad 4.23$$

where

k_s = permeability of saturated layer (cm^2)

P_w = pressure in the saturated layer (gm/cm^2)

$\beta \simeq \sin\beta$ = slope inclination .

In the thin saturated layer, with flow parallel to the hillslope

$$P_w = \rho_w \cdot g \quad h \qquad\qquad 4.24$$

Substituting this in Equation 4.23 yields

$$v_s = -\frac{k_s}{\mu}\rho_w g\left(\frac{\partial h}{\partial x} - \beta\right) \qquad\qquad 4.25$$

Colbeck (1974) discusses why $\frac{\partial h}{\partial x}$ is negligibly small by comparison with β. This approximation is confirmed by the field measurements of the thickness of the saturated layer. Therefore, Equation 4.25 reduces to

$$v_s = \frac{k_s \rho_w g}{\mu}\beta \qquad\qquad 4.26$$

$$h \cdot v_s = \frac{k_s \rho_w g}{\mu} \beta h \qquad\qquad 4.27$$

and for a hillslope of constant angle

$$\frac{\partial(h v_s)}{\partial x} = \frac{k_s \rho_w g}{\mu} \beta \frac{\partial h}{\partial x} \qquad\qquad 4.28$$

Substituting this equation into the continuity Equation 4.22 gives

$$\frac{k_s \rho_w g \beta}{\mu} \frac{\partial h}{\partial x} + \emptyset_e \frac{\partial h}{\partial t} = I \qquad\qquad 4.29$$

This equation indicates that the thickness of the saturated layer, h varies with time and with distance downslope in response to the input of water percolating from the unsaturated zone. In the case of daily cycles of snowmelt, the input is constant along the slope at any one time, but varies throughout the day in the form of a wave in response to variations in the energy available for melting.

Now let us suppose that an observer moves downslope with the wave, at the same speed as the wave. Let his position in time and distance be fixed by coordinates x' and t' moving at the wave speed C_s, such that

$$x' = x - C_s t \qquad C_s = \text{wave speed} \qquad 4.30$$
and
$$t' = t \qquad t = \text{time} \qquad 4.31$$

Since the observer is moving at the same speed as the wave, he cannot perceive changes in wave height with x' because by the newly defined system, the wave is not moving in the x' frame of

reference. The observer can only perceive changes in wave height with time. In other words

$$\frac{\partial h}{\partial x'} = 0 \ .$$

Thus in Equation 4.22, we can write

$$\frac{\partial h}{\partial t'} = \frac{I}{\phi_e} \qquad\qquad 4.33$$

and so

$$dh = \frac{I}{\phi_e} dt' \qquad\qquad 4.34$$

$$\int dh = \frac{1}{\phi_e} \int_{t_o'}^{t_L'} I\,dt' \qquad\qquad 4.35$$

where t_o' is the time at which the observer leaves the top of the hillslope

t_L' is the time at which the observer reaches the slope base

Equation 4.35 may be written

$$h(x',t_L') - h(x',t_o') = \frac{1}{\phi_e} \int_{t_o'}^{t_L'} I\,dt' \qquad\qquad 4.36$$

or

$$h(x',t') = \frac{1}{\phi_e} \int_{t_o'}^{t_L'} I\,dt' + h(x',t_o') \qquad\qquad 4.37$$

The term $h(x',t_o')$ represents the thickness of the saturated layer at the observer's position at the time he leaves the top of the slope, and is zero. The term $h(x',t')$ represents the thickness of the saturated layer at the observer's position at any time after he has left the hilltop.

We wish to derive an expression for q, the discharge per unit width of hillside, and we know that

$$q = h \cdot v$$

or

$$q(x', t') = h(x't') \cdot v_s(x't') \qquad 4.38$$

The value of $q(x', t')$ is the discharge at the observer's position at any time after he has left the hilltop. Discharge from the base of the slope in the x', t' coordinate system is given as $q(x', t'_L)$ i.e. the discharge when the observer reaches the slope base. We must now derive a value for t'_L. To do this we must find the velocity of flow in the saturated layer. Volume flux (v_s) in the saturated layer is given by

$$v_s = \frac{\rho_w \cdot g \cdot k_s \cdot \beta}{\mu} \qquad 4.39$$

If this volume flux is moving through unit volume, only the effective pore space can be used to accommodate flow, so that the velocity of the water through the medium becomes

$$C_s = \frac{v_s}{\phi_e} = \frac{\rho_w \cdot g \cdot k_s \cdot \beta}{\mu \phi_e} \qquad 4.40$$

the travel time for the slope is given by

$$t'_L = \frac{L_s}{C_s} \qquad 4.41$$

where

L_s = slope length

C_s = flow velocity in the saturated layer.

now, from Equation 4.37 and 4.38, substituting from Equation 4.40

$$q(x', t_L') = \frac{\rho_w \cdot g \cdot K_s \cdot \beta}{\emptyset_e \cdot \mu} \int_{t_o'}^{t_L'} I(0, t') \, dt' \qquad 4.42$$

Equation 4.42 simply states that the discharge from the base of the snowpack $q(x', t_L')$ is equivalent to the input to the saturated layer from the unsaturated layer I integrated over a preceding period equivalent to the time taken for the wave to travel through the saturated layer, that is from time $t' = 0$ to time $t' = t_L'$. Equation 4.42 expresses flow as a volume (cm^3/hr). In order to derive discharge in flux units (cm/hr) we must divide by area. For unit width, slope area is L_s .1, or slope length

From Equation 4.41,

$$L_s = C_s / t_L'$$

and so from Equation 4.40

$$L_s = \frac{\rho_w \cdot g \cdot k_s \cdot \beta}{\mu \, \emptyset_e} \cdot t_L' \qquad 4.43$$

substituting Equation 4.43 in Equation 4.42 we obtain

$$q(x', t_L') = \frac{1}{t_L'} \int_{t_o}^{t_L'} I(0, t') dt' \qquad 4.44$$

Equation 4.44 gives the flux rate in cm/hr at the slope base, i.e. the predicted slope base hydrograph in flux units.

CHAPTER 5

THE FIELD STUDY

Aims of the Study

This study may be directed into two portions. First, the rates

of melting at the surface of the snowpack were predicted from calcula-

tions of the energy balance. Secondly, this surface input of water

was routed vertically through the snowpack as unsaturated flow, and

then over the ground to the base of the hillslope as saturated flow.

The result is the prediction of the snowmelt hydrograph at the base

of the slope. The study, then, entails:

(1) measurement of daily amounts of melting under boreal

forest and on the tundra, on hillslopes of differing aspects and gradient.

(2). Prediction of melt first on a daily, and then on an hourly

basis, from the different hillslopes. These predictions were based on

hourly averages of meteorological observations at the sites.

(3) Prediction of diurnal hydrographs from the base of each slope;

involving the routing of the surface melt through the snowpack and along

the ground.

(4) Continuous measurement of runoff from hillside plots, with

areas of approximately 2000 m^2.

Description of Experimental Sites

The study was conducted on seven hillside plots in two groups.

One group of four plots was in an area of boreal forest and the other

group of three plots was on the tundra (see Figure 1.3 and Figure 1.4).

The study was undertaken on small plots for several reasons. The first of these is that it is easier to attempt water balance computations on a small plot, where deep seepage and soil water recharge can be eliminated or evaluated, than in a drainage basin. In computing the energy balance it is more plausible to use one energy balance measured at a point to predict melt over an area when the distances between the point and the sites are small. On small plots, conditions of soil, gradient,exposure and vegetation cover can be kept fairly uniform. In addition, a higher quality of data is more easily attained when the worker has a small area of operation. This is particularly important in the subarctic, where instrument failures are frequent and constant attention is needed.

On small hillside plots, especially with impermeable soils and shallow (less than 2 m) snowpacks, each day's runoff hydrograph is distinct. This gives an excellent basis for testing daily totalized runoffs against daily totalized energy balance estimates, since delayed flows occuring during early and mid-morning are relatively small.

The seven hillside plots were selected in order to include a range of aspects and gradients, since aspect and gradient affect the incidence of incoming solar radiation. This variation is reflected in the net radiation on the slopes, and this spatial variation of the energy balance is of great interest in snowmelt hydrology (Hendrick and Filgate, 1971). The slopes were treated as planar for the purpose of mapping radiation, although it can be seen from Figures 5.3 and 5.7 that they are

not entirely straight. This also seems to be a valid approximation
for a first attempt at runoff modelling, but will be discussed later.
Table 5.1 shows the general site characteristics.

The Forest Sites

The four forest sites are situated in an area of open lichen
woodland. The forest on the sites has a crown coverage of about 16
percent. The crown density figures given in Table 5.1 were measured
using a photographic method described by Fitzgibbon and Dunne (1970),
which derives the total proportion of the hemisphere occupied by tree
canopy as well as variations in canopy density with angular elevation.
Figure 5.1 is a vertical aerial photograph of the four forest sites,
and together with Figures 1.3 and 1.4, gives a good impression of the
discontinuous nature of the canopy. The two dominant tree species are black
and white spruce. Tree heights in the area of the woods sites vary from
2m to 10 m, with a mean of about 7 m. Underneath the forest canopy, in
more poorly drained locations, an underbrush of alder and birch has
developed. This underbrush is present on all of the four forest sites,
but is only densely developed in a few locations.

The forest floor is composed of a lichen mat 5-10 cm in depth.
This thick bed of lichen is primarily Cladonia Alpestris (Caribou Moss),
with several other species in small proportions. The lichen mat is not
attached to the mineral soil by roots. Rooting systems generally are very
shallow. Even the root systems of large trees penetrate no more than
20 to 30 cm into the soil. In fact, rooting is entirely restricted to

Table 5.1

Experimental Site		Forest Density	Area (m^2)	Mean Slope (^{o})	Length (m)	Aspect (^{o})
Tundra	A	0	2810	4°	85	242
	B	0	1335	9°	49	271
	C	0	1777	5°	37	058
Woods	D	0.162	2409	7°	85	062
	E	—	1802	15°	54	215
	F	0.164	1822	5°30'	61	013
	G		1680	7°	76	244

General Site Dimensions

FIGURE 5.1

Site 'D'

Site 'E'

Site 'F'

Site 'G'
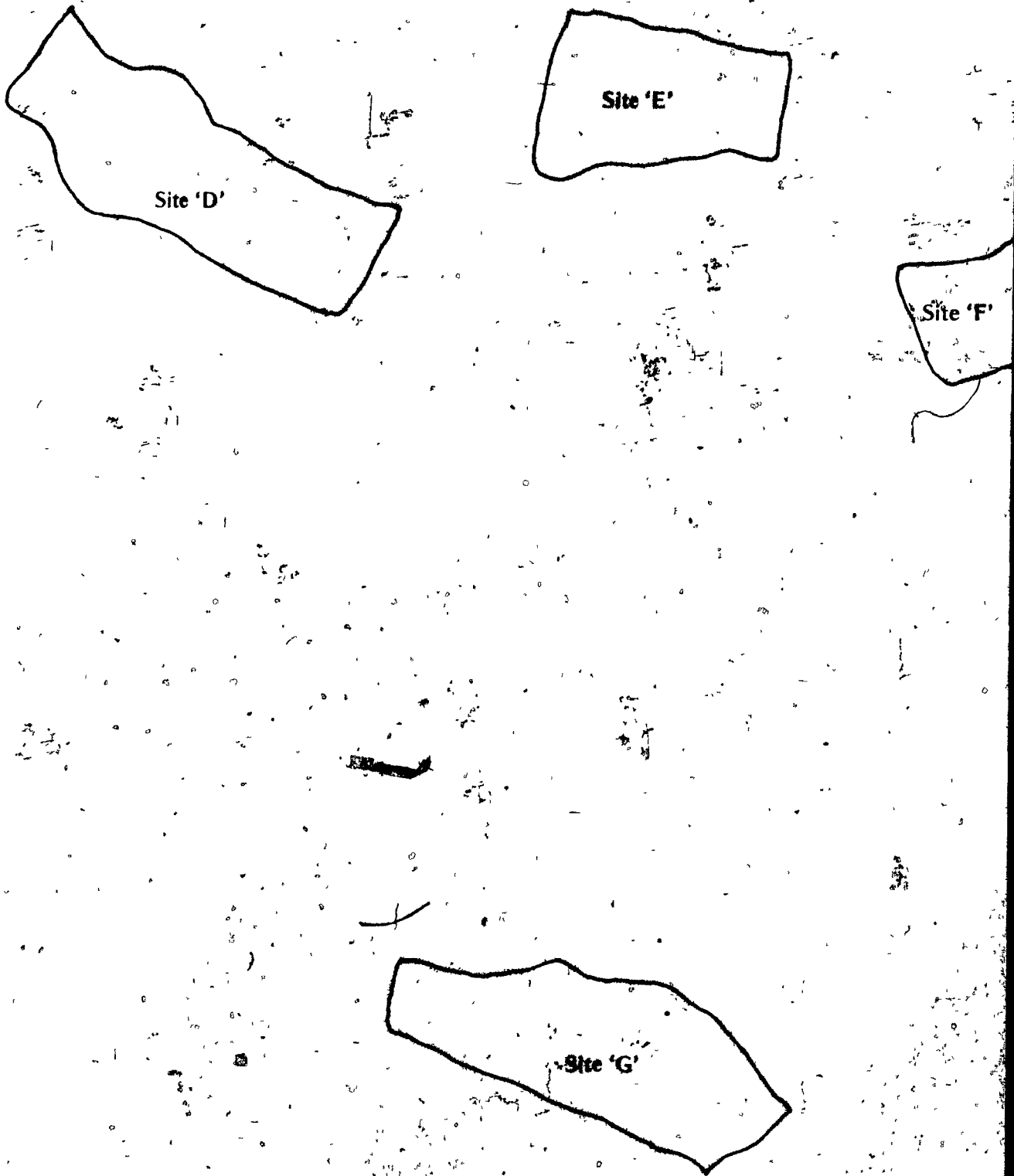
Aerial photograph of the forest site

FIGURE 5.2

Scale

50 m

North (true)

Site 'F'

Anemometer *

Radiometers

Trench

Gauge House

Gauge House

Trench

Site 'G'

Anemometer *

Gauge House

Trench

Anemometer *

Site 'E'

Mine Road

Central Meteorological Site ⊠

Radiometers

Anemometer *

Site 'D'

Map of the Forest Sites

Gauge House
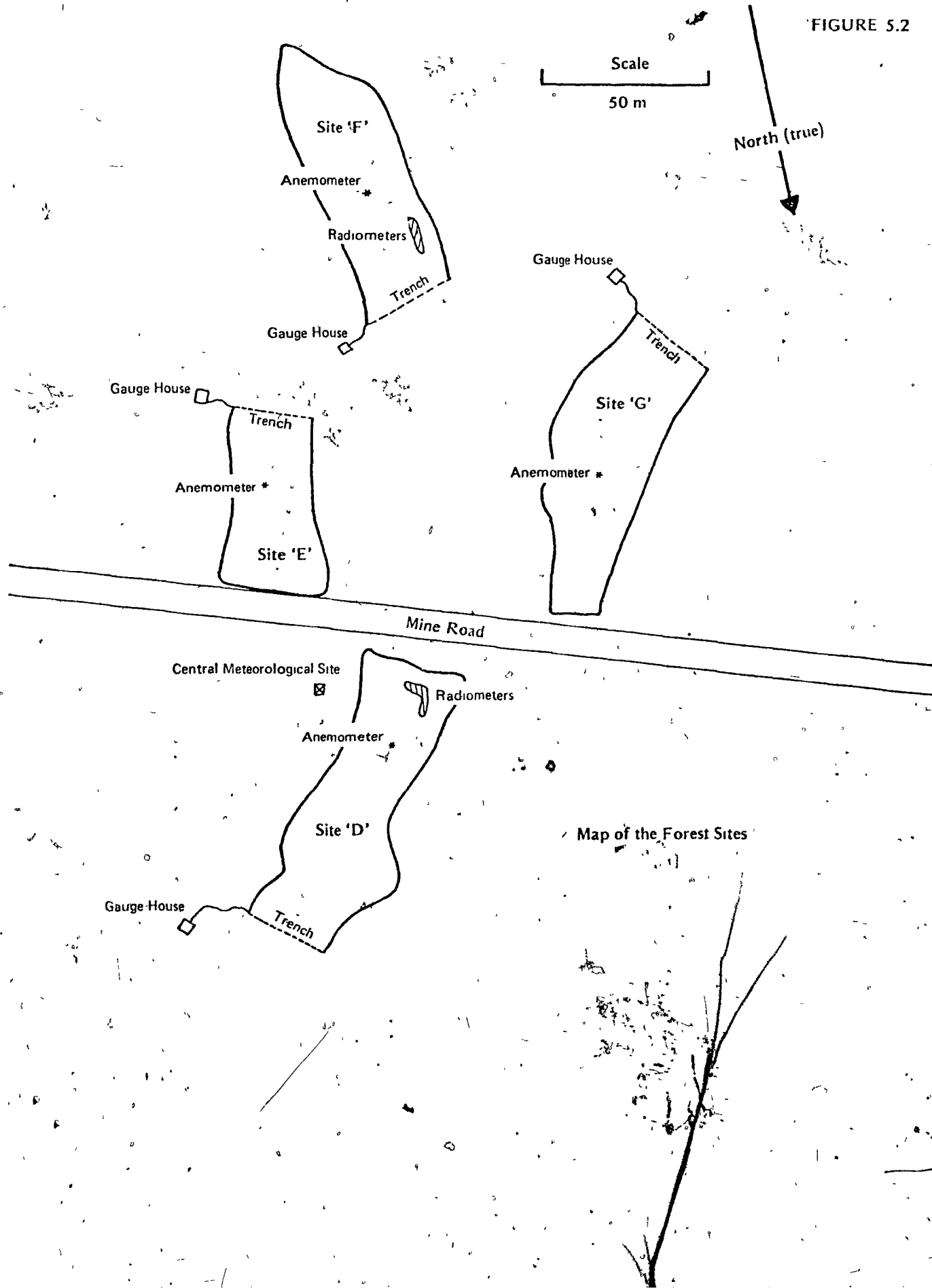
Trench

FIGURE 5.3

Slope Profiles of the Forest Sites

'D' Average slope 7°

T

'E' Average slope 15°

T

5 m. | 5 m.

Scale

'F' Average slope 5°

T

T : Collecting trench

'G' Average slope 7°

T

the surface layers. The weathering of the surface layers has resulted in the development of podsolic soils, so restricted in development that they are termed mini-podsols (Nicholson 1972). They exhibit the sequence typical of podsols: a very poorly developed humic upper layer, a grey sandy eluviated layer, and an iron rich illuviated layer. Immediately below this sequence is the parent material, dense glacial till. The local till has a blue-green silty clay matrix incorporating fragments of most of the local rock types: quartzite, dolomite, slate and chert. Fragments vary in size from gravel to boulders. The total depth of till is highly variable. In several places on ridge tops, the till is no more than 20 cm deep. At the bases of the slopes, the till varies in thickness, but is generally between 1 and 3 metres thick. The texture of the till is dense, and incorporated particles are tightly held in the silty-clay matrix. No evidence of disturbance or re-working within the till was found, and it is evident that the material is highly impermeable.

The Tundra Sites

The group of three tundra sites was situated some 22 km north of the woods sites. They were on the flanks of a small ridge (see Figure 5.6). Again the sites were as straight as possible, but some curvature can be seen in Figure 5.7.

On the tundra, the sites are free of trees, although there are some dwarf spruce, less than 2 m in height (see Figures 5.8 and 5.9) The lichen mat and soils of the tundra are very similar to those under the forest, except that both the lichen mat and the soil horizons

Closed lichen woodland

The trench is the excavation for the hydrologic instrumentation.
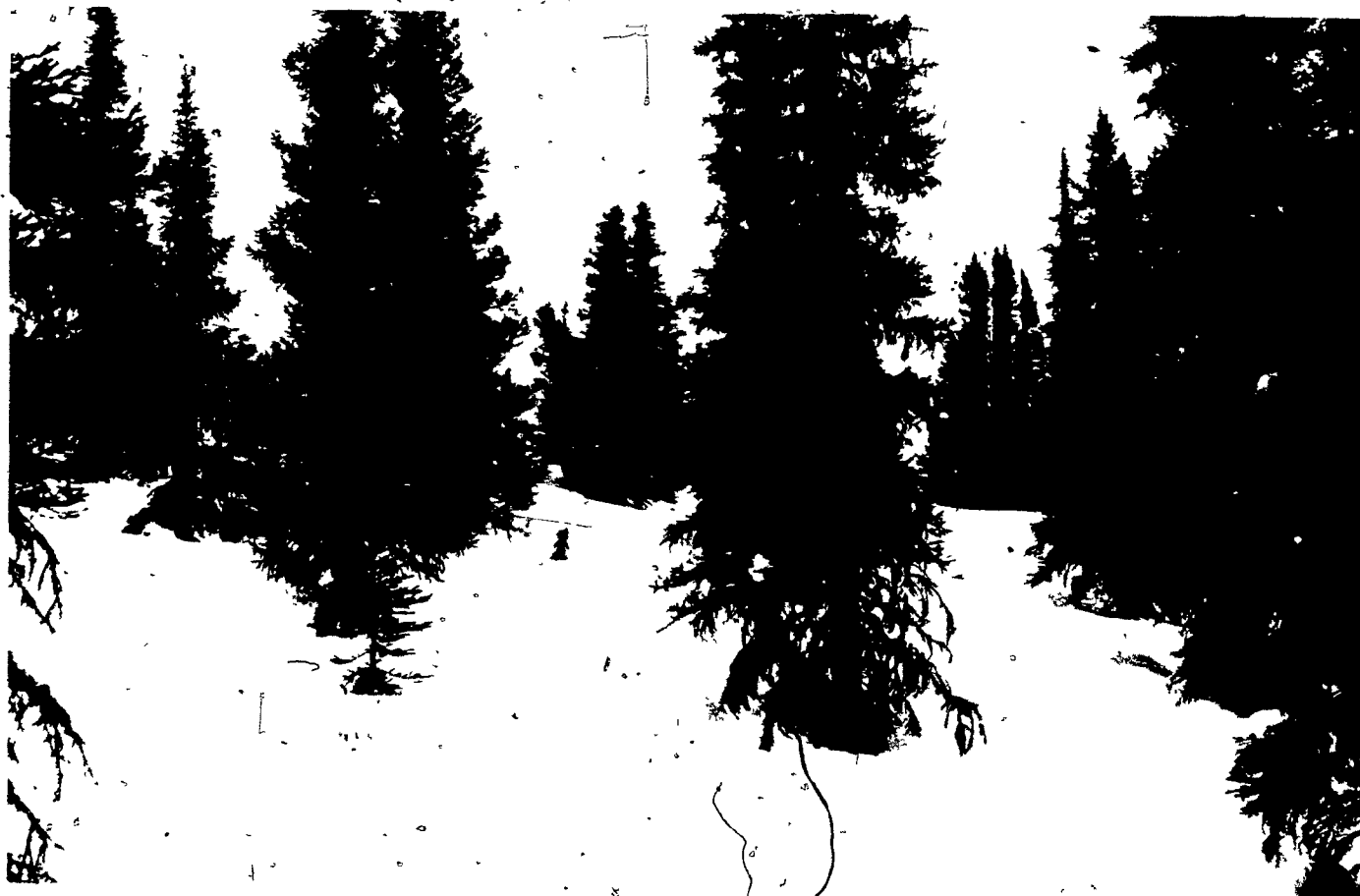
Open lichen woodland

This type of forest is dominant in the basin
with a crown density of 15-20 percent. Note
the hummocky snow surface.

FIGURE 5.5

FIGURE 5.6

Gauge House

Trench

Site 'C'

North (true)

Scale

50 m

Gauge House

Site 'B'

Trench

Site 'A'

Map of the Tundra Sites

Gauge House

Trench

Gully

Central Meteorological site ⊠

Mine Road
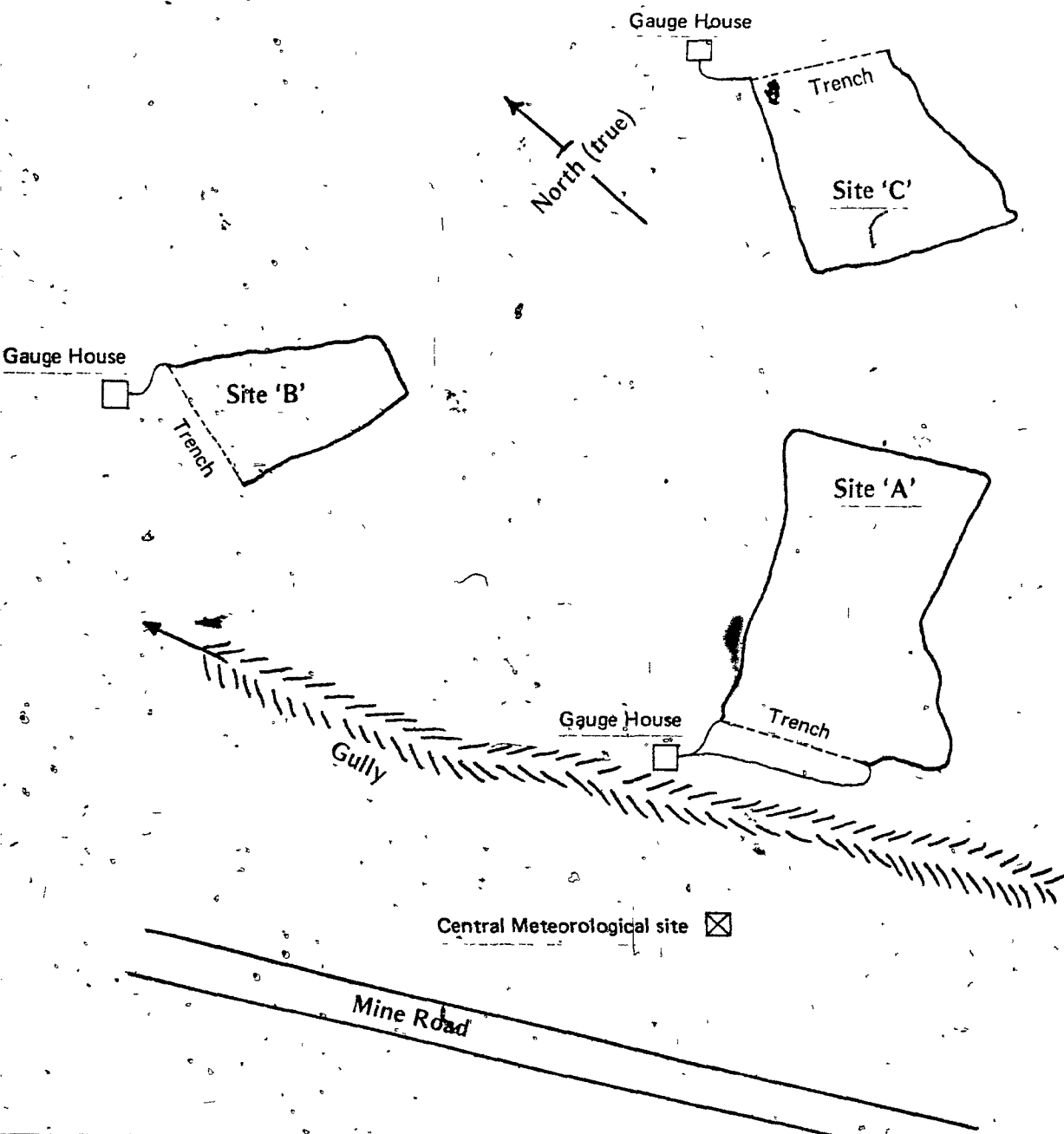
FIGURE 5.7

Slope Profiles of the Tundra Sites.

'A' Average slope = 4°

T

'B' Average Slope = 9°

T

'C' Average Slope = 5°

T

5 m

5m

Scale.

T = Collector Trench

-71

are less well developed   on the tundra. The thickness of the till

underlying the plots is even more variable on the tundra; in fact at

the ridgetops there is no till cover at all. The till is of a very

similar nature to that in the forest. Both the soil and subsoil are

thus impermeable in nature. In addition, during the two snowmelt seasons

when data were collected, the soils of both forest and tundra plots and

in the surrounding area were impregnated with "concrete" frost. This

type of soil freezing is described by Dunne and Black (1971), and

consists of solid ice within the soil. On the study plots, the ice was

so abundant that there were no open pore spaces. This type of frost

reduces the infiltration capacity of the soil to zero, so that in the

case of the Schefferville plots, there is no doubt that the soil per-

meability during snowmelt is zero. Pits excavated through a 10 cm

deep snowpack late in the melt period revealed tightly frozen soil, with

no evidence of infiltrating water. Drains excavated in the forest

showed no subsurface flow until well after the snow had disappeared from

the sites. There is no doubt, in view of these observations, that sub-

surface drainage is practically nonexistent during the snowmelt period.

Energy Balance Instrumentation

During the 1972 snowmelt season, in the forest the following

instrumentation was operated to monitor the energy balance of the

snowpack.

(1) Incoming solar radiation at the snow surface. (i.e. below the

forest canopy) was measured using five electronic (Lintronic) solarimeters.

The solarimeters were operated in series, and the combined signal from

* see next page

Photograph of tundra sites

This photograph shows the initial excavations
on Site C'. Note the clumps of dwarf-spruce.

FIGURE 5.8

Photograph of tundra sites

This photograph shows Site 'C' at peak snow accumulation.
The top of the hut is 2 m above the ground.

FIGURE 5.9

all five was measured. Several instruments were used because there
is substantial shading of the snow surface by individual trees, and
one solarimeter would not give a good estimate of the average global
radiation on the snow surface. Thus, randomly sited instruments were
used in order to get a good sample of the incoming shortwave radiation
in the forest.

(2) Solar radiation in the open was measured continuously with a
Belfort actinograph. The hourly readings from this instrument corre-
lated extremely well with those from an Eppley pyrheliometer operated
at Schefferville, 10 km north-northwest of the forest sites. The
relationship between the two sets of readings was

$$Y_E = 1.05 \, X_B - 2.02 \quad cal/cm^2/hr$$

where

Y_E = Eppley hourly (Q+q) total

X_B = Belfort hourly (Q+q) total

r = 0.944

r^2 = 0.890

σ_e = 7.4 cal/cm^2/hr

N = 632

The actinograph, being simpler than the electrically powered pyrhelio-
meter, furnished an uninterrupted record, which was used to complete the
Eppley record.

---

(3) A continuous record of the diffuse component of global radiation was also measured at Schefferville using a shaded pyrheliometer.

(4) Albedo was measured in the woods using two Lintronic sensors, are facing up measuring incoming shortwave radiation and are facing down measuring reflected shortwave radiation.

(5) Net allwave radiation was measured in the forest using five Funk-type net radiometers in series. Again, in order to obtain a better sample of the net radiation, the five instruments were placed at random, and the combined signal was measured.

(6) Hourly wind-run was measured at the central meteorological site in the woods, using a Cassella 3-cup (8 cm) recording anemometer placed 2m above the snow surface. This instrument has a relatively high stalling speed (approximately 0.2 m/s), but since the mean windspeed during both seasons is in the order of 2.5 m/s, this should not affect the results adversely. Wet and dry-bulb temperatures were measured hourly during the day, using an Assman aspirated psychrometer. These wet and dry-bulb temperatures were used to provide a record of atmospheric vapour pressure (List, 1966). During periods when the Assman record did not exist, a record of dry-bulb temperature, wet-bulb temperature and vapour pressure was generated from the thermohygrograph record. The thermohygrograph was a standard Lambrecht instrument, situated in a Stevenson screen 2m above the snow surface.

On the tundra during the 1972 melt season the following energy balance instrumentation was operated.

(1) A Belfort type actinograph was used to measure global radiation

(2) Atmospheric temperature and vapour pressure were measured as in the forest.

(3) Hourly wind-run was measured using a Cassella recording anemometer at 2m above the surface.

In the 1973 season, meteorological observations were made only in the woods, for reasons discussed later. During this season, the same energy balance parameters were measured as in 1972 in the forest.

During an additional field season in 1974, the variation of 2m windspeed between the woods sites was assessed by placing five Cassella anemometers in the woods, and at the central meteorological site, and one on each of the four plots. The results of this survey are discussed on page 105.

Hydrologic Instrumentation

In 1972, at each of the sites, the following hydrologic measurements were made.

(1) Snowpack depth and daily melt.

The amount of snow on each of the plots was measured daily using depth measurements at 15 snowstakes on each site. Surveys of snow density (10 point measurements per site) were carried out on alternate days using a 9 cm diameter Adirondack snow sampler and a spring balance. The average snow density obtained from these figures was used to convert the 15 - point depth estimates into water equivalents. The estimates of water equivalent obtained from this method are rather

imprecise because of sampling errors, operator errors, and errors
caused by varying snow conditions. The errors in the snow tube
measurements are possibly in error as much as 2 cm per day, or 40%
of the maximum observed daily melt, computed from daily runoff totals.
Such measurements were too imprecise for-hydrologic work of the kind being
attempted in this study.

(2)   Runoff

During the first field season, an attempt was made to measure two
separate runoff components; surface runoff and subsurface flow (see
Figure 5.10). The surface channel, designed to intercept surface runoff,
consisted of heavy gauge polyethylene sheet buried at its upslope edge
about 3 cm into the mineral soil. The back of the channel was formed by
a 20 cm wide board supported by stakes driven into the ground. This
channel sloped down to an outlet, and the water was piped from there to a
gauge house (see Figures 5.2 and 5.6).

In order to measure the subsurface drainage, a ditch 45 cm wide
and approximately 1 m deep was excavated down to subsoil that was clayey
and almost impermeable. The bottom of this trench was carefully graded
and the base and back of the trench lined with heavy duty polyethylene
sheet. A drain tile was laid in the trench and covered with gravel.
The trench was backfilled, and the resulting spoil heap covered with
polyethylene sheet in order to prevent the entry of surface water. The
drain tile routed water to the gauge house.

Flow from the surface channel and the subsurface drain was passed

FIGURE 5.10

Hydrological Instrumentation

surface channel

Polyethylene Sheet

Hydrologic Instrumentation in 1972

Polyethylene Sheet

Backfill

mineral soil

lichen mat

drain tile

gravel blinding for drain tile

Ditch

bentonite

embankment

Hydrologic Instrumentation in 1973
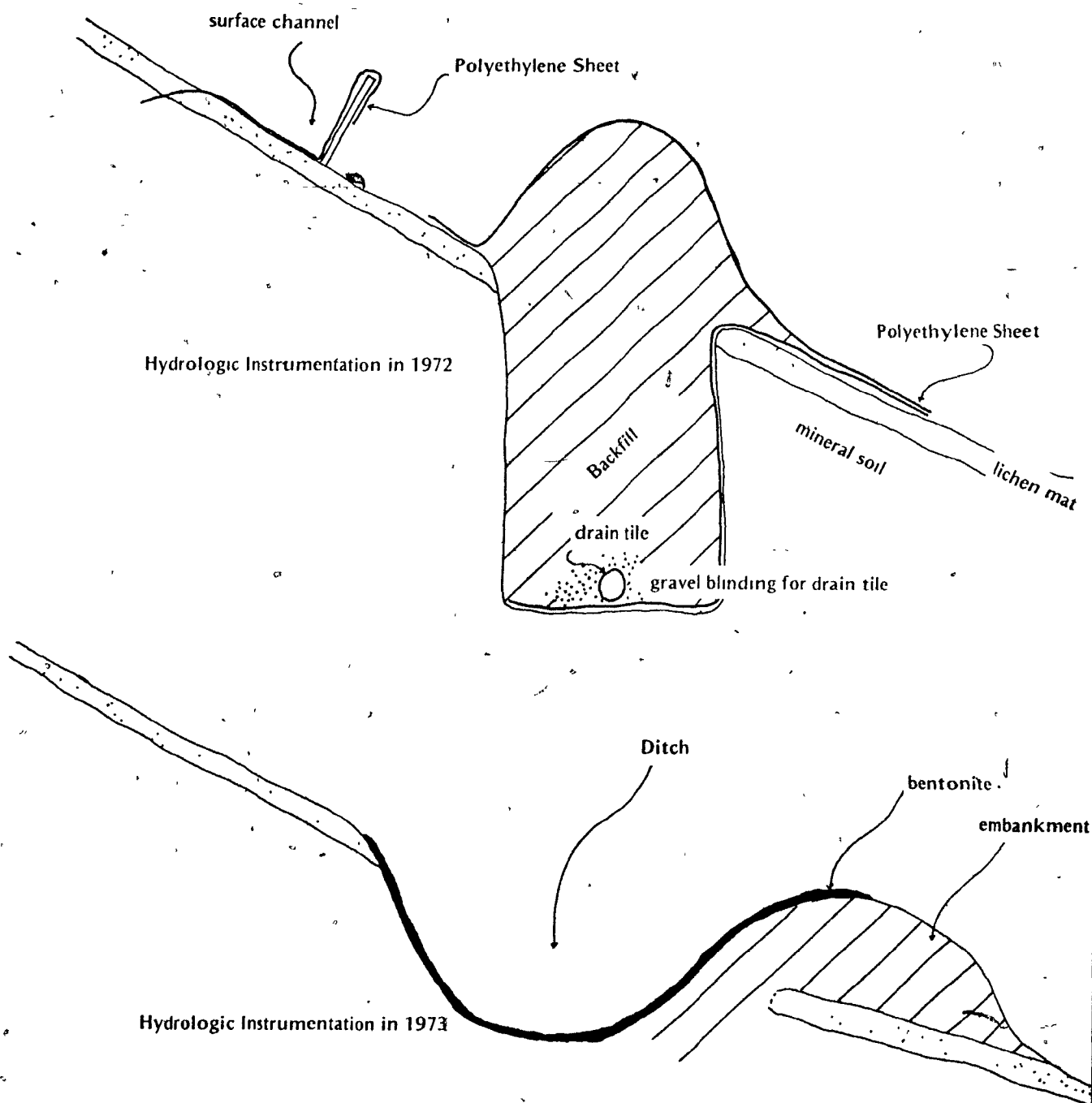
through weir boxes with calibrated 8° 'V'-notch weirs. A continuous
record of stage at the weirs obtained with two Belfort FW-1 water-
level recorders gave a continuous record of discharge on each site.

For the 1973 season, both hydrologic and energy balance measurements
were made only in the woods. The reasons for this were mainly logistical.
The hydrologic instrumentation at the tundra sites was severely damaged
by flooding during the 1972 season, and it seemed probable that the
same type of damage would occur even if the sites could have been re-
constructed. In addition, the 1972 season showed that attempting to
collect adequate data at two such widely separated sites was extremely
difficult. For the 1973 season in the forest, some changes were made
in the hydrological instrumentation. One shortcoming of the runoff
measurements made in 1972 was that the polyethylene surface runoff channel
leaked badly and in an unpredictable fashion as the soil surface thawed.
An alternative surface runoff interceptor was constructed for the 1973
season (see Figure 5.10). At the base of the sites, a channel was
excavated. The sides and bottom of the channels were compacted, and then
lined with bentonite, a clay mineral which migrates into soil pores,
swells and effectively renders the soil impermeable. This modified
instrumentation worked extremely well; no leakage was seen to occur,
and a continuous record of runoff was obtained for the whole 1973 season.

Another addition to the hydrologic instrumentation made in 1973
was two flux plates. (see Figure 5.11). These flux plates were designed
to intercept the meltwater wave just before it entered the saturated layer.
Had the flux plates functioned satisfactorily, they would have allowed

FIGURE 5.11

Emplacement of the Flux Plate and Recorder.
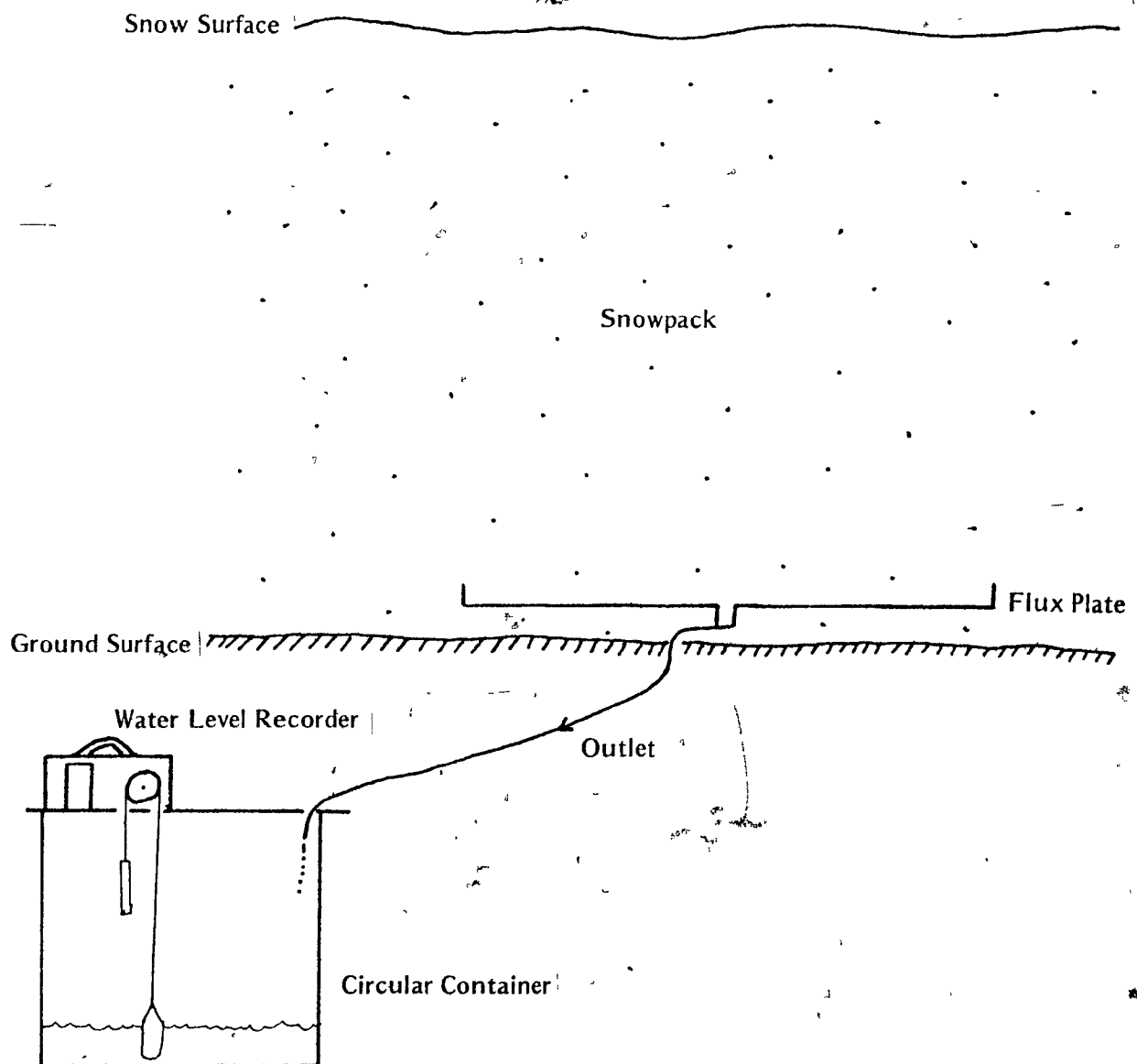
an assessment of the permeability of the unsaturated layer, as detailed
on page 142 .

The flux plate was a rectangle of sealed wood with raised edges,
and was emplaced in the snow just above ground level. This was done
in order that the plate should not intercept any water which was flowing
laterally along the ground. The flux plate was designed to intercept only
water flowing vertically in the unsaturated upper layers of the snowpack.
The outlet of the flux plate was connected to a container of known geometry.
The level of water (and therefore the volume) was monitored using a Belfort
water level recorder. The data derived from this instrumentation are a
continuous record of the rate of arrival of water at the level of the plate.

CHAPTER 6

DESCRIPTIVE HYDROLOGY

Water equivalent of the snowpack is given by the product of mean depth and mean density. A summary of these figures for the beginning of the melt season is given in Table 6.1 A. There is obviously less difference in density between sites than there is in depth (and water equivalent). This applies to both between - site variation, as shown in Table 6.1 A, and also within-site variation, as shown in Table 6.2.

Depth is most variable on the tundra. The terrain there is rough on a macro - scale, consisting of a series of small ridges and valleys. On a micro-scale, however, the terrain is quite smooth, because of the lack of trees or brush. This micro-smoothness, combined with winds averaging 5 to 6 m/sec and sometimes reaching 16 m/sec causes intense drifting of snow off ridges and into depressions. Snow depths vary from zero to 3 m, and the three figures given for water equivalent reflect this variation. Site 'A' is in the lee of a ridge, and had snow in some places deeper than 3 m. Site 'C', on the other side of the ridge, was swept almost clear of snow, the maximum snow depth on this plot being 60 cm.

In contrast to the tundra, depths and water equivalents on the four woods sites were less variable, both between and within sites as indicated by Tables 6.1 A and 6.2. The variation of woods and tundra within-site samples is shown in Table 6.2. Variation on the tundra can be seen to be very great. This extreme variability makes it extremely difficult to define the mean value for depth and water equivalent. In

Table 6.1 A

Snow Conditions at Commencement of Measurements

	Site	Mean Water Equivalent (cm)	Mean Density (gm/cm^3)	Mean Depth (cm)
(Tundra)	A	45.1	0.421	107.2
	B	23.5	0.399	58.9
	C	12.4	0.366	33.8
1972 (Forest)	D	37.5	0.325	115.4
	E	31.1	0.313	99.3
	F	45.5	0.336	135.4
	G	43.5	0.320	136.0
1973 (Forest)	D	34.2	0.290	118.0
	E	22.04	0.290	76.0
	F	30.21	0.290	104.2
	G	32.68	0.300	109.0

Table 6.1 B

15 pairs of observations

critical $r = \pm 0.25$

	D	E	F	G
D				
E	0.31			
F	0.55	0.31		
G	0.68	0.09	0.44	

Correlation matrix between daily snowstake estimates of melt on forest sites 'D','E','F' and 'G'.

Table 6.2

Tundra Site	Mean Depth	95% Confidence. Limits on Depth	Mean Density	95% limits on Density
'A'	100.9 cm n = 17	$\pm$ 32.37 cm	0.421 n = 10	$\pm$ .04
Forest Site				
'F'	111.9 cm n = 14	$\pm$ 11.06 cm	0.300 n = 10	$\pm$ .035

Within-site variability of snow depths and densities, site 'F' (forest)

and site 'A' (tundra) 16/05/72

addition to the statistical difficulty of fixing a mean depth value,
it is often difficult to read a snowstake to a consistent degree of
accuracy. Even when the same observer makes the survey each day, errors
occur. The major difficulty in making good snowstake melt estimates on
a site is that a large, variable quantity is measured twice in order to
define a small difference. The net result of all the difficulties is
that daily snowstake measurements of the change in water equivalent (i.e.
melt) are completely unsatisfactory. Negative values, which imply snow
accumulation, occur on days when runoff was measured; the snowstake
estimate of daily melt on the four forest sites gave such negative values
on 12 occasions in the 1973 season.

Table 6.1 B is a correlation matrix of the four daily melt estimates
from snow stake measurement on sites 'D', 'E', 'F' and 'G'. The values
of the coefficients are all low, and in one case the coefficient is not
significant. This low correspondence between estimates which should be
very similar confirms the impression given by the confidence limits in
Table 6.2. that the snowstake estimates of daily melt are of little utility.

The snowstake measurements collected during the two field seasons
were rejected as estimators of daily melt volumes. The values of daily
melt used to test the predictions of the heatflow model were derived by
summing flows under the daily hydrographs. This totalized runoff was then
reduced to an equivalent depth of melt (in cm) by using

$$\text{Daily melt} = \frac{\Sigma\ RO}{10.A'}\quad cm$$

$$\Sigma RO = \text{total daily runoff} \ (\ell)$$

$$A' = \text{site area} \ (m^2)$$

The hydrograph of each day's runoff was separated from that of others by plotting the recession limbs on semilogarithmic graph paper and extrapolating the recession curve. Later it will be shown that the Colbeck physical runoff model confirms the accuracy of these extrapolations. The daily runoff figures thus derived for the forest sites are given in Figure 6.1. Similar measurements were not possible for the tundra sites because of instrument failure, although some hydrographs were available from sites 'A' and 'C' which proved useful for testing the runoff model (see later). Figure 6.1 shows that melt rates were generally low in the first 8 days of the melt. During this period, site 'E' had the highest melt rates, mainly because of its more southerly aspect. All of the sites had their maximum runoff on the 10th or 11th, except 'E', where the snowpack had started to break up on May 9th. 'F' shows the most prolonged melting, since it had the most complete snow cover late in the melt. Maximum melts were 5 cm on 'D', 2.7 cm on 'E', 5.9 cm on 'F', and 4.9 cm on 'G'.

Figure 6.2 shows a 9-day hydrograph of the peak snowmelt period of 1973 on site 'G'. The general form of the hydrographs is well shown on this trace. On May 10th, the hydrograph shows the best development of the main features. The commencement of rise is at 1300 E.S.T., some 8 hours after sunrise. The hydrograph has a steep rising limb to a peak of 0.36 cm/hr at 1500 E.S.T., and an extended falling limb. This extended falling limb is best developed on days with high melt rates. The total

FIGURE 6.1

Daily Melt Rates on the Forest Sites, 1973.

Site 'D'

Snowpack starts to break up

Site 'E'

9 - Day Hydr
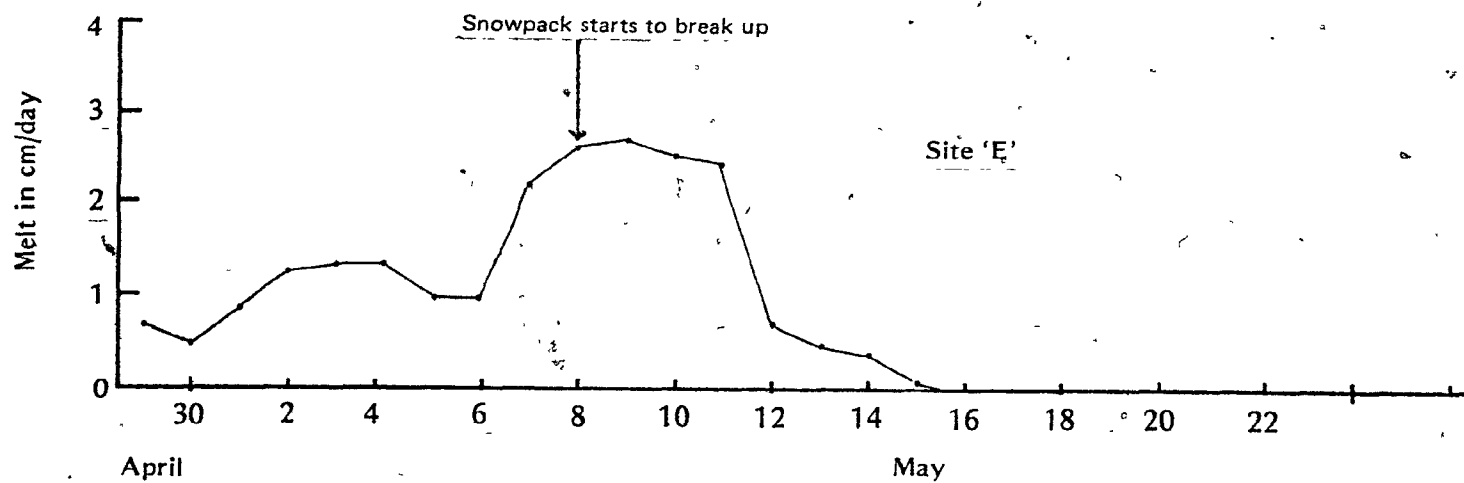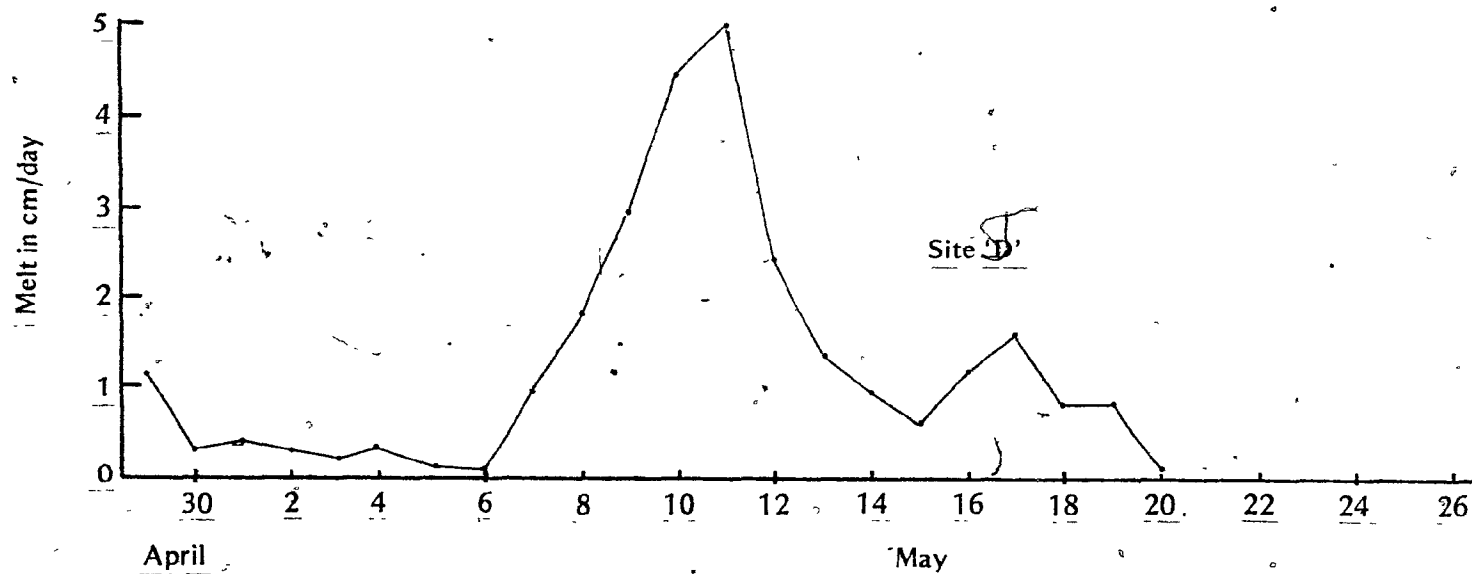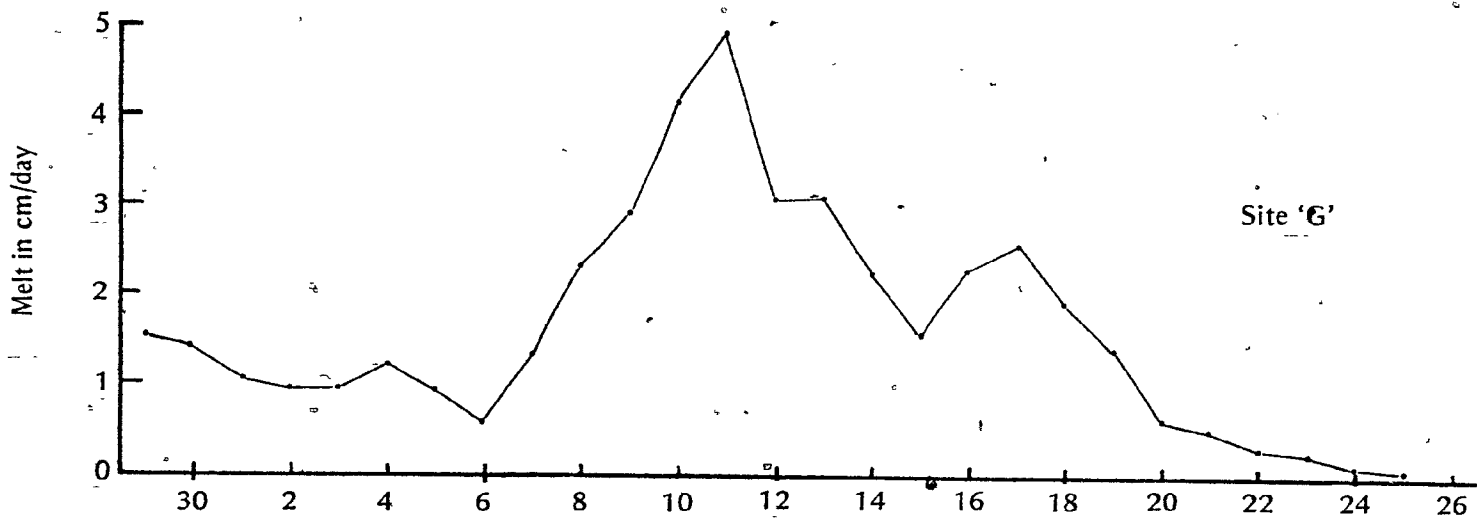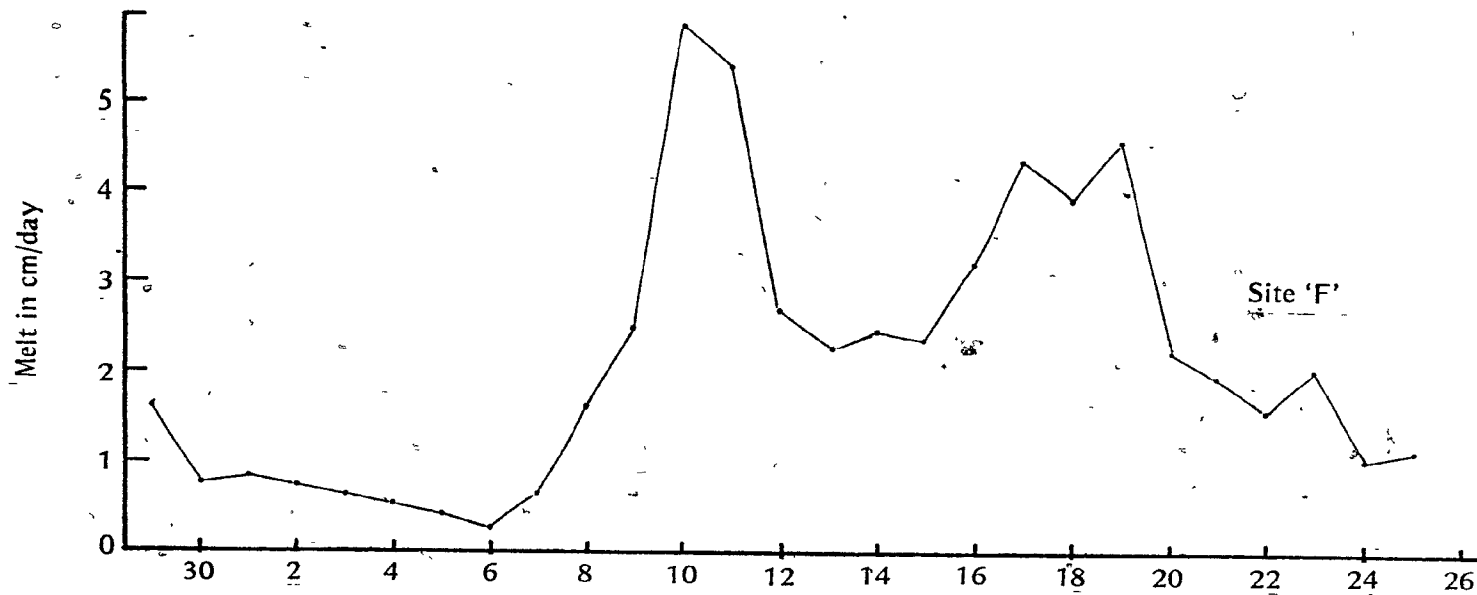
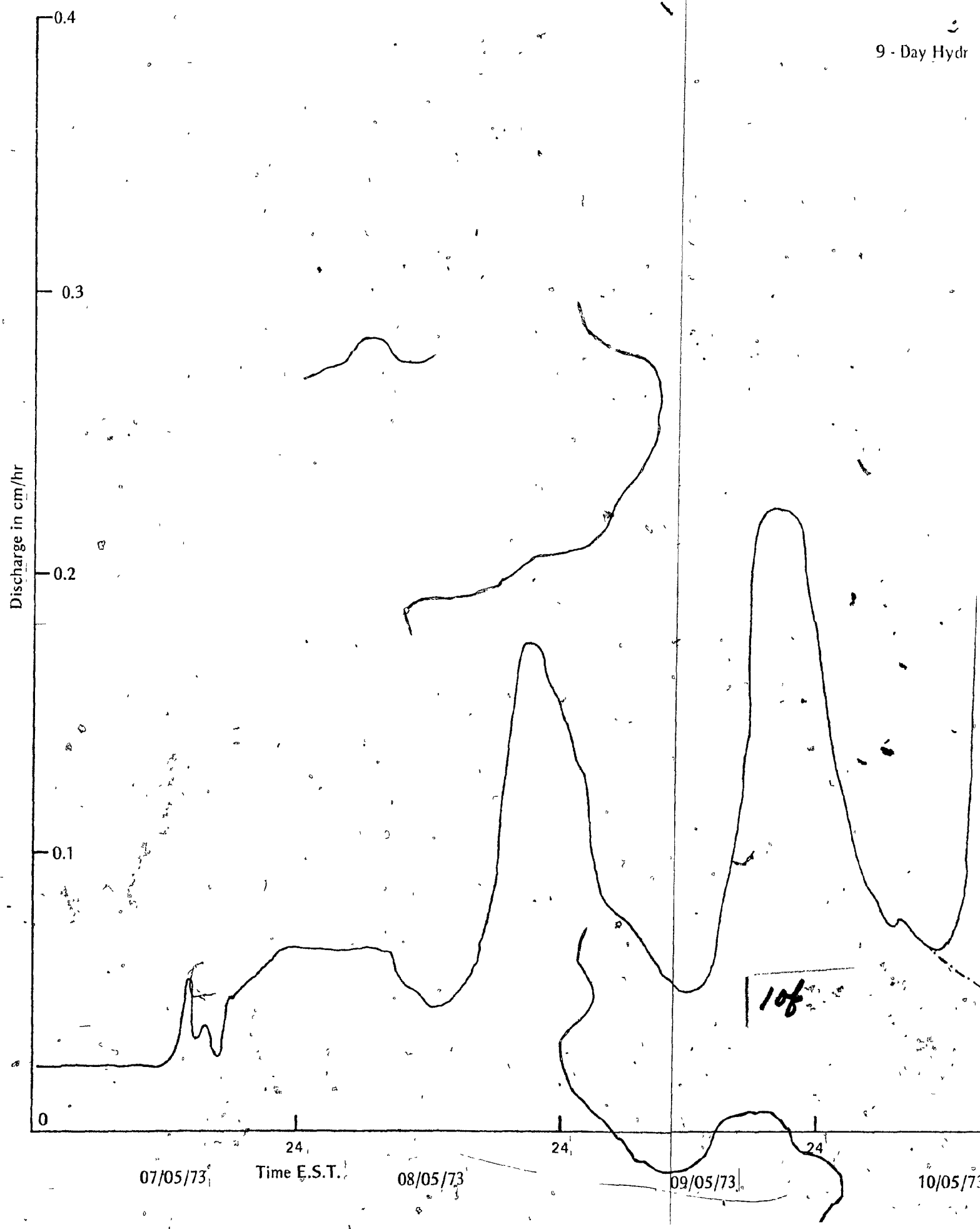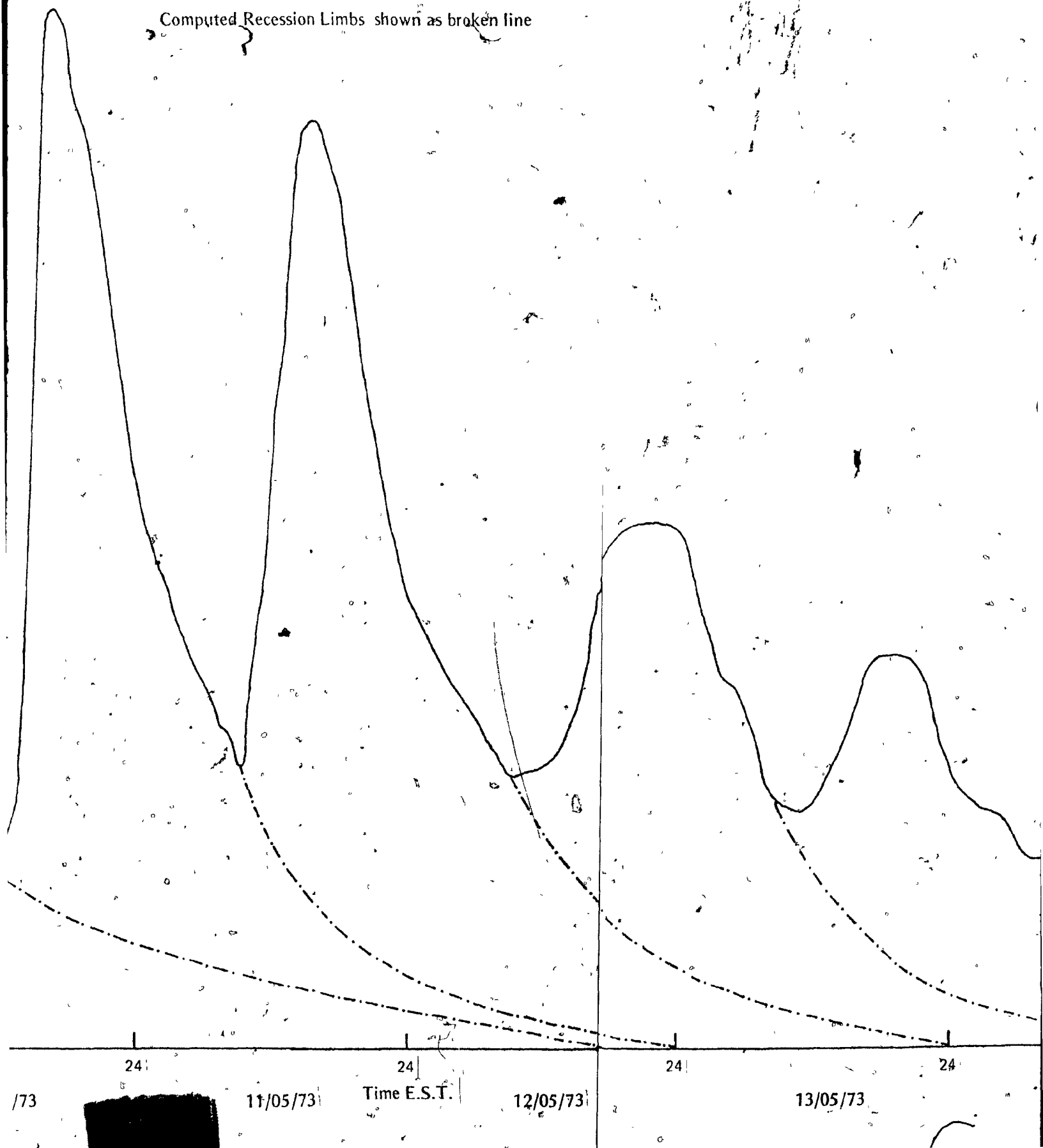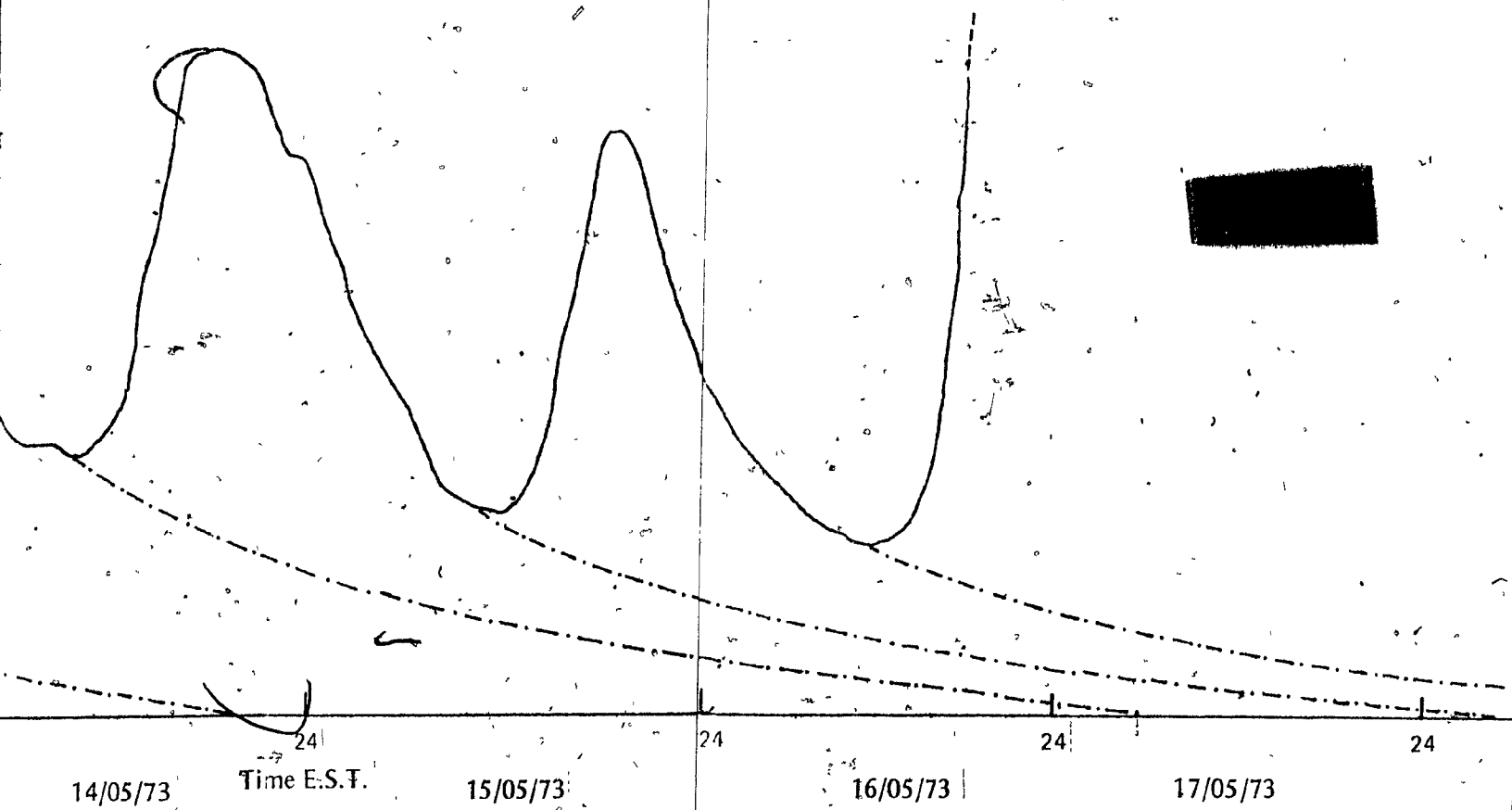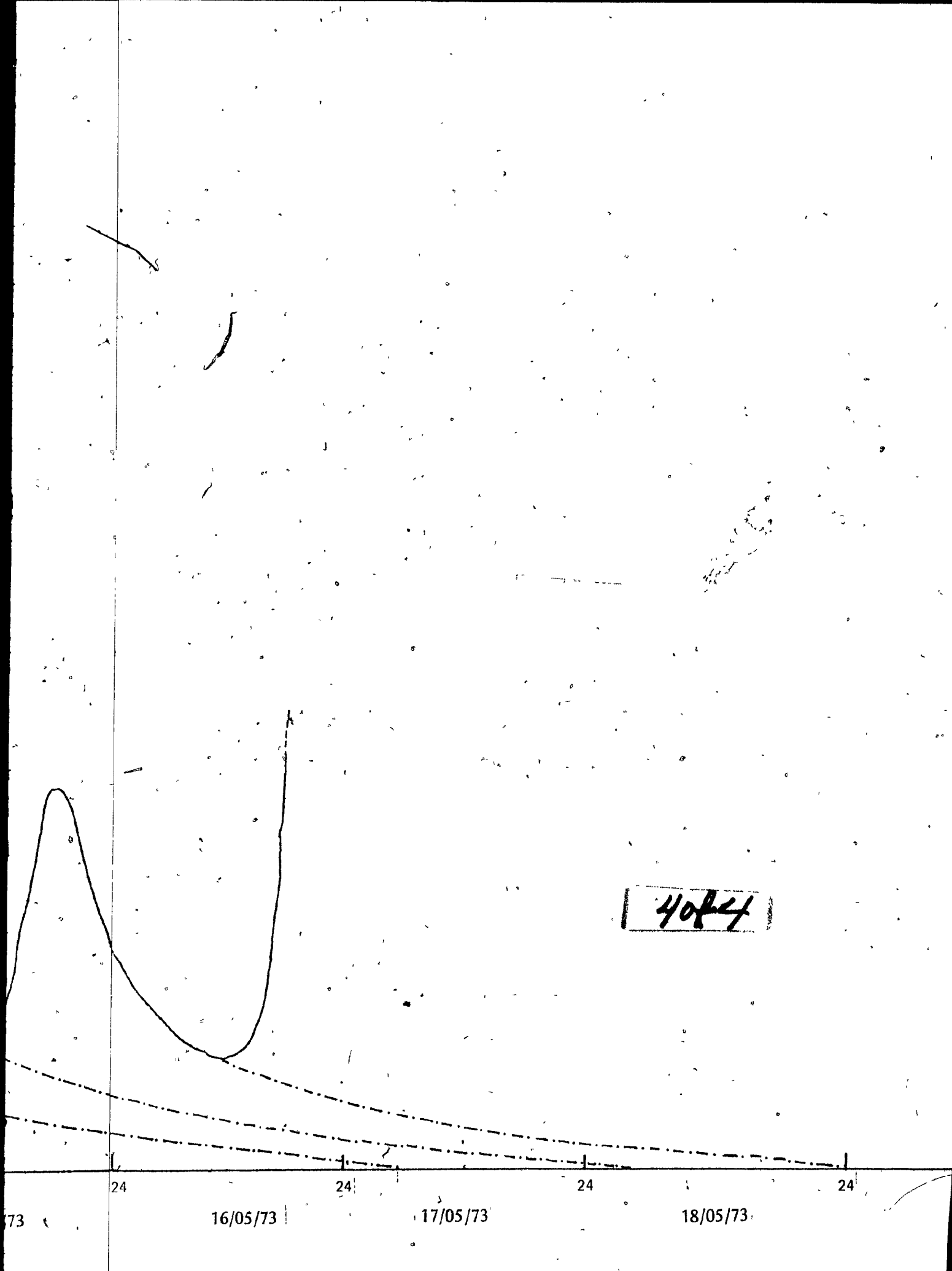FIGURE 6.2

ograph on Site 'G' , from May 7th to May 16th, 1973.

Computed Recession Limbs shown as broken line

24   24   24   24

/73   11/05/73   Time E.S.T.   12/05/73   13/05/73

24   24   24   24

14/05/73   Time E.S.T.   15/05/73   16/05/73   17/05/73

24 24 24 24

73

16/05/73 17/05/73 18/05/73

4 of 4

melt on May 10th on site 'G' was 4.8 cm. Figure 6.3 shows the hydro-
graphs recorded on sites 'D' and 'E' on the same day, May 9th 1973.
On this day the total observed melt derived from the hydrographs was
3.0 cm on 'D', and 2.7 cm on 'E'. The differences in form between
the two hydrographs are interesting. On 'E', the hydrograph begins
to rise at 1100 E.S.T., 6 hours after sunrise, and peaks earlier than
that on 'D', even though 'D' intercepts more solar radiation then 'E'
early in the morning by virtue of its easterly aspect.

The earlier peak on 'E' is caused by two factors. 'E' is a
short, steep slope (15° inclination, and 'D' is longer and less steep
7°). In addition, the snow depths at this date were 82 cm on 'D',
and 21.5 cm on 'E'. Thus, on 'E', the unsaturated and saturated path
lengths are shorter, and because the inclination of 'E' is greater, the
speed of travel in the saturated layer is greater. These two factors in
combination cause the much earlier peak on 'E'. The steepness and short
length of site 'E' also causes the more rapid draining of water out of
the saturated zone of the pack, and explains why the receeding limb on
site 'D' on the 7th of May is sustained at a higher level than that on 'E'.
Maximum rates of runoff on this day (May 9th) are 0.360 cm/hr on 'E', and
0.300 cm/hr on 'D'. The highest recorded runoff rates were 0.403 cm/hr
on 'D', 0.343 cm/hr on 'E', 0.312 cm/hr on 'F' and 0.356 cm/hr on 'G'.

It can be seen from the 9-day hydrograph (Figure 6.2) that the
baseflow levels increase later in the melt. This is a result of higher
melt rates being sustained later into the night. On some nights, melting
continued overnight, as a result of the general warming trend in the latter
half of the melt.

Observed Hydrographs on sites 'D' and 'E' for May 9th , 1973

FIGURE 6.3

Site 'D'
Site 'E'

Discharge in cm/hr

0.3
0.2
0.1
0

18   22   02   06   10   14   18   22   02   06   10

09/05/73   Time E.S.T.   10/05/73

-91-
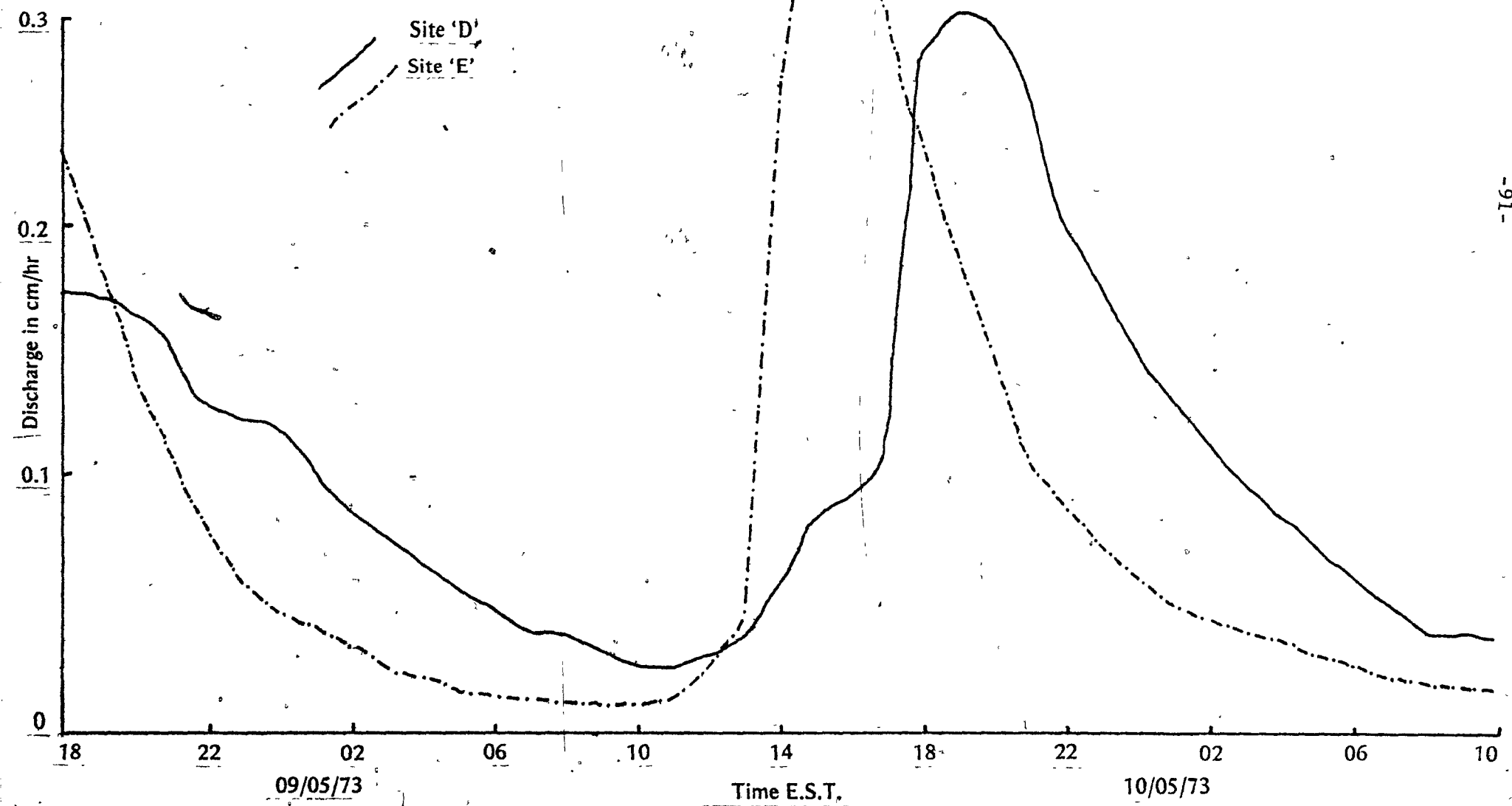
Generally the form of hydrographs on the tundra is similar to that in the forest. Peaks tend to occur later than those in the forest as a result of larger heat deficits built up overnight. These greater heat deficits are caused generally by higher wind-speeds on the tundra, combined with lower temperatures. They delay the onset of melting the next day as late as, for example 1100 E.S.T. (May 16th 1972). Peaks occur as late as 2030 hours on site 'A', which has the deepest (1 m) pack on the tundra.

As can be seen from Figure 6.1, the melt season lasted longer on some plots than on others. On the tundra in 1972, site 'C' only had 7 melt days before the water equivalent for the site was reduced to less than 2 cm. The longest season observed was in site 'F' in 1973 where melt continued for 27 days.

Because the snow cover in the woods was relatively even, the snowpack did not break up appreciably until a few days before the snow disappeared, thus the season lasted up to 20 days . On site 'E', breakup started earlier, and an estimated snow cover proportion was used to correct runoff for areal cover of snow.

CHAPTER 7

THE APPLICATION OF THE HEATFLOW MODEL

The heatflow model, outlined in Chapter 3 gives the total heat-flow to a horizontal surface when all the variables in question are known.   In practice, not all the required variables were measured continuously, and the major approximations required to apply the model are dealt with in this chapter.

Hourly values of net allwave radiation (H_R) were needed for all seven sites.   If the value of total global radiation $(Q+q)$ is known, then an estimate of H_R^- can be made (see later in this section).   Since none of the sites is horizontal, the measured horizontal values of radiation do not apply to the sites, since slope inclination and aspect affect the income of solar radiation, and therefore net radiation values on that slope.   If the energy balance, and differences in energy balance between sites are to be well defined, the first step is to compensate the horizontal radiation values for the inclinations and aspects of the sites.   A method of mapping radiation is given by Garnier and Ohmura (1968). Qualitatively, the method is as follows.   Total incoming short-wave radiation is composed of direct beam radiation (Q) and diffuse radiation (q).   The diffuse radiation may be regarded as being emitted by the whole hemisphere of the sky, and thus its value is not affected by the orientation of the recieving surface.   The direct beam portion of incoming shortwave, however, is much affected by the orientation of the slope.   In the northern hemisphere, slopes with southerly aspects are more sunny than those with northerly aspects.   If the intensity of direct

radiation on a horizontal surface at the outer edge of the atmosphere is given by I_{od}, then the intensity on a horizontal surface at the ground (I_m) is given by,

$$I_m = I_{od} \cdot C^m \qquad\qquad 7.1$$

where,

C = mean zenith path transmissivity

m = optical air mass

The slope value of direct radiation (I_s), is then given by

$$I_s = I_{od} \cdot C^m \cos (X' \wedge S'') \qquad\qquad 7.2$$

where

X' = unit coordinate vector normal to slope

S'' = unit coordinate vector expressing height and position of the sun

$\wedge$ = symbol representing 'angle between' X and S .

The conversion of this vector expression into plane geometry is somewhat complex, but the sun's position relative to the plane of the slope can be defined in terms of aspect and inclination of the slope, and sun elevation and azimuth.

In order to use this method, it is necessary to separate Q and q from total global radiation. The direct beam (Q) is then modified for inclination and aspect of the slope, and then added back to the unaltered q value, giving (Q+ q) on the slope. The inputs required, then, are various constants relating to the position of the sun, and slope orientation, and horizontal global radiation in its direct and diffuse components.

Diffuse radiation is not a commonly measured variable, and
thus some method had to be found to develop a continuous record of
it. In 1972, diffuse radiation and global radiation were measured
at Schefferville, allowing the following analysis to be performed.
Diffuse radiation was measured with an Eppley pyrheliometer equipped
with a shading band. An unshaded pyrheliometer measured total global
at the same time. The value of global radiation at any time is related
to two major factors. These are:

(i) The position of the sun, which controls both the income of
solar radiation per unit area at the outer edge of the atmosphere,
and the path length of solar radiation through the atmosphere .

(ii) Cloudiness

The values of diffuse radiation is related to path length
through the atmosphere and to cloudiness. For the period when
instrumental observations were available for both the total and
diffuse components of solar radiation, Figure 7.2 was constructed
using hourly values of the components.

The symbol I_o represents the intensity of solar radiation per unit
horizontal area at the outer edge of the atmosphere and was calculated
using the three variables describing the angular position of the sun
relative to the horizontal, that is

$$I_o = S_c \ (\sin \psi \sin \Delta + \cos \psi \cdot \cos \Delta \cdot \cos \Omega).$$

where

I_o = incoming shortwave radiation on a horizontal surface at
the outer edge of the atmosphere

S_c = solar constant = 116.4 cal/cm^2/hr

ψ = latitude   (o)

Δ = declination of the sun   (o)

Ω = hour angle   (o)

FIGURE—7.1

Definition Diagram For Radiation Mapping.

Unit coordinate vector perpendicular to slope

Unit coordinate vector representing position of sun

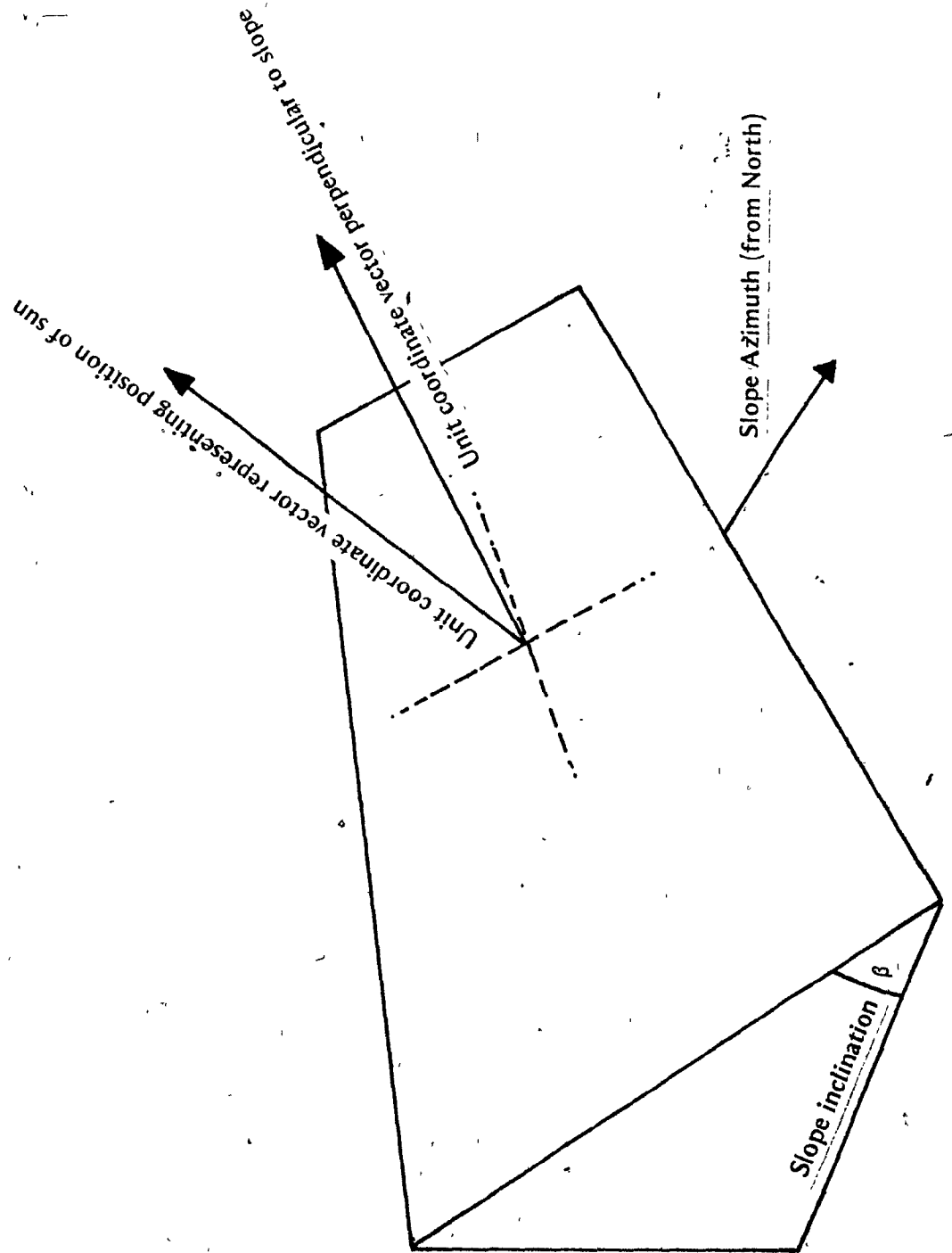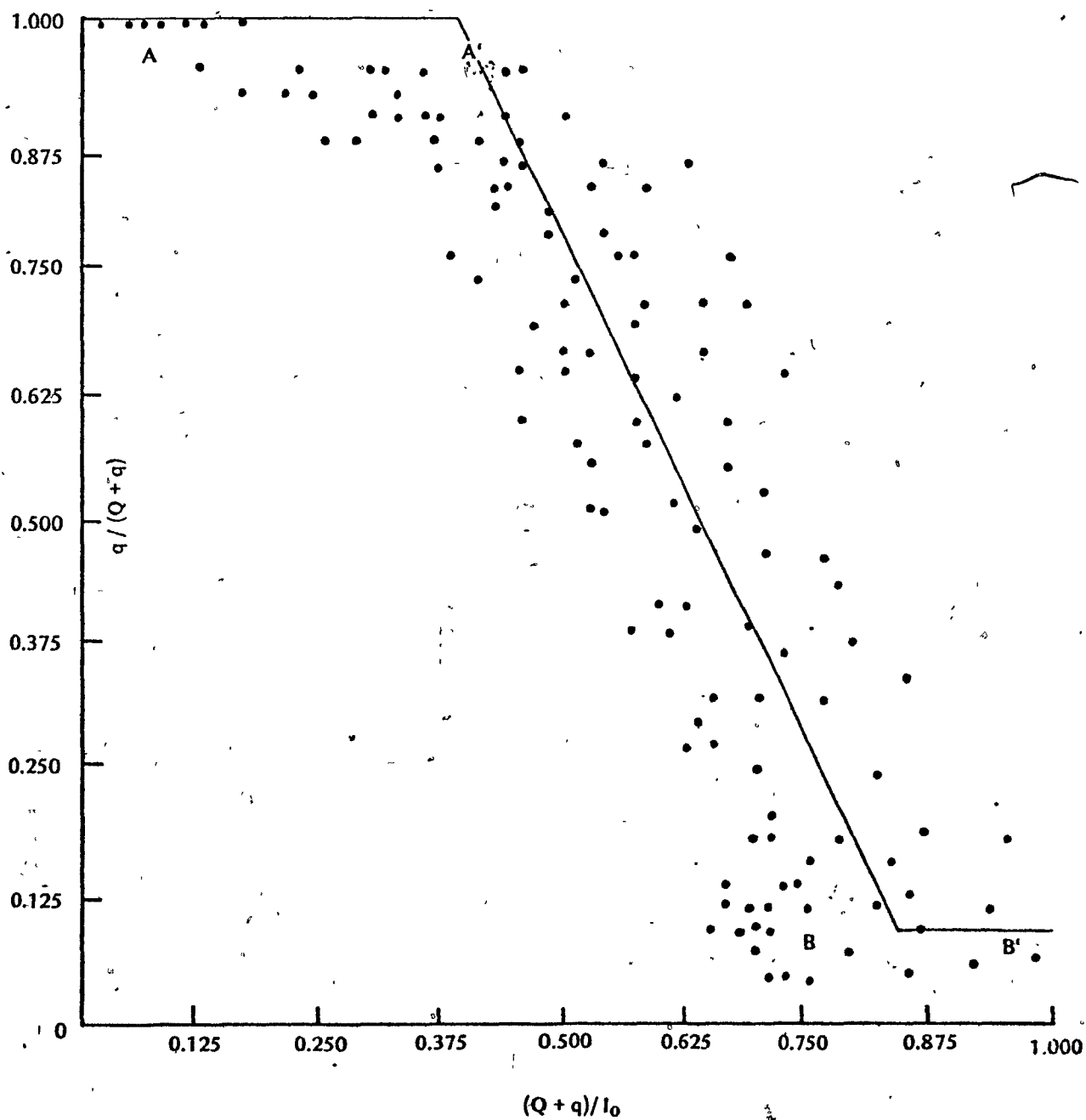Slope Azimuth (from North)

Slope inclination

β

FIGURE 7.2

Direct- Diffuse ratio vs. Cloudiness index for Schefferville 1972

Figure 7.1 shows that at values of $(Q+q/I_o)$ of less than 0.4, that is for cloudy conditions, and low sun angles, when solar radiation is generally low, it is a good approximation to say that shortwave radiation is entirely diffuse. Under these conditions, $(q/Q+q) = 1.0$. At values of $(Q+q/I_o)$ of between 0.4 and 0.85, there is an approximately linear, inverse relationship between $(Q+q/I_o)$ and $(q/Q+q)$ such that when the intensity of solar radiation increases as a proportion of the income above the atmosphere, the relative size of the diffuse portion decreases. At values of $(Q+q)/I_o$ greater than 0.85, diffuse radiation forms a more or less constant proportion of global radiation, so that $(q/Q+q) = 0.12$. This approximation concurs with the findings of Liu and Jordan (1960) almost exactly. So few values of $(Q+q)/I_o$ fall into this region that the approximation is of little importance. A regression between $q/(Q+q)$ and $(Q+q)/I_o$ for the range of $\dfrac{Q+q}{I_o}$ from 0.40 to 0.85 gives the following result,

$$(\frac{q}{Q+q}) = 1.7366 - 1.8766 (\frac{Q+q}{I_o}) \qquad 7.3$$

$r = 0.835$

$r^2 = 0.700$

$N = 119$

$\sigma_e = 0.053$

This equation together with values of I_o computed from astronomical tables, and values of $(Q+q)$ measured at the study site were used to generate a continuous record of diffuse solar radiation. The scatter

of the data is considerable, but the standard error of the estimate for Equation 7.3 shows that the method is a fairly precise way of deriving diffuse values when there are no measured data available. During the present study, the measured diffuse values were used with the Garnier-Ohmura method for mapping for the 1972 data, and synthesized values were used during instrument failures in 1972, and throughout the 1973 season when only total global radiation was measured.

The synthesis of direct and diffuse components of global radiation, and their use in the Garnier-Ohmura mapping program produces an hourly record of total global radiation on all seven slopes, compensated for slope inclination and azimuth. Figure 7.3 shows the variation in total global radiation between sites 'D' and 'E' for one day (May 25th 1972). 'D' has a northeasterly aspect and 'E' has a southwesterly aspect. The difference between the income of global on the two slopes is obvious . The maximum difference in this case is 25%, which is substantial, and demonstrates the necessity for mapping global radiation whenever environments of differing gradient and aspect are being considered in a detailed energy balance.

The conspicuous differences shown in Figure 7.3 are the result of a high direct component. Figure 7.4 shows differences under both high direct beam (sunny) conditions, and under cloudy conditions. It is clear that under cloudy conditions slope inclination and aspect have little or no effect on income of shortwave radiation.

It was noted in Chapter 3 that net radiation is rarely measured continuously. The synthesis of net allwave radiation from its components

FIGURE 7.3

Values of Global Radiation on two Slopes of Differing Aspect and Inclination.

Two Days of Global-Radiation on Sites 'D' and 'E'.

FIGURE 7.4

- Site 'E'
- Site 'D'

Total Global Radiation (Q + q) on the Slope in cal/cm2/hr

10/05/73

23/05/73

Time E.S.T.
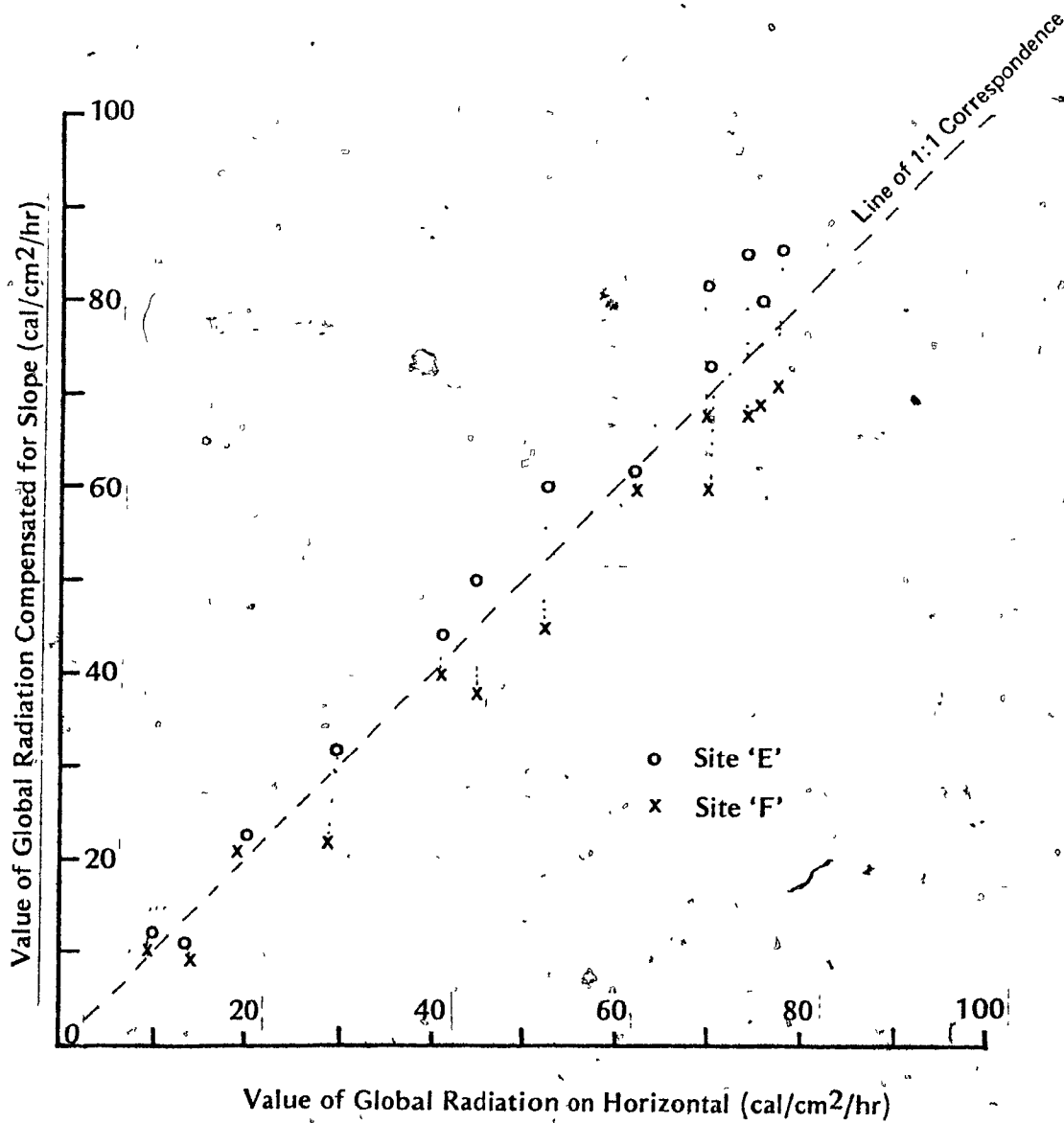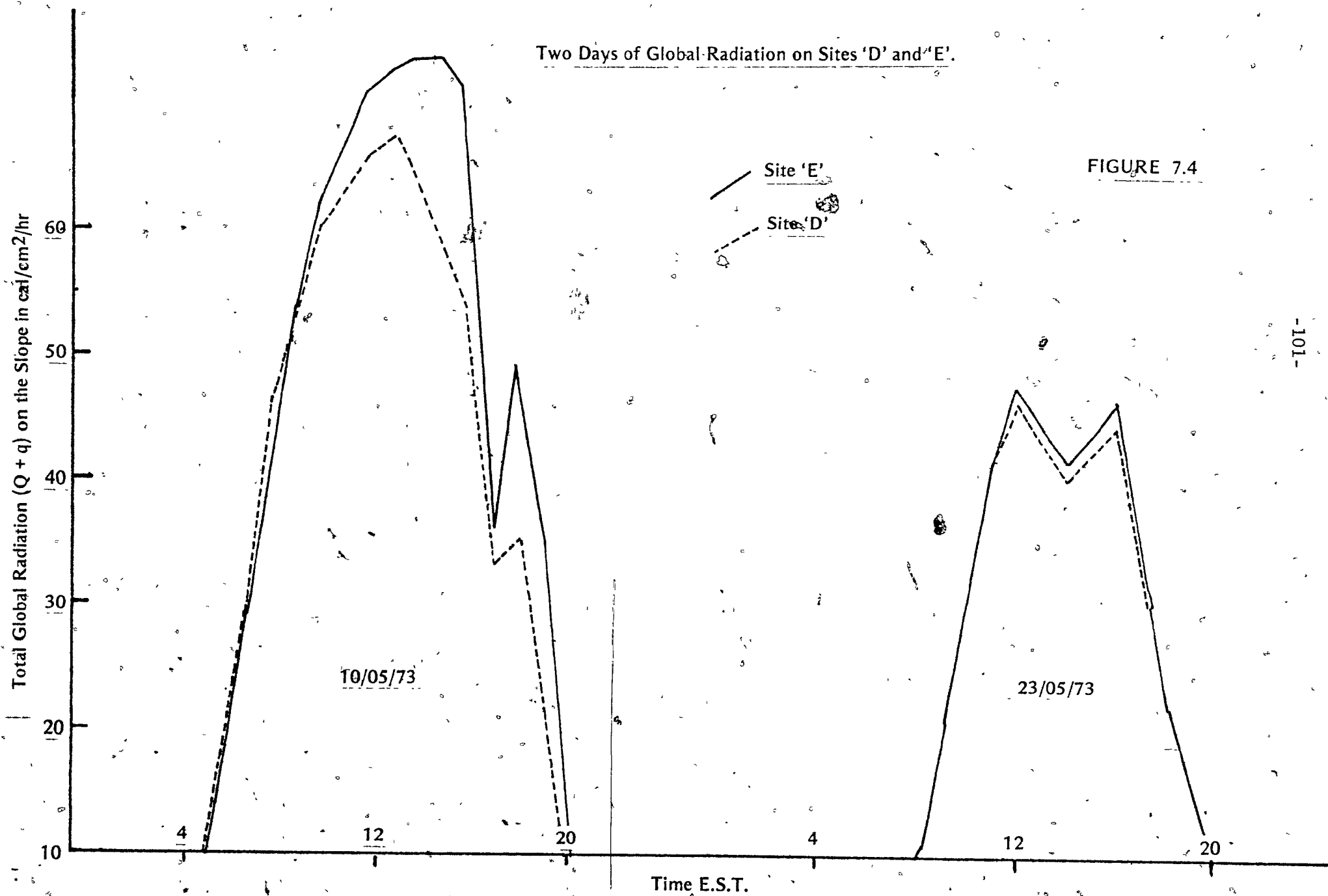
was also discussed and rejected. An alternative method of assessing H_R must therefore be found. Petzold and Wilson (1974) show that an excellent correlation exists between global radiation in the open $(Q+q)$ and net radiation under a forest canopy of a fixed density and structure (H_{Rf}). During the 1972 and 1973 field seasons relations were developed for both sites 'D' and 'F' in the forest. For 'D' the relationship is

$$H_{Rf} = -1.09 + 0.245 \ (Q+q) \qquad cal/cm^2/hr \qquad 7.4$$

where

$$r = 0.903$$
$$r^2 = 0.815$$
$$\sigma_e = 2.74 \qquad cal/cm^2/hr$$
$$N = 211$$

A similar relationship was found to exist on site 'F' such that:

$$H_{Rf} = -0.59 + 0.223 \ (Q+q) \qquad cal/cm^2/hr \qquad 7.5$$

where

$$r = 0.874$$
$$r^2 = 0.763$$
$$\sigma_e = 2.300 \qquad (cal/cm^2/hr)$$
$$N = 56$$

These two lines do not differ significantly at the 5% level, and so the two data sets were combined, giving

$$H_{Rf} = 0.996 + 0.242 \ (Q+q) \qquad 7.6$$

where

$$r = 0.901$$

$$r^2 = 0.812$$

$$\sigma_e = 2.06 \quad cal/cm^2/hr$$

$$N = 267$$

These lines are shown in Figure 7.5.

Thus using Equation 7.6, if the value of (Q+q) corrected for aspect and gradient is known for any hour then the value of net radiation for that hour can be computed directly. A similar relationship to those in the forest was shown by Petzold (1974) over an open snow surface similar to that on the tundra.

$$H_{Ro} = -0.60 + 0.150 \ (Q+q) \quad cal/cm^2/hr \tag{7.7}$$

where

$$H_R = \text{net radiation in the open}$$

$$r = 0.841$$

$$r^2 = 0.707$$

$$\sigma_e = 2.4 \quad cal/cm^2/hr$$

$$N = 107$$

Thus, for both the forest and the tundra, if we have values of global radiation we can estimate the value of net radiation with some accuracy.

One aspect of these equations is unsatisfactory. At night when global radiation is zero, net radiation in the forest is predicted to remain constant at -0.996 $cal/cm^2/hr$, and in the open at -0.60 $cal/cm^2/hr$.

FIGURE 7.5
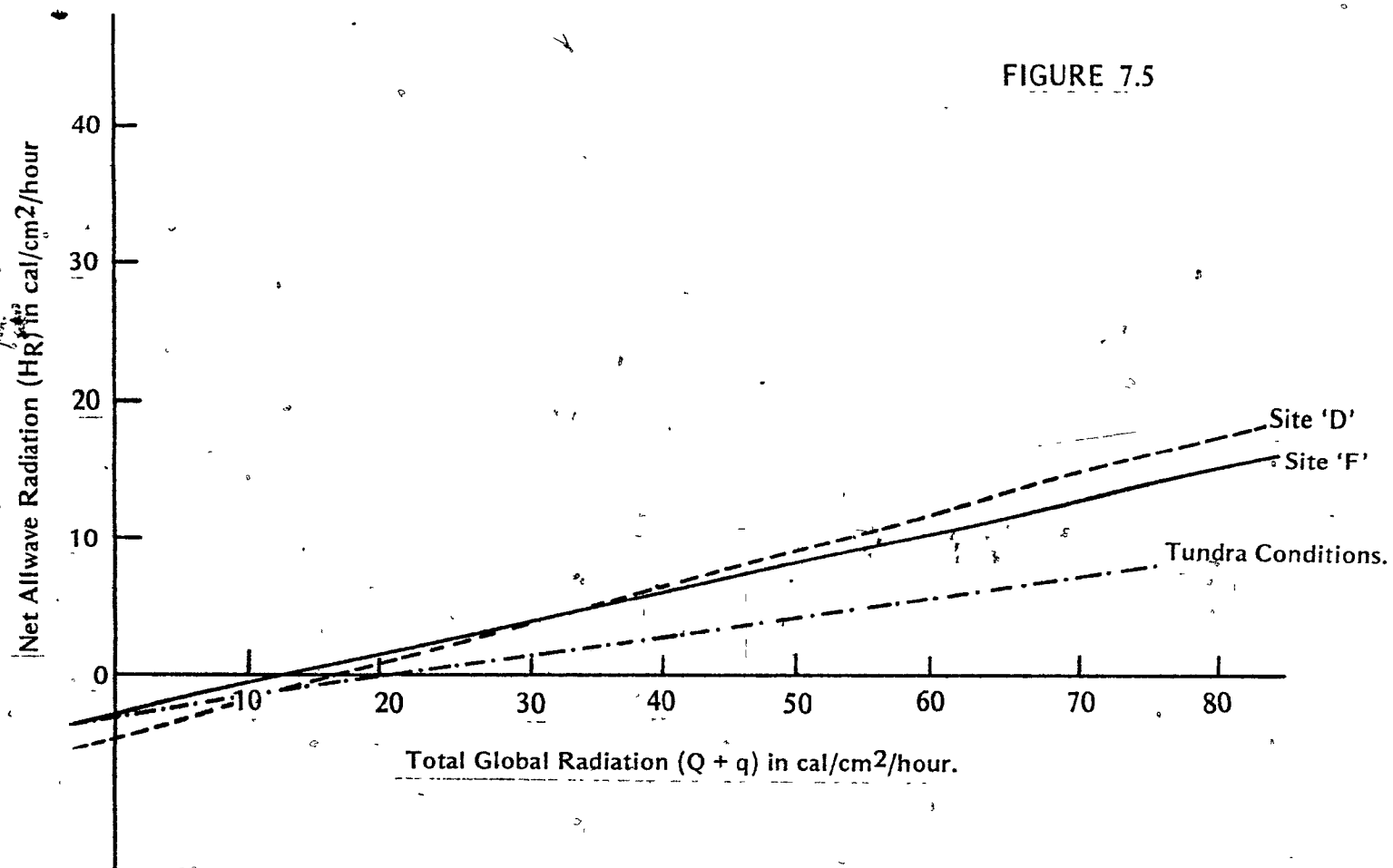
Relationships between Net Allwave Radiation (H_R) and Total Global Radiation (Q + q).

The value of this constant is derived from the regression of H_{Rf} on
(Q+q) and reflects the mean night-time loss over the whole measurement
period. In fact the longwave balance at night is far from constant,
varying greatly with cloud conditions, air temperature and vapour pressure.
Figure 7.6 shows the loss computed using a Brunt-type equation. Although
the Brunt equation was found to be unsatisfactory for general use, it
gave reasonable values of the longwave loss on the night shown in Figure 7.6.
This diagram is intended only as an illustration of the kind of variation
to be expected in the nocturnal balance. Other than the obvious over-
simplification of predicting a constant longwave loss at night, Equation 7.6
forms an excellent basis for assessing hourly net radiation.

The turbulent fluxes, defined in Chapter 3, require an evaluation
of several variables. Most of these variables were measured directly, but
some approximations were made in cases where measurement was not possible,
or not adequate. One of the major variables in the equations defining
turbulent heatflows is the windspeed at a height of 2 m above the snowpack
surface, u_z. During both the 1972 and 1973 field seasons, only one
anemometer, located at the central meteorological site (see Figure 5.2),
was used to measure u_z in the forest. There are differences between
sites in exposure, and in tree spacing and height (see Table 7.1). These
variations affect the windspeed on each site. During the spring of 1974,
a wind survey was undertaken. An "index" anemometer was placed at the central
meteorological site, and other anemometers placed at the centre of each of
the four forest sites 'D', 'E', 'F', and 'G'. Total daily wind-run was measured
at each site for eleven days. The results of the survey are shown in Table 7.2.

Nocturnal Radiation Balance Predicted by two Methods

FIGURE 7.6

Y-axis: Hourly Loss (cal/cm²/hr)

Loss Predicted Using Brunt - Type Equation

Loss Predicted Using Regression Model

X-axis: Time E.S.T.

May 10th, 1973

May 11th, 1973

-106-
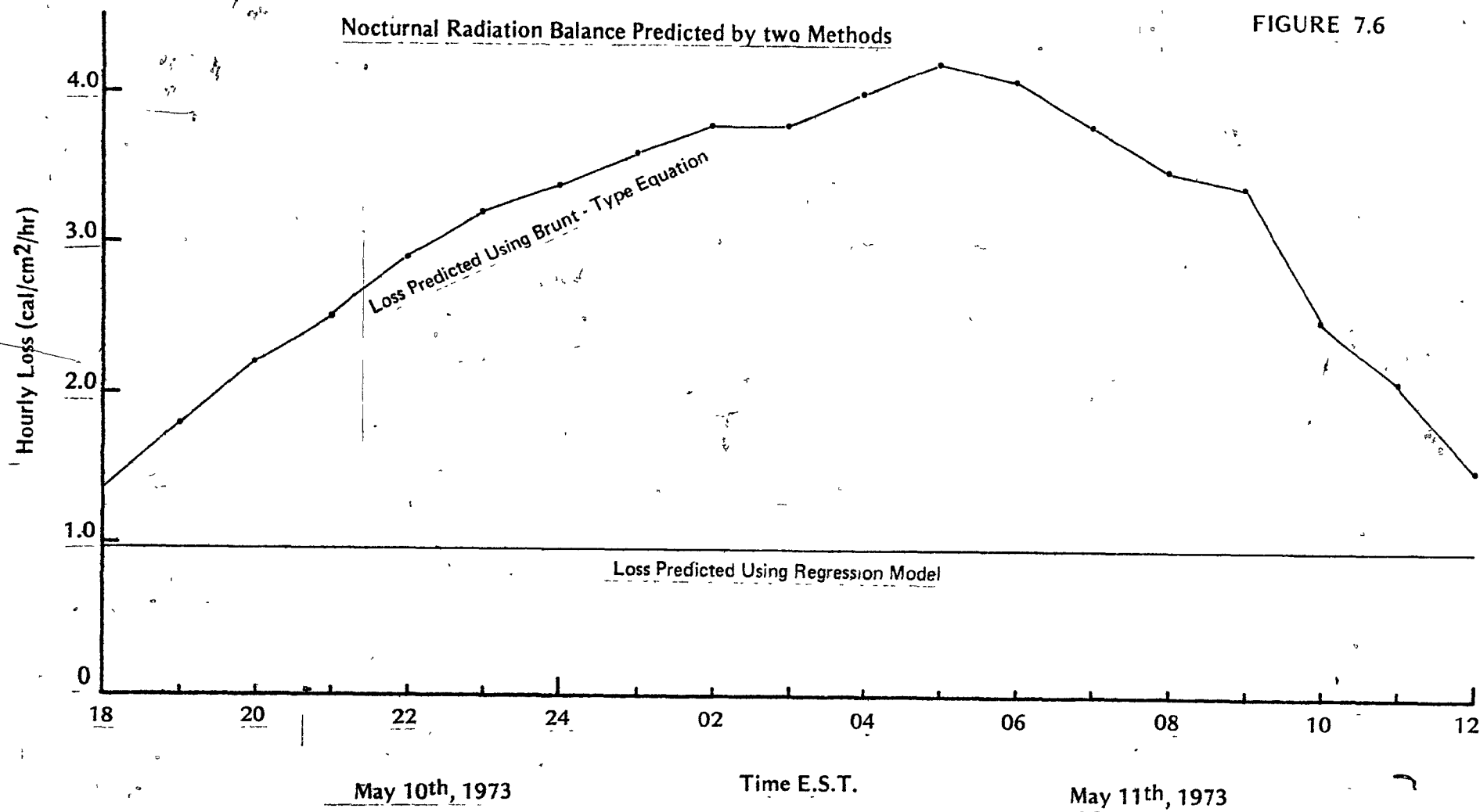
Table 7.1

Site	r (mean)	D (mean)	H (mean)
D	1.02	4.49	6.19
E	0.90	4.65	7.33
F	1.27	5.56	6.60
G	1.10	4.54	8.23

r = tree radius (m)

D = distance between trees (m)

H = tree height (m)

Table 7.2

Windspeed

Period (days)	Central Met. Site	Site 'D'	Site 'E'	Site 'F'	Site 'G'
1	1.0	—	0.603	0.670	0.660
2	1.0	0.726	0.120	0.718	0.119
3	1.0	0.925	0.287	0.890	0.525
4	1.0	0.899	0.061	0.905	0.404
5	1.0	0.750	0.285	0.833	0.367
6	1.0	0.559	0.085	0.696	0.322
7	1.0	0.683	0.229	0.640	0.360
8	1.0	0.690	0.280	0.502	0.317
9	1.0	0.600	0.131	0.534	0.322
10	1.0	0.812	0.090	0.778	0.413
11	1.0	0.910	0.435	0.517	0.562
Mean Values (compensated for calibration)	1.0	0.90	0.280	0.790	0.490
Values Adopted	1.0	0.90	0.80	0.80	0.80

Results of Wind Survey

Unfortunately the dominant wind direction during the survey
was northerly. During the snowmelt season, northerly winds are less
pronounced. The low wind speeds recorded on sites 'E' and 'G' are
open to doubt because these sites are sheltered from northerly winds.
They would not be so sheltered during the melt, and so the values
assumed for wind decrease from the meteorological site readings are as
shown in Table 7.2. Throughout the analysis these corrections were
applied to the observed meteorological site windspeed. The low values
measured on 'E' and 'G' during northerly wind conditions, however, show
that there is a large degree of uncertainty about this term in the
energy balance in areas of steep slopes and rough terrain. On the
tundra, all sites were equally exposed, and so the central meteorological
site windspeed was applied to each.

The other variable in the equations describing the turbulent ex-
changes which has to be approximated is the snow surface temperature.
This has already been discussed in Chapter 3.

Site 'E' was the only slope on which the snow cover broke up to
expose bare ground with substantial amounts of snow remaining on the plot.
Because of this, an estimate was made each day of the proportion of the
plot covered by snow. This estimate of percentage cover is used to
correct the energy-balance estimate of melt.

The final result of all the heat model computations is the hourly energy ba-
lance of seven slopes with each slope constituting a different snowmelt environ-
ment. The differences between these environments may be considerable, as shown
in Figure 7.7 and Figure 7.8.

FIGURE 7.7

Surface Flux on Sites 'D' and 'E', May 11th, 1973
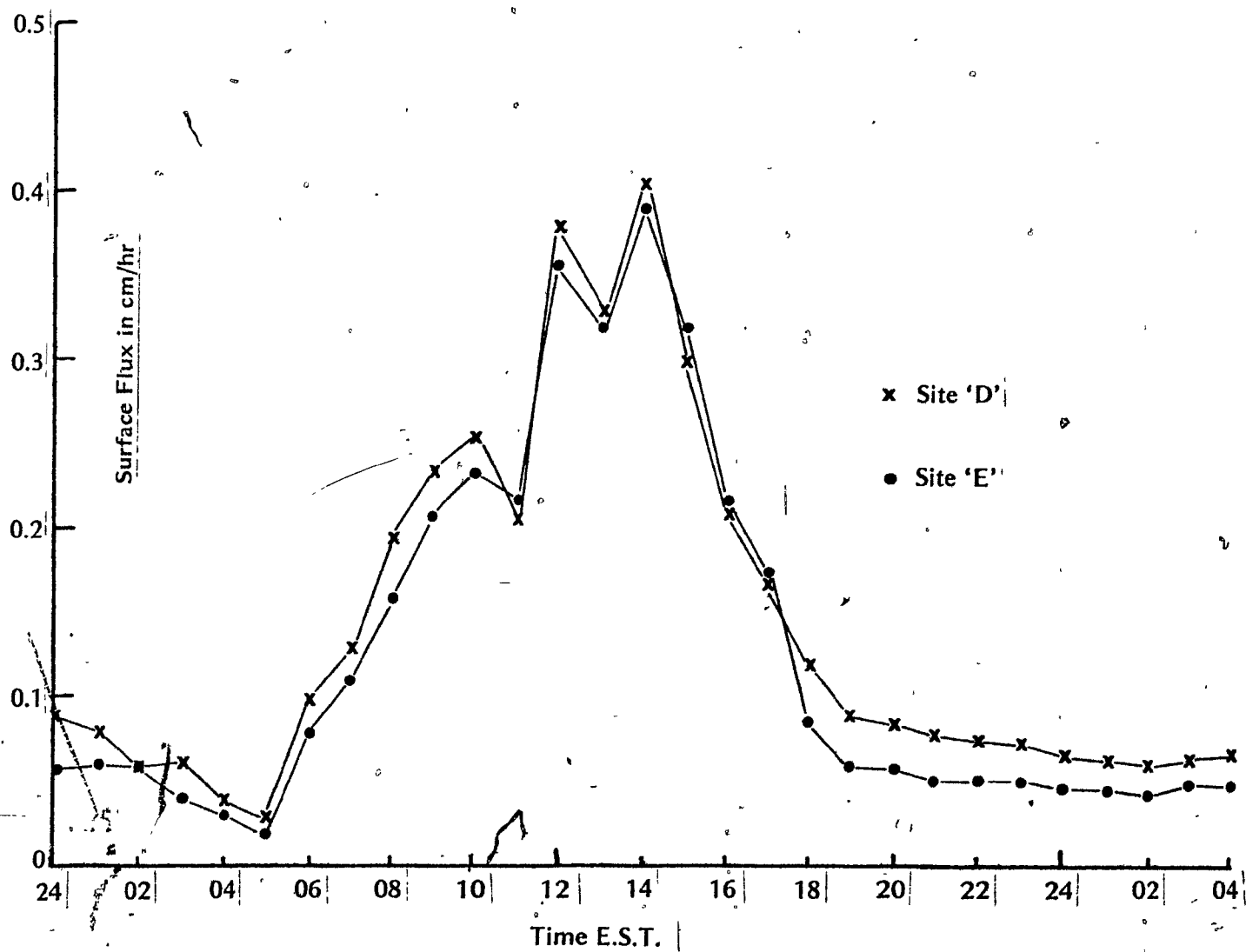
FIGURE 7.8

Surface Flux on Sites 'D' and 'E', May 4th, 1973

Time E.S.T.
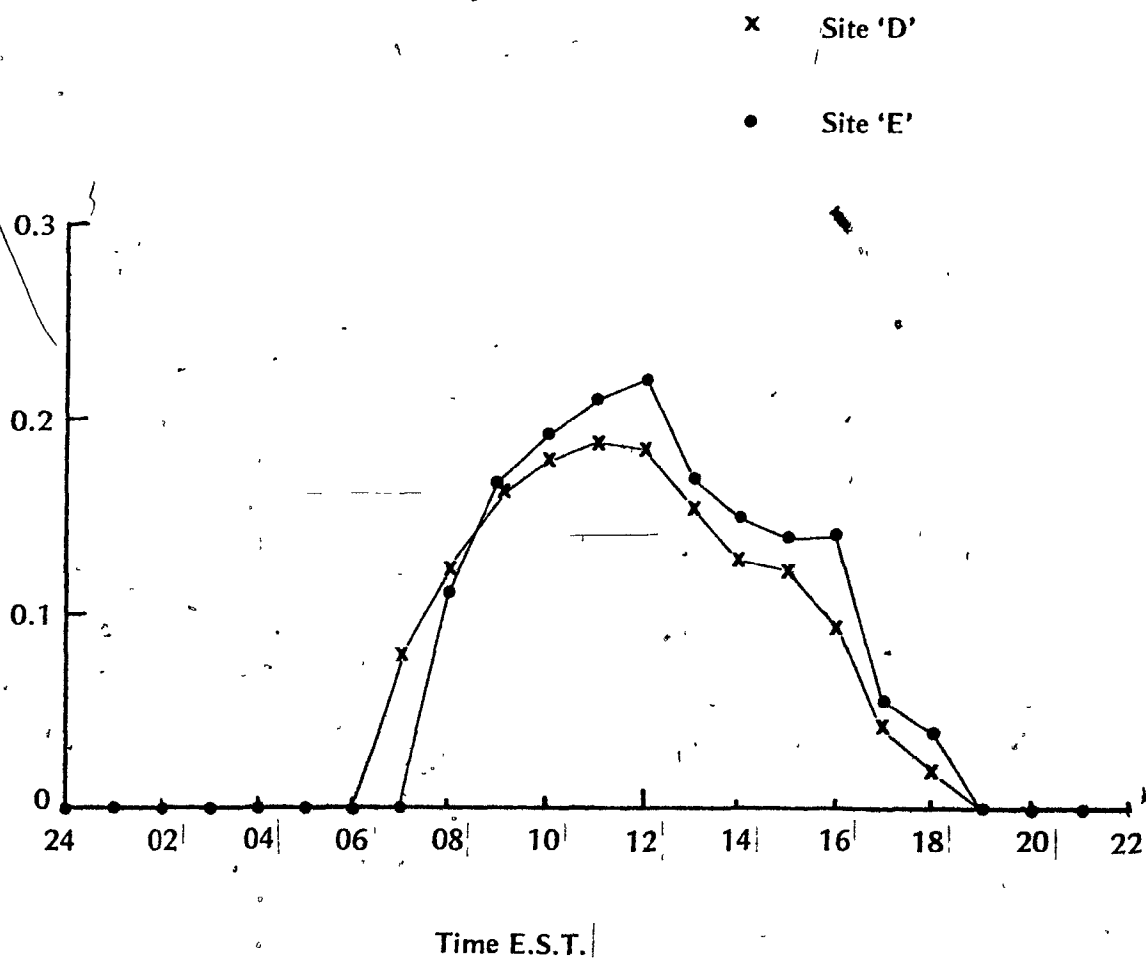
Figure 7.7 shows the melt rates on slopes 'D' and 'E' on a day

of rapid melt, due to both high radiation and high turbulent fluxes.

The sum of the turbulent fluxes is much greater than the radiation

melt, so that site 'D' with its higher windspeed (see Table 7.2)

has higher melt rates for most of the day. By contrast, Figure 7.8 shows

the computed melt rates for the same two sites during a day with high

radiation fluxes, but small turbulent fluxes. Site 'D', with its

easterly aspect, has higher levels of melt in the morning, since the

early morning sun is more intense on 'D' than on 'E'. In the middle

of the morning, however, the situation is reversed, and 'E' intercepts

more radiation than does 'D'.

Results of the Application of the Heatflow Model

Using the measurements and approximations described in the first part of this chapter, the heatflow model derived in Chapter 3 was used to predict hourly melt rates for the seven sites during the 1972 and 1973 melt seasons. The hourly values were summed to produce daily totals. For the 1973 season, when reliable daily melt totals derived from runoff hydrographs were available, the theoretical melts were compared with the observed melts. Regression of observed (Y) on the computed (X) runoff totals (in cm) for 17 days on each of the four forest sites gave the following results

Site 'D'

$$Y = -0.59 + 1.25X \qquad\qquad 7.8$$

$r = 0.93$

$r^2 = 0.86$

$\sigma_e = 0.55$ cm

$N = 17$

The regression constant (a' = -0.59) is significantly different from zero at the 5% level, and the regression coefficient is significantly different from 1.0, also at the 5% level.

Site 'E'

$$Y = 0.15 + 1.13X \qquad\qquad 7.9$$

$r = 0.89$

$r^2 = 0.81$

$\sigma_e = 0.37$ cm

$N = 17$

The a' value is not significantly different from zero at the 5% level and the regression coefficient (b) is not significantly different from 1.0, also at the 5% level .

Site 'F'.

$$Y = -0.05 + 1.32X \qquad 7.10$$

$r = .72$

$r^2 = .51$

$\sigma_e = 1.16$

$N = 17$

The regression constant (a') is not significantly different from zero at the 5% level, but the regression coefficient (b) differs significantly from 1.0 at the 5% level.

Site 'G'

$$Y = 0.66 + 0.90X \qquad 7.11$$

$r = 0.72$

$r^2 = .51$

$\sigma_e = 0.87$ cm

$N = 17$

The value of a' differs significantly from zero, and the value of b differs significantly from 1.0, both at the 5% level.

All sites combined:

$$Y = 0.07 + 1.13X \qquad 7.12$$

$$r = 0.78$$

$$r^2 = 0.61$$

$$\sigma_e = 0.84$$

$$N = 17$$

For the overall prediction, a does not differ significantly from zero, nor b from 1.0, both at the 5% level. Figure 7.9 shows the computed and observed value for all plots combined, and Figure 7.10 to 7.13 show the values of computed (X) and observed (Y) daily melt for each of the four forest sites for 17 days.

Two points are immediately apparent. First, on sites 'D' and 'E' the correspondence between observed and computed runoff is very good, as is evident from the regression equations. On site 'F', the correspondence is poor, and on 'G' moderately good, especially during the early part of the melt season. Secondly the pattern of over and under-prediction is the same on all four sites. There is a hysteresis loop with overprediction early in the melt and underprediction late in the melt. The form of the loop is a little more complicated for site 'E' because of the application of the snowcover depletion factor described earlier in this chapter on that site. Although the regression analysis shows that the predictions of daily melt from the energy budget are within generally accepted tests of precision, the generality of form of the hysteresis loop warrants some attention.

The errors causing the hysteresis could be caused by errors in either the observed runoff, or in the computed runoff. In the computation of the observed daily runoff, hydrograph separation gave recession limbs (see Figure 7.14) which extended for 50-60 hours after

FIGURE 7.9

Calculated Daily Runoff versus Observed Daily runoff . All Sites, with $z_0 = 0.005$ m

FIGURE 7.10

Calculated Daily Runoff versus Observed Daily Runoff.
Site 'D' with $z_0 = 0.005$ m

FIGURE 7.11

Calculated Daily Runoff versus Observed Daily Runoff.
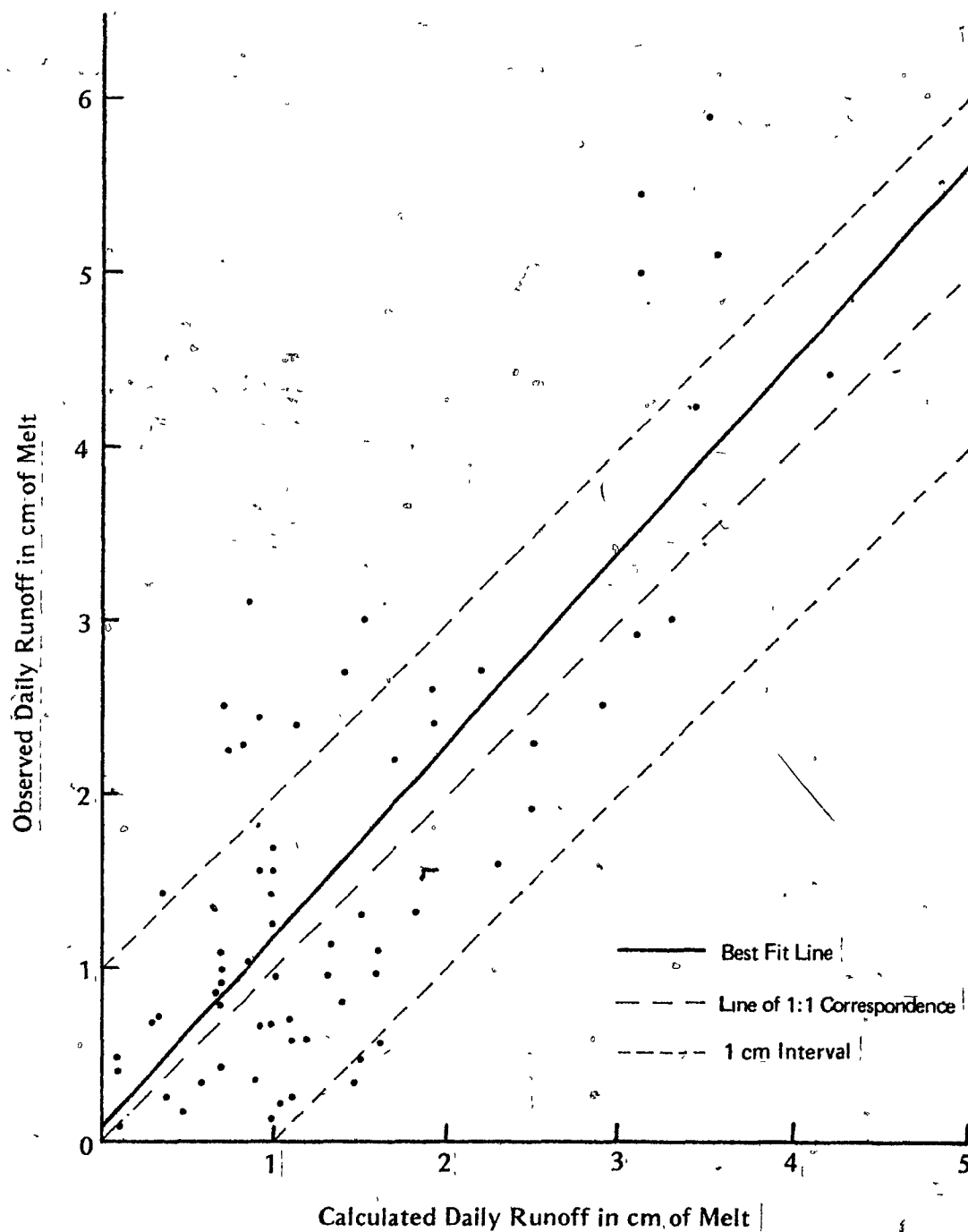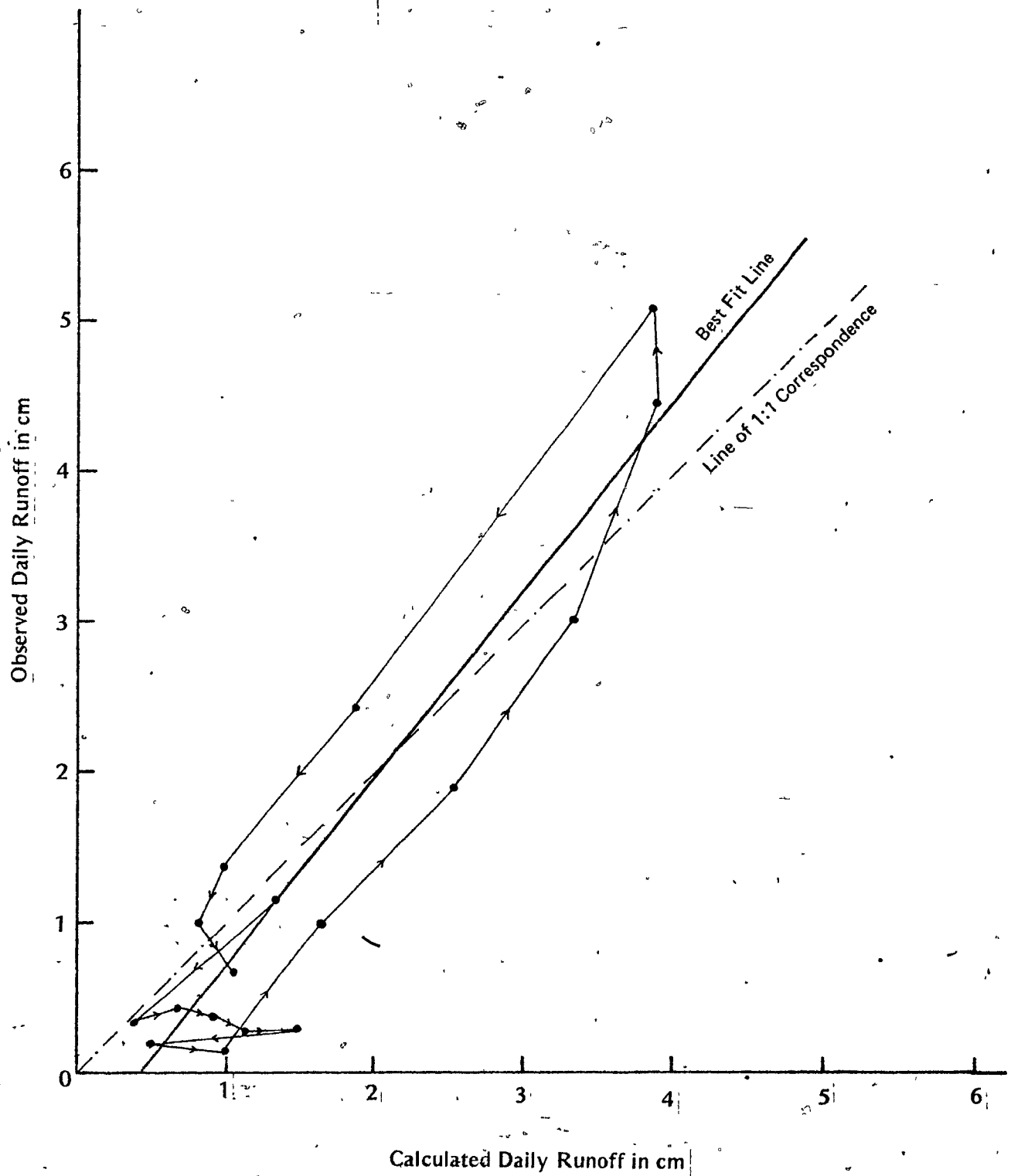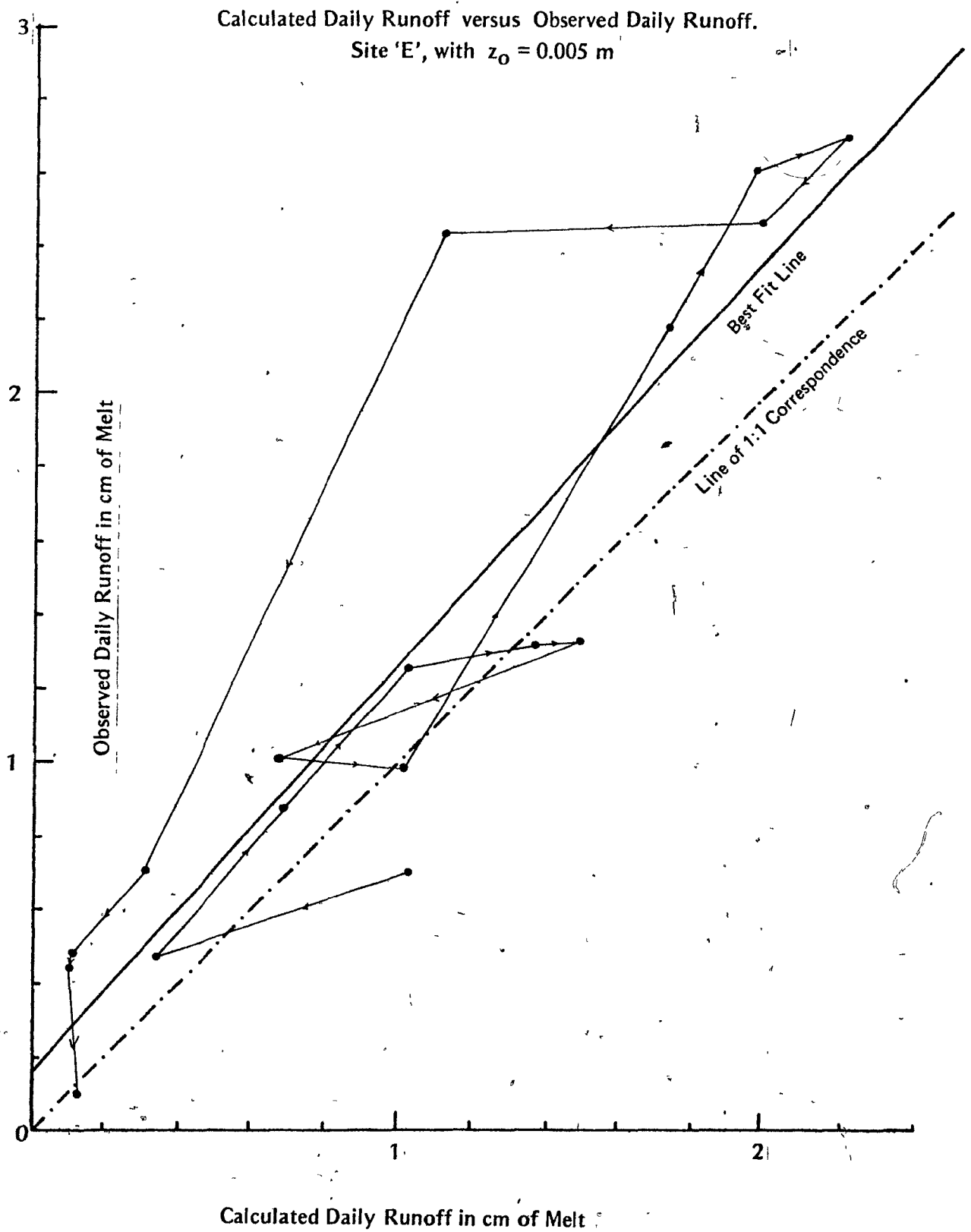Site 'E', with $z_o = 0.005$ m

Calculated Daily Runoff versus Observed Daily Runoff
Site 'F', with $z_0 = 0.005$ m

FIGURE 7.12

FIGURE 7.13
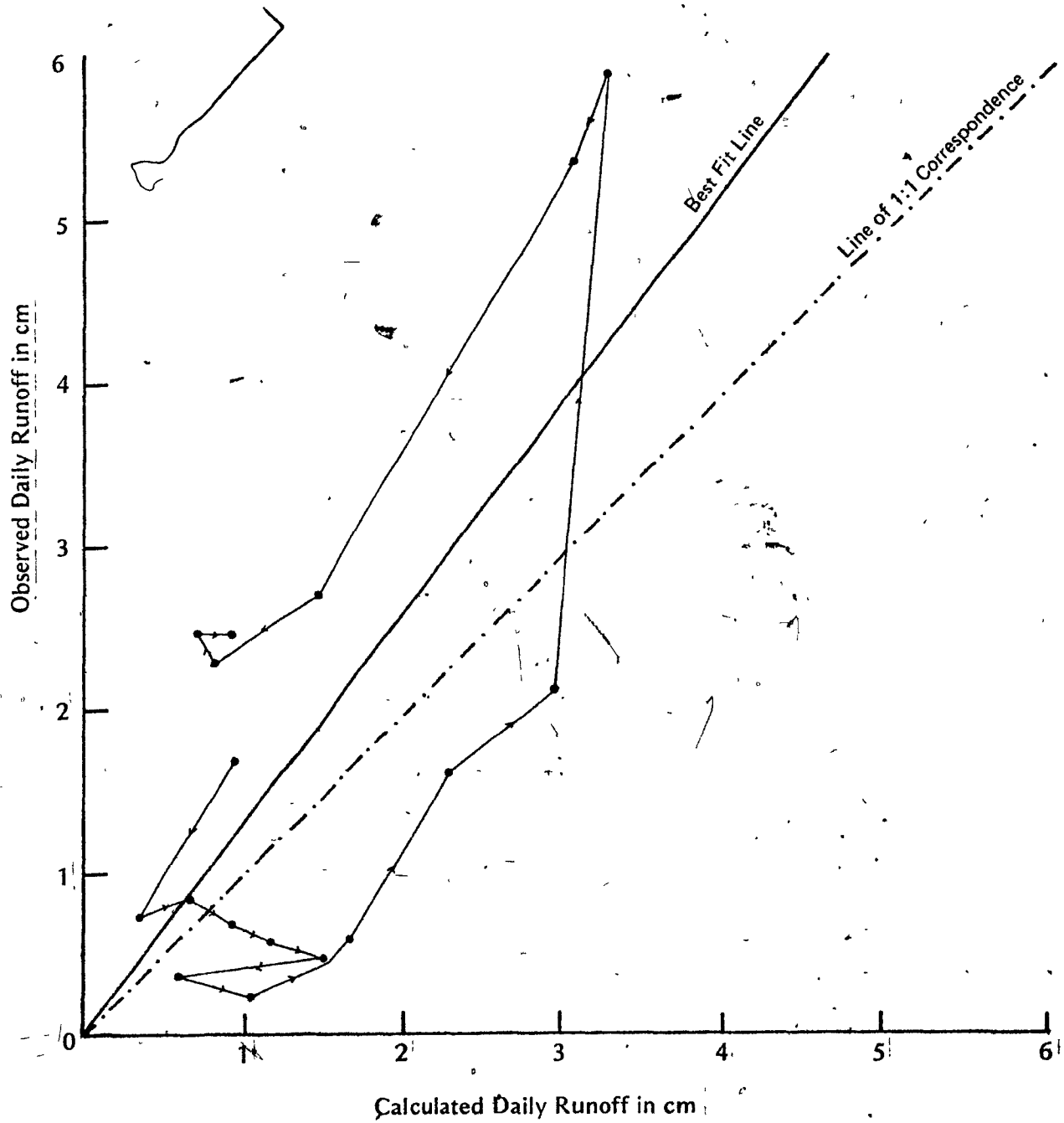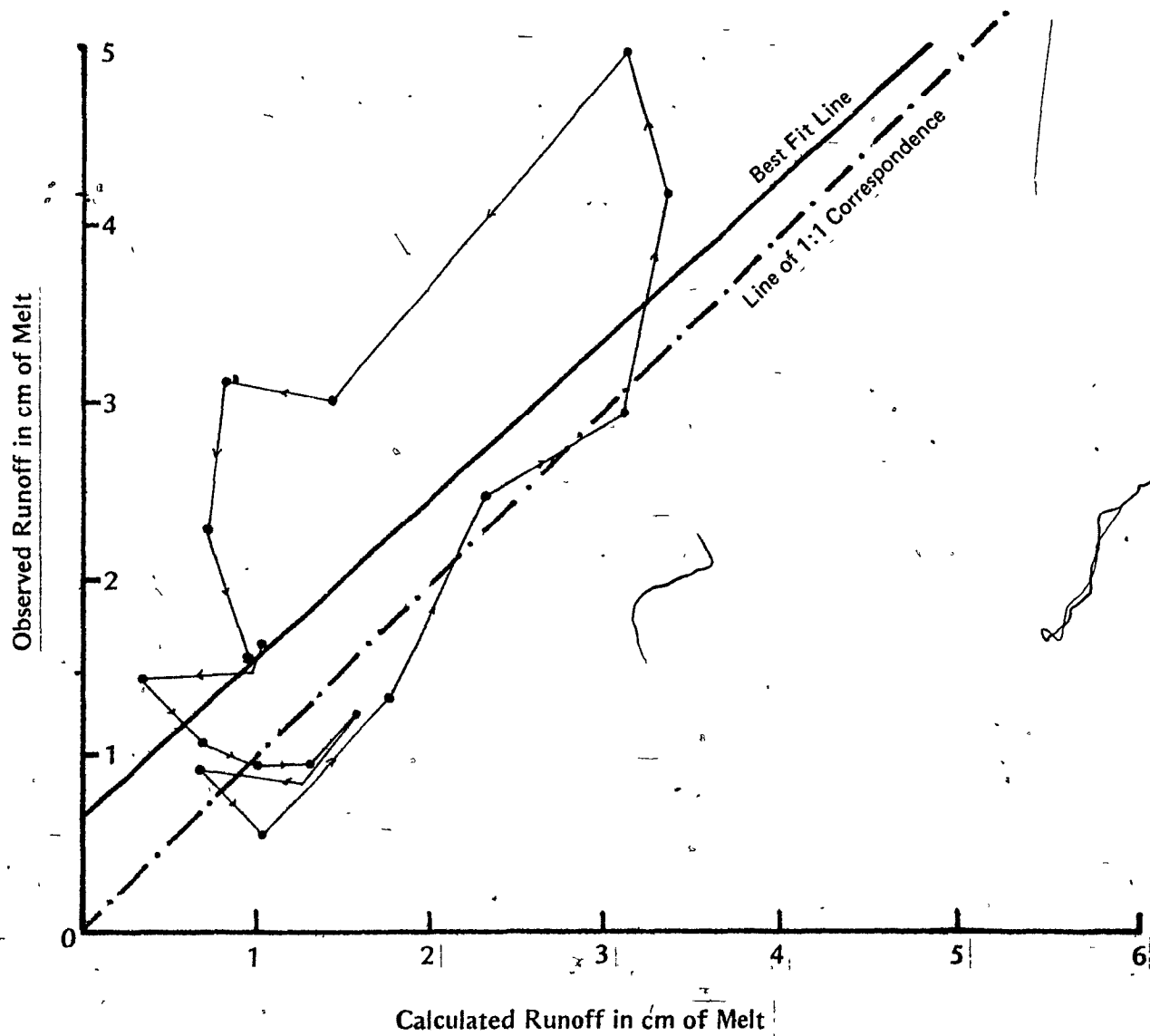
Calculated Daily Runoff versus Observed Daily Runoff
Site 'G' with $z_0 = 0.005$ m

Observed Runoff in cm of Melt (y-axis)

Calculated Runoff in cm of Melt (x-axis)

Best Fit Line

Line of 1:1 Correspondence

the peak. Hydrographs for the earlier period did not exhibit this extended recession. On site 'F', the form of the hydrographs changed between the 9th and 10th of May. On the 9th, as on preceding days, the recession limb was steep and extended about 24 hours after peak. On the 10th and 11th of May, the slope of the recession limb decreased so that on the 11th, the recession extended for 60 hours. This change seemed to be related to the continuation of melting throughout the night of the 10th and 11th. The relationship between the energy input to the snowpack and the extended recession limbs is not clear. Figure 7.15 shows that there is no simple relationship between peak surface melting and the rate at which a hydrograph recedes. Figure 7.16, however, demonstrates that there is a quite definite relationship between the peak observed runoff rate, and the rate of recession of the hydrograph, such that the recession rate varies greatly depending on the peak rate of flow. The relationship implies low recession rates for hydrographs with high peak flows. The computed recession for 'D' on May 11th is shown in Figure 7.14. Since this recession is extrapolated for some 40 hours, it seems possible that it may be exaggerated. As a check on how realistic it is to extend a recession this far, the same hydrograph was computed from theoretical surface flux, using the routing model described in Chapter 4. The results of this are shown in Figure 7.17. It can be seen that although the volume and peak of the predicted hydrograph are not completely in accord with the observed hydrograph, the predicted recessions using both methods are very similar. This confirms the fact that left to drain and without further melt, a snowpack of 60 cm depth would still be producing water

FIGURE 7.14

Separated Hydrographs for Site 'D', May 11th and 12th, 1973
Separated limbs shown in broken lines.

11/05/73

12/05/73

Discharge in cm/hr

0.4
0.3
0.2
0.1
0

24   12   24   12   24   12   24   12

Time E.S.T.

-122-
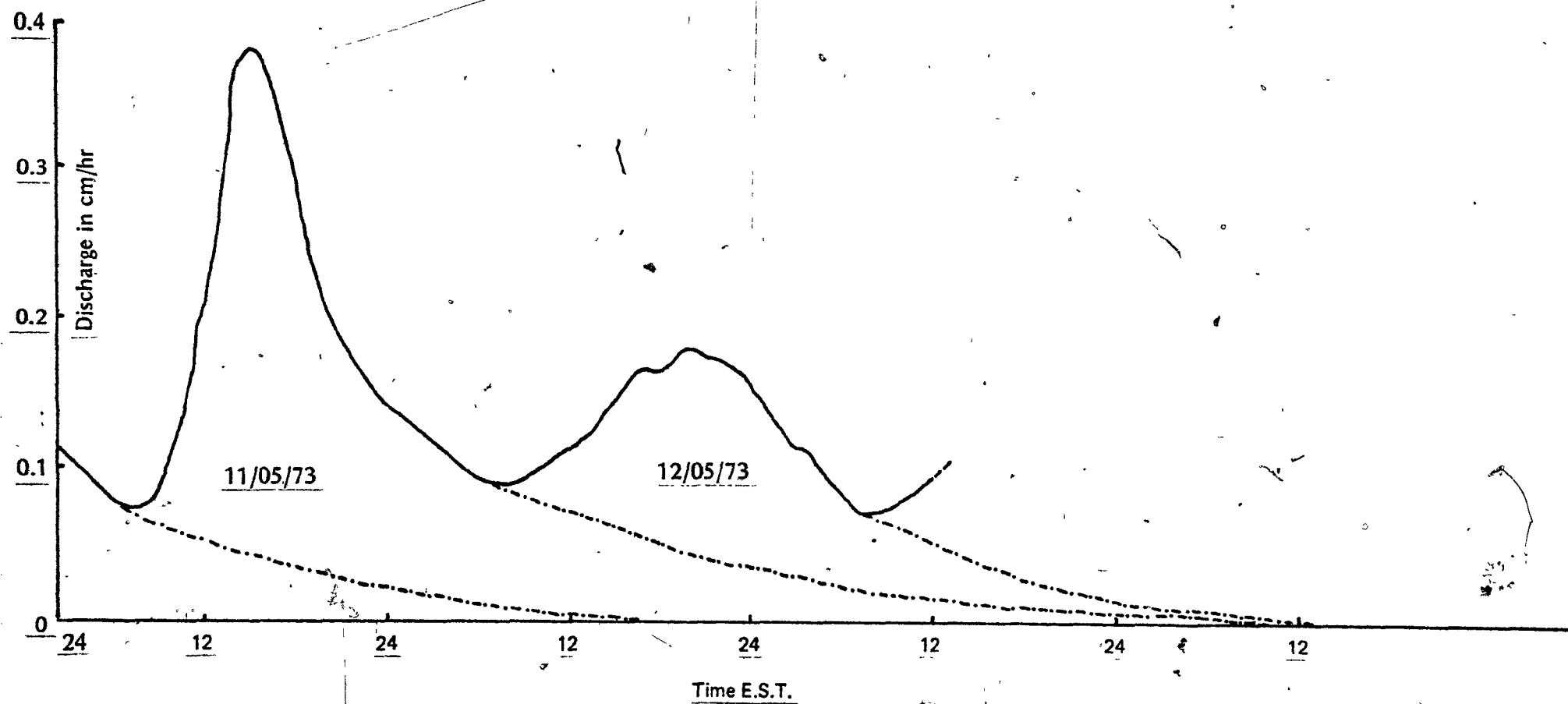
FIGURE 7.15

Gradient of Recession Limb versus Maximum Computed Surface Flux, Site 'F'.

Peak of Computed Surface Flux (cm/hr)

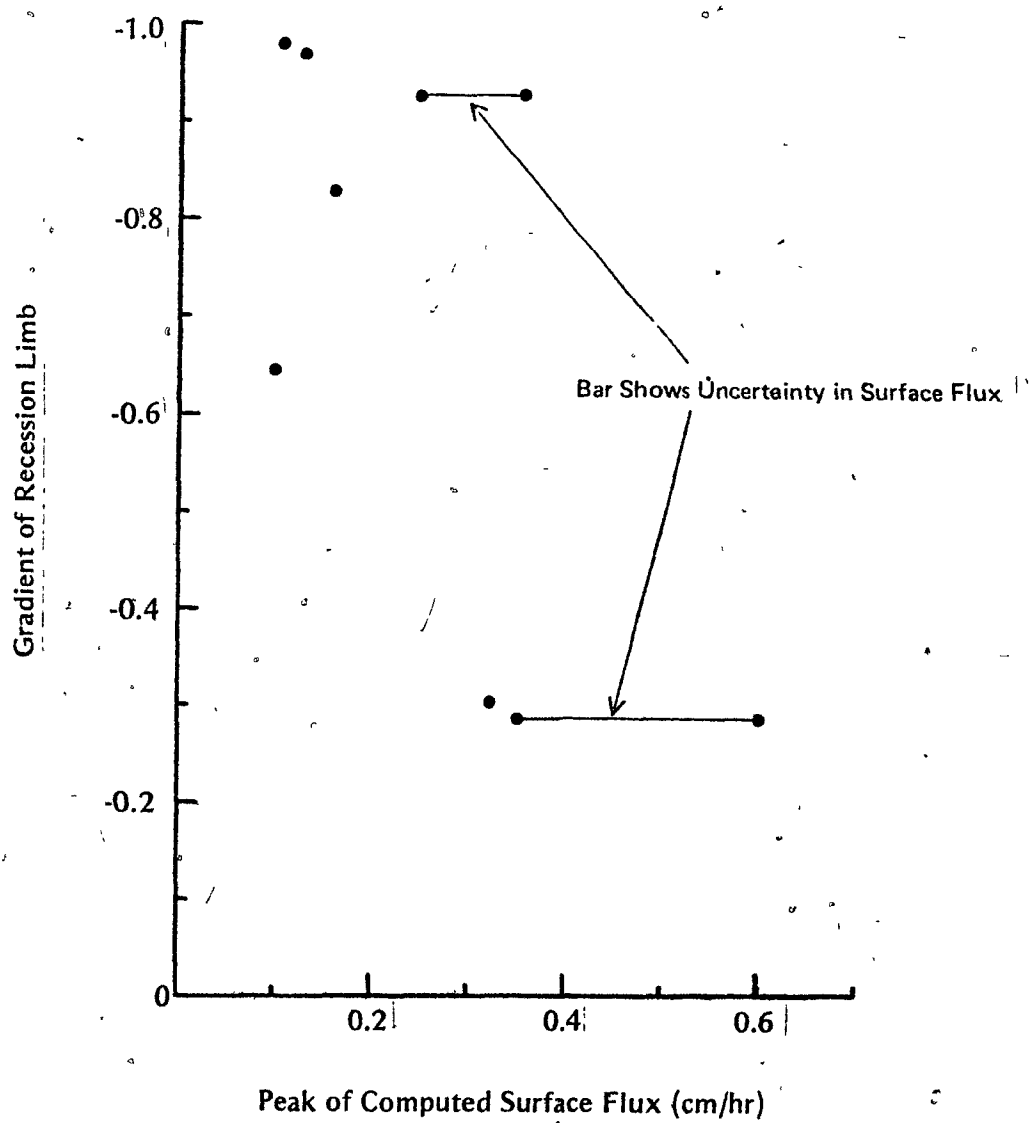FIGURE 7.16

Gradient of Recession Limb versus Measured Peak Runoff Rate, Site 'F'
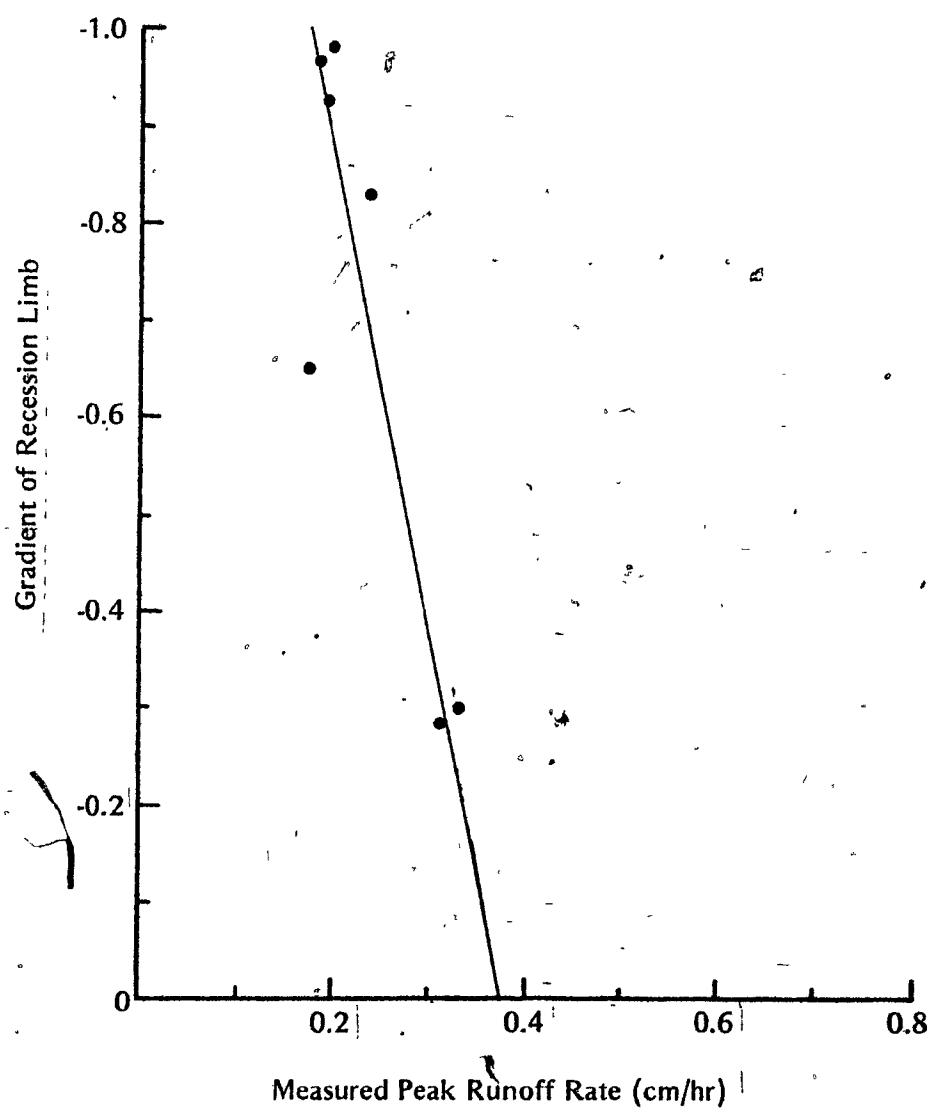
Hydrograph separation using two techniques. Site 'D',
May 11th, 1973

FIGURE 7.17

-125-

Hydrograph predicted using physical model.

Observed hydrograph separated
using normal technique.

Discharge in cm/hr

0.4

0.3

0.2

0.1

0

12   24   12   24   12   24   12   24

Time E.S.T.
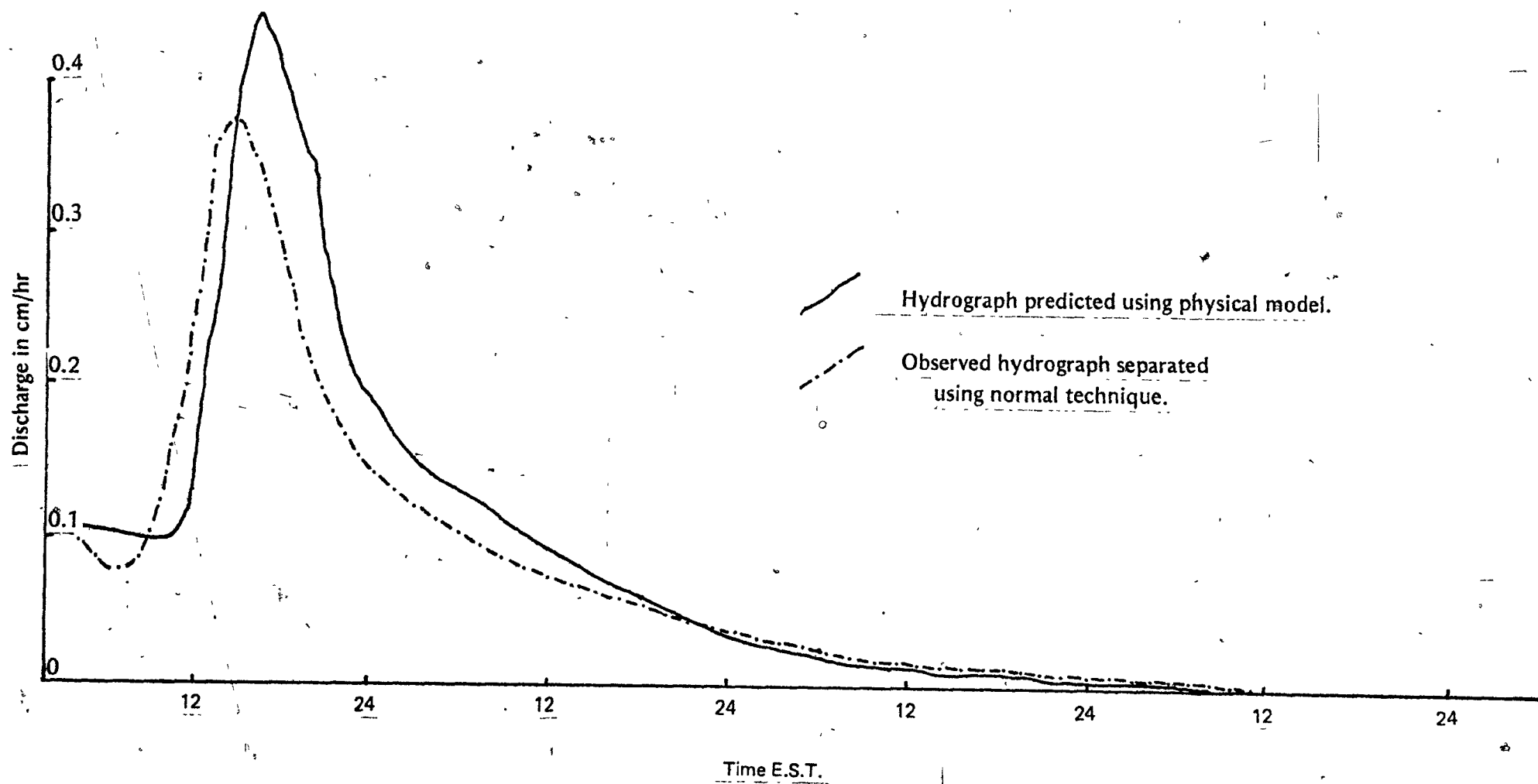
60 hours after a large peak. This means that to separate slope hydro-
graphs in order to define daily volumes of flow, the recession limb
is likely to be very long, and the chance of error in estimating daily
flows correspondingly high. Even small errors in extrapolating the
recession limb can lead to volume errors in the order of 0.5 cm. This
compares with standard errors of between 0.37 cm and 1.16 cm in the
regressions between observed and calculated melt. The observed slope
hydrographs for all sites are separated from May 10th onwards. Prior
to this date, melting ceased each night, and the similarity of re-
cession limbs made separation unnecessary.

The second possiblity in exploring the form of the hysteresis loop
is that the predicted daily flow from the energy balance is at fault.
The possible sources of error are:

(i) The estimate of H_R, radiation heatflow

(ii) The estimation of sensible heatflow

(iii) The estimation of latent heatflow.

In order to isolate the source of error, each component of the energy
balance was plotted against the daily error. Error showed no relationship
with H_R, and little with the sensible heatflow (see Figure 7.18) but a
suggestive association with the latent heatflow. Further, the relation-
ship between mean daily vapour pressure and error (Figure 7.19) seemed
the strongest of all. Vapour pressure affects latent heat transfer
directly, since it is one of the variables used in assessing H_e. It also
affects the radiation balance, in that sky emission is known to be a

FIGURE 7.18

Daily Error versus Daily Sensible Heatflow

Daily Error versus Daily Latent Heatflow
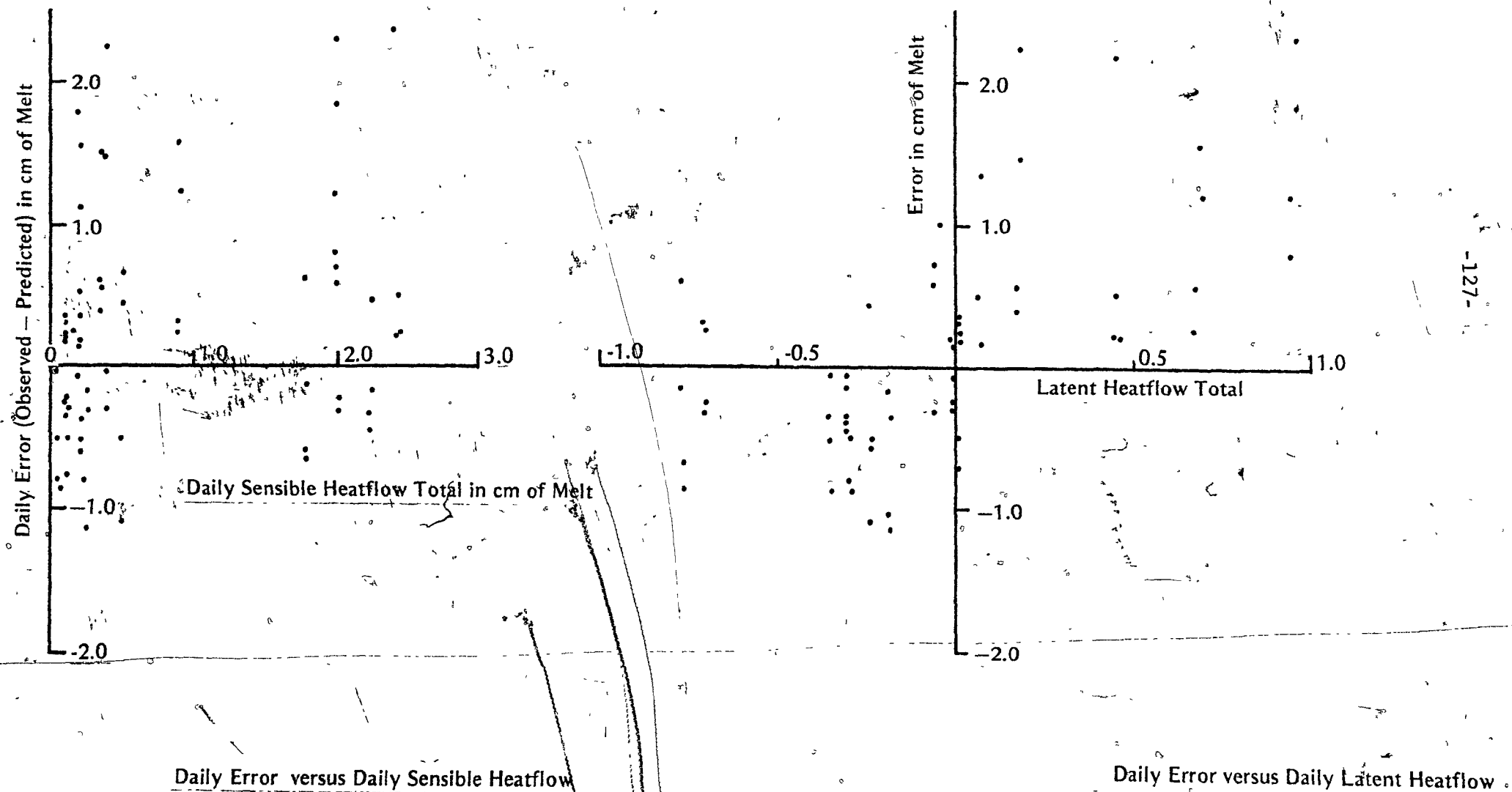
FIGURE 7.19

Mean Daily Vapour Pressure vs. Daily Error in cm of melt For all Forest Sites.
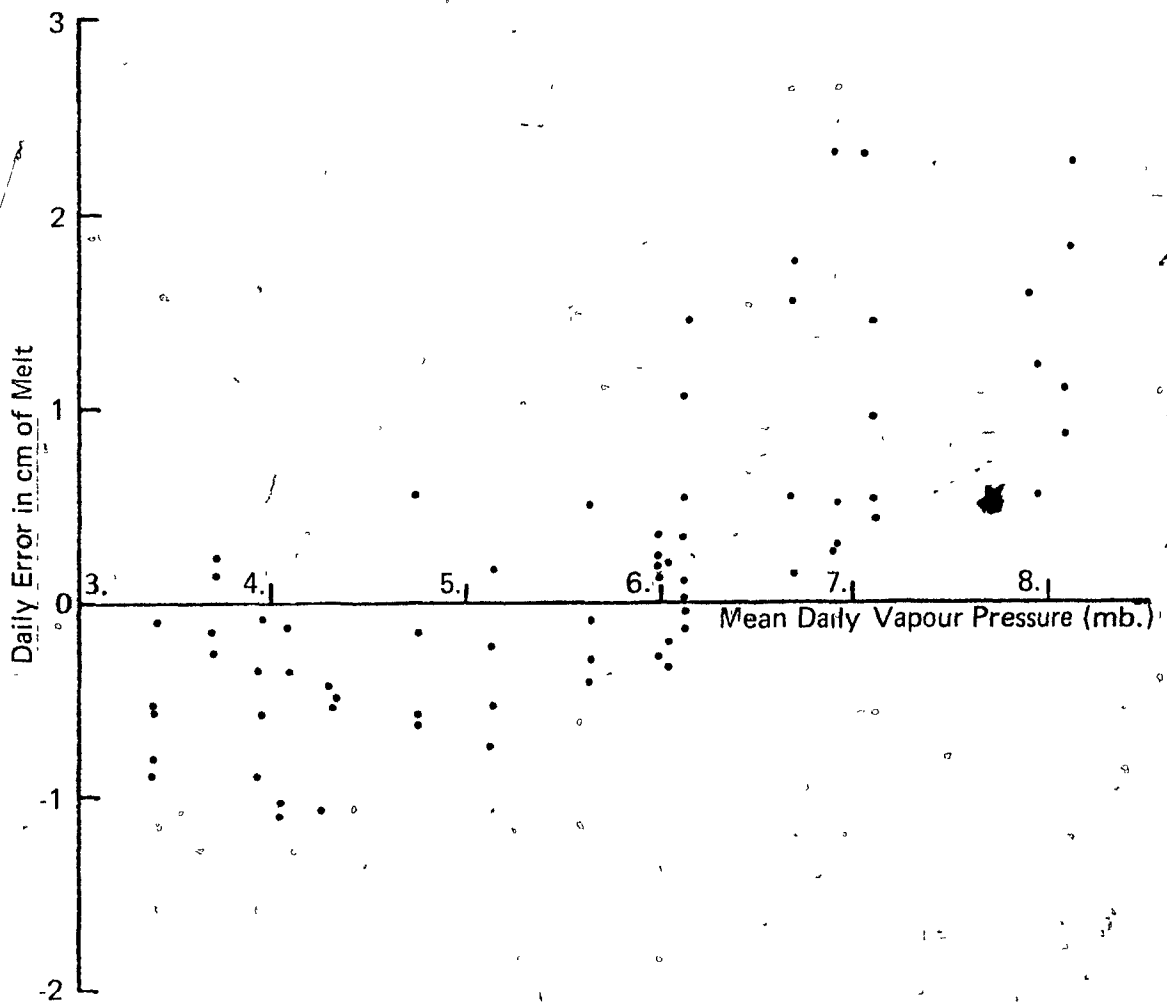
function of temperature and vapour pressure. The Brunt Equation (Sellers)
1965) gives an estimate of the variation of sky emission with tempera-
ture and vapour pressure .

$$L\downarrow = T_{abs}^4 \cdot (0.605 + 0.48\sqrt{ea}) \qquad\qquad 7.13$$

$L\downarrow$ = sky emission $(cal/cm^2/hr)$

T_{abs} = air temperature $(^{\circ}K)$

σ' = Stefan-Boltzmann constant $(cal/cm^2/hr/^{\circ}K^4)$

e_a = air vapour pressure (mb)

One of the assumptions implicit in the adoption of regression lines
of H_R on (Q+q) was that the relationship is invariant in the period
being considered. The similar form of the 1972 and 1973 relationship
(Equations 7.4 and 7.5), and the lack of any statistical difference
between them suggests that the assumption is valid. Similar regressions
undertaken in the Danville Vt. area (Dunne, pers, comm.) show that the
slope of H_R versus (Q+q) lines can vary daily during the melt, both
with air temperature, and to some extent with vapour pressure. If
we assume that the relationship does change, and that changes are due
only to variations in vapour pressure and its effects on $L\downarrow$, the
following results emerge. The mean daily vapour pressure at the outset
of the melt season was 4.5 mb, and at the close was 8 mb. Assuming
a temperature of $10^{\circ}C$, this change in vapour pressure would have changed
sky emission from an initial value of 23.2 $cal/cm^2/hr$ to a final value
of 25.2 $cal/cm^2/hr$. This difference would, at maximum, account for 0.6 cm
of melt per day, when the errors in question are over 2.0 cm. Thus

although errors in H_R may explain some of the problem, they cannot explain all of it.

Another possibility is that the measured value of e_a was erroneous, and affected the estimate of H_e, since from Equation 3.24

$$H_c = -C_1 (e_a - e_s) \cdot u_z \qquad cal/cm^2/hr$$

at maximum, the errror was approximately 2.0 cm per day. The value of H_c on the days with large errors was in the same order - that is between 1.7 and 2.0 cm/day. If the error is to be attributed to a poor measurement of e_a this suggests that for the large error days, H_e was an underestimate by about 2.0 cm of melt, and would have to be doubled, implying a mis-measurement in e_a of 2.0 mb, an implausibly large amount. In addition, parallel records of e_a were made using the hand-held Assman aspirated psychrometer, and a Lambrecht hygrothermograph in the Stevenson Screen. The regression equation of Assman-measured relative humidity on Lambrecht relative humidity was:

$$RH_a = 5.04 + 1.00 \, RH_L \qquad\qquad 7.14$$

where

RH_a = Assman relative humidity (computed from aspirated psychrometer readings)

RH_L = Lambrecht relative humidity (computed from thermohygrograph readings)

r = 0.90

r^2 = 0.81

σ_e = 8.07 %

N = 152

This is a very precise relationship. A similarly precise relationship exists for temperature, measured by the two methods, such that

$$T_{aA} = -0.005 + 0.997 \ T_{aL} \qquad\qquad 7.15$$

where

T_{aA} = Assman - derived temperature

T_{aL} = Lambrecht - derived temperature

r = 0.974

r^2 = 0.949

σ_e = 0.96 $^\circ$C

N = 152

These results show that a mis-measurement of air temperature or vapour pressure is unlikely, since the psychrometer and hygrothermograph readings are independent. It seems from these considerations that the errors cannot be attributed to either H_e or H_R directly.

A further suggestion is that the effective roughness length (z_o) increased in the later stages of the melt. Although no detailed observation was made of changes in the snow surface, it is known that the underbrush on all sites started to break through the snow surface on about May 10th. These alder bushes are compressed down to the ground by accumulating snow, and recover by springing back up to their vertical position after the snow has melted off them. At the early stages of their exposure, they extend approximately 10-15 cm above the snow surface, and constitute a new roughness element over the snowpack. If their height is taken as 15 cm, it can be assumed (Tajchman, 1971) that the

new roughness length is equivalent to one-tenth of the plant height,

giving $z_o = .015$ m. This increases the roughness length from .005 m

for the snowpack, increasing exchanges by approximately 1.5 times.

Roughness was changed on the 10th for all sites except 'E' which was

changed a day earlier. Figures 7.21 to 7.24 shows the effects on the

hysteresis of changing the roughness length. Figure 7.20 shows the

overall prediction for all 4 sites.

Site 'D'

$$Y = -0.38 + 0.96X \qquad\qquad 7.16$$

$r = 0.97$

$r^2 = 0.94$

$\sigma_e = 0.36$ cm

$N = 17$

The regression constant (a) differs significantly from zero at

the 5% level, but the regression coefficient (b) does not differ

significantly from 1.0 again at the 5% level.

Site 'E'

$$Y = -0.14 + 1.13X \qquad\qquad 7.17$$

$r = 0.93$

$r^2 = 0.87$

$\sigma_e = 0.31$ cm

$N = 17$

The regression constant does not differ significantly from zero,

the regression coefficient does not differ significantly from 1.0, both

at the 5% level.

FIGURE 7.20

Calculated Daily Runoff versus Observed Daily Runoff.

All Sites, with $z_0 = 0.005$ m from 29/04/73 to 09/05/73
and $z_0 = 0.015$ m from 10/05/73 to 15/05/73
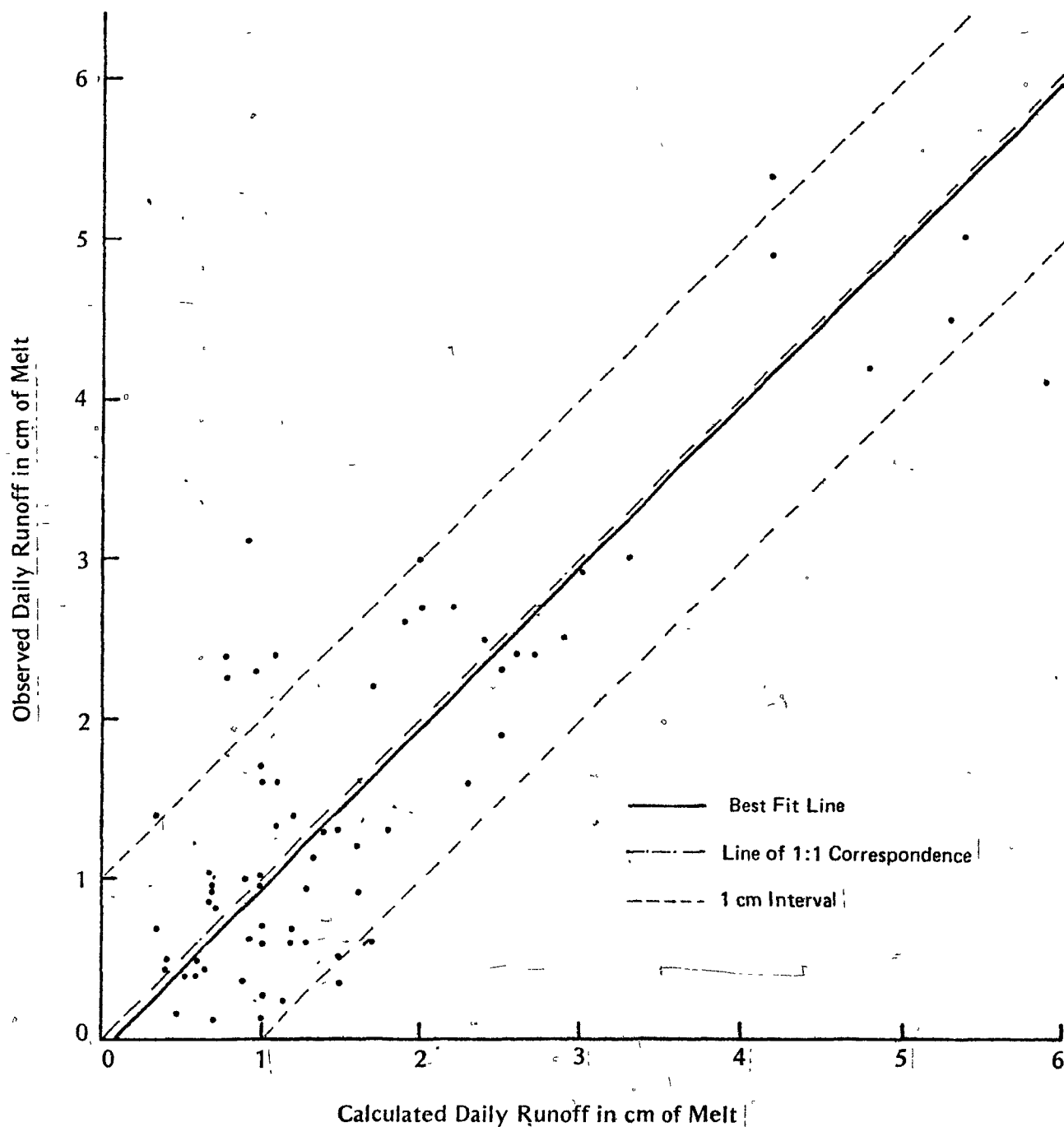
FIGURE 7.21

Calculated Daily Runoff versus Observed Daily Runoff.
Site 'D', with $z_0 = 0.005$ from 29/04/73 to 09/05/73
$z_0 = 0.015$ from 10/05/73 to 15/05/73
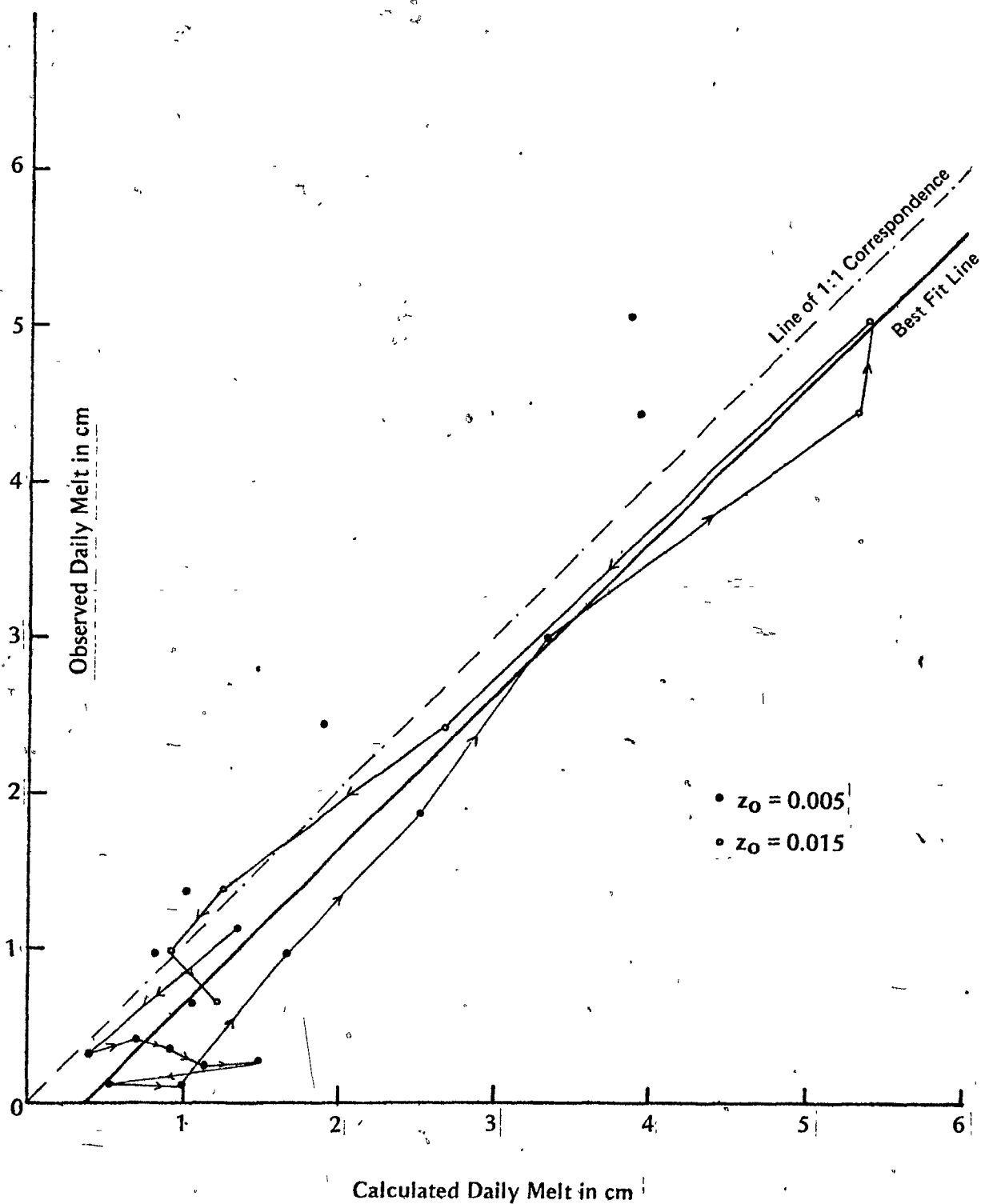
FIGURE 7.22

Calculated Daily Runoff versus Observed Daily Runoff.

Best Fit Line

Line of 1:1 Correspondence

• $z_0 = 0.005$
○ $z_0 = 0.015$

Observed Daily Runoff in cm

Calculated Daily Runoff in cm
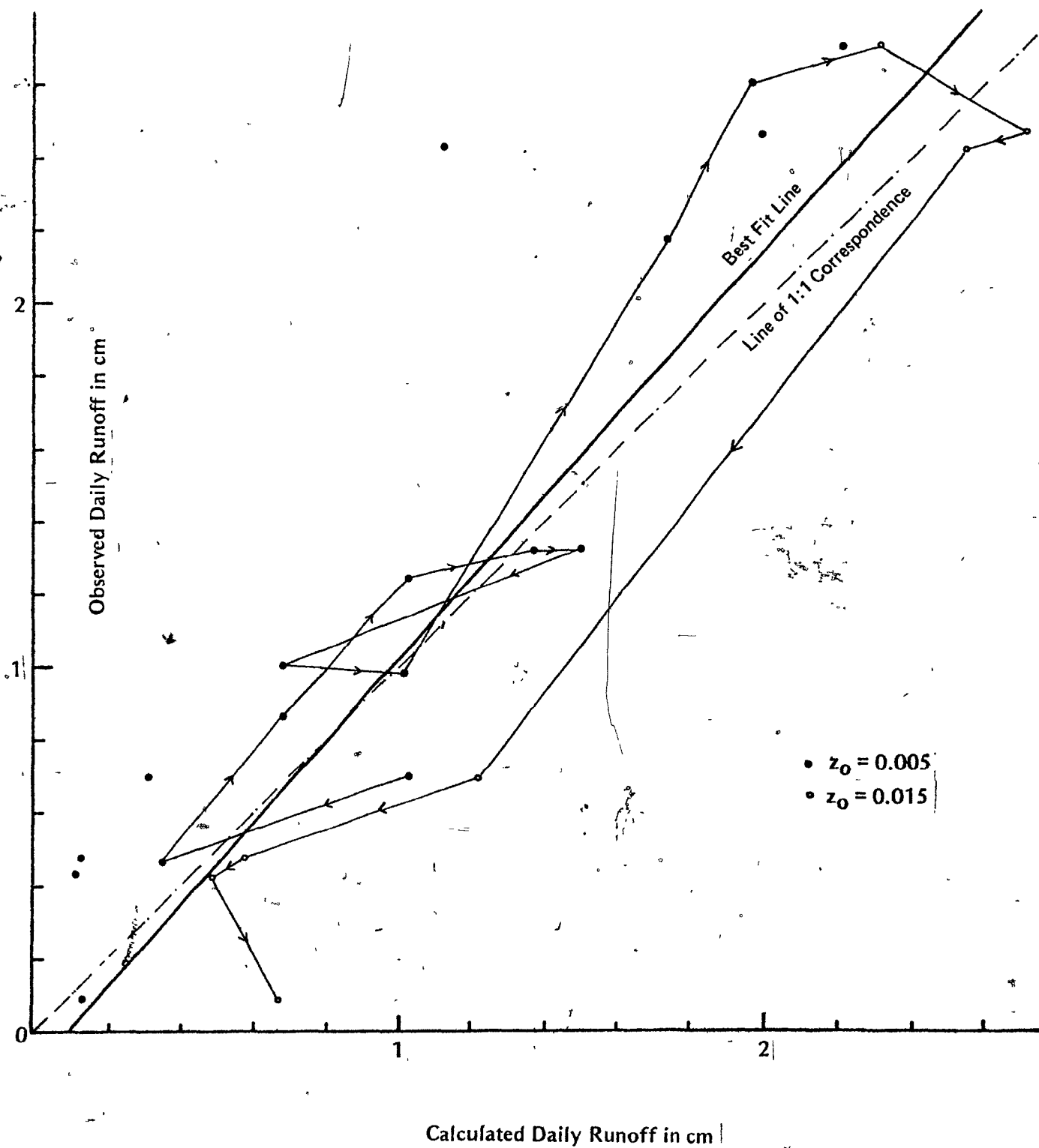
FIGURE 7.23

Predicted Daily Runoff versus Observed Daily Runoff
Site 'F', with $z_0 \doteq 0.005$ from 29/04/73 to 09/05/73
$z_0 = 0.015$ from 10/05/73 to 15/05/73

Calculated Daily Runoff in cm of Melt
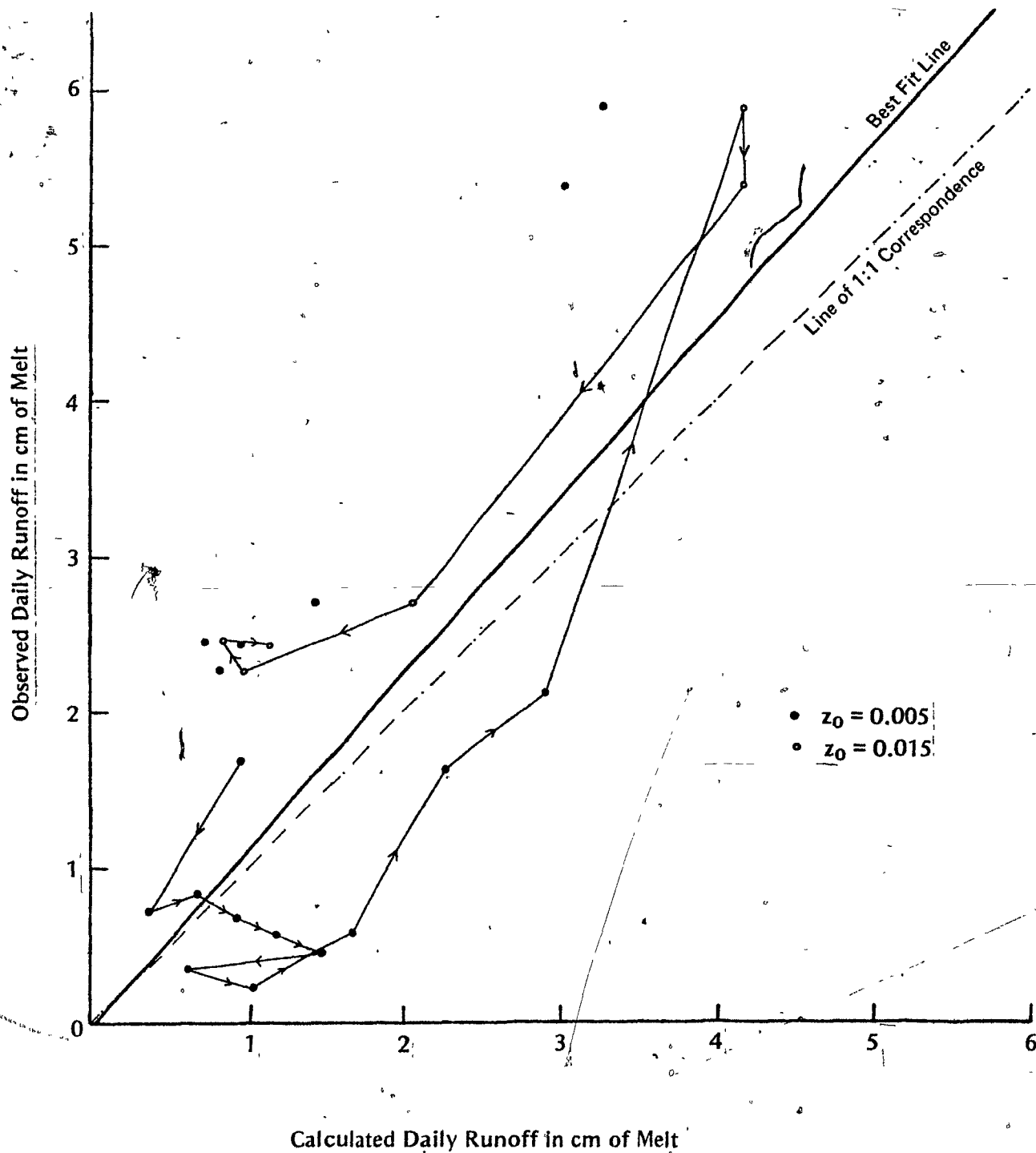
FIGURE 7.24

Calculated Daily Runoff versus Observed Daily Runoff Site 'G'.

$z_O = 0.005$ from 29/04/73 to 09/05/73

$z_O = 0.015$ from 10/05/73 to 15/05/73
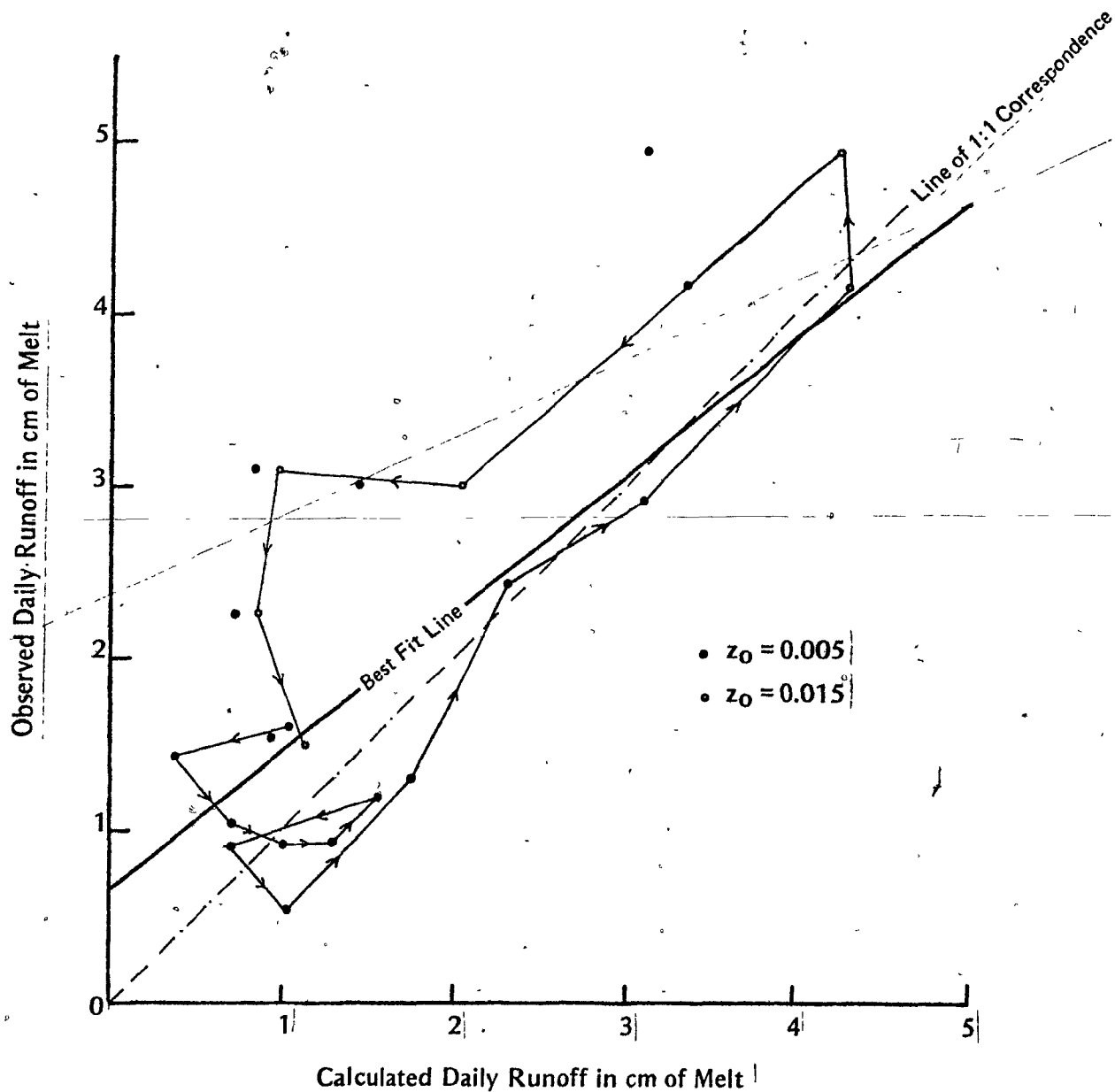
Site 'F'

$$Y = -0.07 + 1.19X \qquad\qquad 7.18$$

r = 0.83

r^2 = 0.69

σ_e = 0.93 cm

N = 17

The regression constant does not differ significantly from zero, and the regression coefficient does not differ significantly from 1.0, both at the 5% level.

Site 'G'

$$Y = 0.65 + 0.80X \qquad\qquad 7.19$$

r = .81

r^2 = .66

σ_e = 0.73 cm

N = 17

The constant ('a') differs significantly from zero at the   level, but the coefficient (b) does not differ significantly from 1.0 at the 5% level.

Taking the example of site 'D' (Figure 7.21), it can be seen that on days where previously values were underestimated (May 10th, 11th, 12th), the energy balance now overpredicts for May 10th, 11th, and 12th. On site 'E', 'F' and 'G', the patterns vary, but in all cases, correspondence between observed and computed melt is much improved. Figure (7.20) shows the overall prediction for all forest sites. This diagram, when compared

with Figure 7.9 shows a quite distinct improvement, with the best fit line almost coincident with the 1:1 line, and a lower standard error of the estimate.

The estimate of $z_o = 0.015$ m is only an approximation, and was adopted simply to demonstrate that a roughening of the snow surface substantially reduces the hysteresis on all sites. The adoption of two roughness lengths for the period before and after the first emergence of vegetation is clearly unrealistic. The roughness of the surface does not change in this fashion, but would increase from a value of approximately .005 m early in the season in response to the baring of patches of ground and to the emergence of bushes. The figure of .015 m was chosen because it is the best estimate that can be made with available data. The use of this figure in re-estimating the energy balance estimate shows that the change in z_o is probably a major contributor to the bad estimation late in the season.

Some of the plots still show a loop similar to the original, but not as wide. This persistent underestimation late in the season can probably be attributed to the effects of bare patches of ground and vegetation on the radiation balance near the ground. A commonly seen phenomenon on a snow surface is the "melt-cups" around trees, snowstakes and protruding vegetation. This localized melting is caused largely by radiation being absorbed by the objects protecting through the snowpack, which then re-radiate causing intensified melt in the immediate vicinity. This intensification of radiation melt is not accounted for by the regression model used to estimate radiation in the present study, since the net radiometers were always placed over an unbroken snow surface.

From the foregoing discussion, it can be seen that although the predictions of daily melt using the heatflow model are good, there are uncertainties in some areas. The first affects the turbulent exchanges, and is the lack of data collected on surface roughness changes. This lack emphasizes the importance of measuring the factors influencing the turbulent exchanges, in particular changing surface roughness. The second uncertainty is the lack of knowledge of how the H_R versus $(Q+q)$ regression lines might change with temperature, vapour pressure, and with differing surface conditions due to the penetration of plants. Finally, the exact value of the observed daily runoff is difficult to fix accurately. There is some uncertainty involved because of the extremely protracted recessions suggested by two independent methods of analysis.

CHAPTER 8

APPLICATION OF THE THEORY OF SNOWMELT RUNOFF

Equation 4.18 describes the velocity with which a parcel of water of constant flux (v_w) percolates vertically downwards in a snowpack.

With a constant v_w, Equation 4.18 reduces to

$$\left(\frac{dz}{dt}\right)_{v_w} = C'$$

where

$$C' = \frac{n}{\emptyset_e} \left[\frac{\rho_w \cdot g \cdot k'}{\mu} \right]^{1/n} v_w^{\left(\frac{n-1}{n}\right)}$$

or we may write

$$\int dz = C' \int dt$$

$$z = C't + C''$$

at $t = 0$, $z = 0$, and so $C'' = 0$

where

$t = 0$ represents the time at which the flux v_w leaves the surface

so

$$z = \frac{n}{\emptyset_e} \left[\frac{\rho_w \cdot g \cdot k'}{\mu} \right]^{1/n} v_w^{\frac{(n-1)}{n}} \cdot t \qquad 8.1$$

This equation describes the depth of penetration of a parcel of constant volume flux (v_w) at any time t. Field evidence given by Colbeck and Davidson (1972) suggests that n = 3 for snow.

Thus Equation 8.1 reduces to

$$\frac{z}{t} = \frac{3}{\emptyset_e} \left[\frac{\rho_w \cdot g \cdot k'}{\mu} \right]^{1/3} \cdot v_w^{2/3} \qquad 8.2$$

The flux plates described in Chapter 5 were installed in order to get an estimate of permeability for the unsaturated layer (k'). From Equation 8.2, we know that time of travel is related to snow depth, flux rate, and snow permeability and porosity. For a constant flux rate, depth and porosity, t is a function of permeability alone. Suppose we take the falling limb of the wave of surface melt, and identify the departure time of various flux levels (see Figure 8.1), and then from the flux-plate data derive their time of arrival after traversing the depth of snow over the flux plate. From Equation 8.2

$$\log(\frac{z}{t}) = \log \left[3 \left[\frac{\rho_w \cdot g \cdot k'}{\mu} \right]^{1/3} \emptyset_e^{-1} \right] + 2/3 \log v_w \qquad 8.3$$

If we now plot $\log(\frac{z}{t})$ against $\log(v_w)$ we obtain a linear relationship. The slope of the line is 2/3, and the intercept on the ordinate of this graph at an obcissa value of $\log v_w = 0 (v_w = 1)$ gives the value of the expression $3 \frac{\rho_w \cdot g \cdot k'}{\mu}^{1/3} \emptyset_e^{-1}$. As detailed later in this section, we can compute $\emptyset_e$, $\frac{\rho_w \cdot g}{\mu}$ is known, and thus substituting in the intercept value, we will obtain a value for k'. Unfortunately, the flux plate data were too inconsistent to use. In many cases the meltwater wave apparently reached the flux plate before it left the surface. The causes of this failure are not obvious, but the flux plate in question was installed in a pit and it seems that

FIGURE 8.1

Application of the Flux Plate Data

Snow Surface

Flux Plate

Ground Surface

z

Surface Flux Trace

Surface Flux = 0.5 cm/hr

Flux Rate (cm/hr)

Flux Plate Trace

Surface Flux = 0.5 cm/hr

Flux Rate (cm/hr)

t1   t2
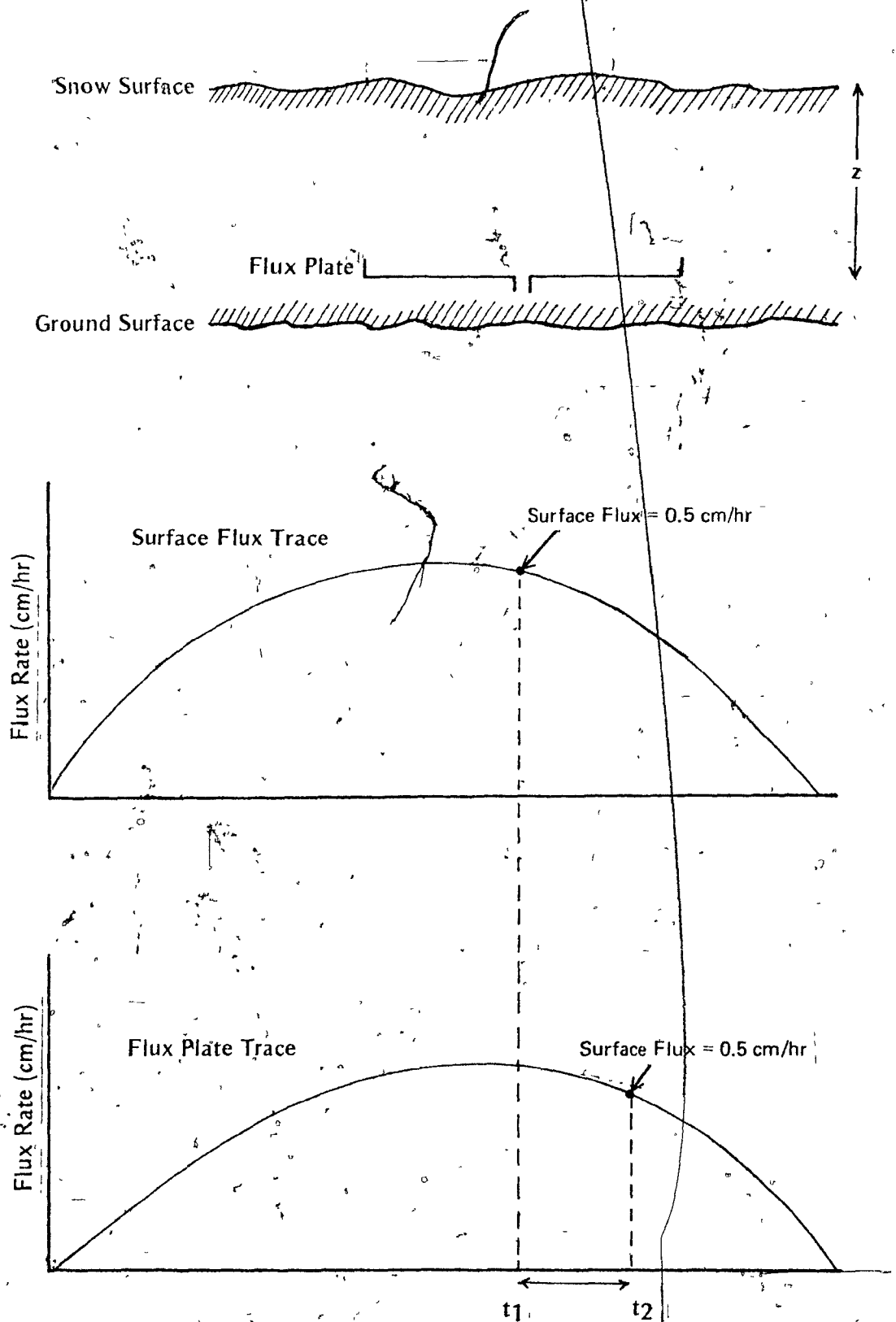
melting of the exposed face of the pit may have contributed water to
the flux plate. In addition, errors may have been caused by the under-
estimation of the surface flux. This would lead to a bad estimate of
departure times, and inconsistencies in the data. In the absence of a
measured value for permeability, a value had to be assumed from the
literature . There are many estimates of permeability available, but
few are applicable to the type of snow found during the thaw at
Schefferville. Three estimates of permeability are available for snow
with particle sizes like those in the unsaturated portion of the
Schefferville snowpacks. They are

$$k' = 5.0 \times 10^{-6} \text{ cm}^2 \quad \text{(Shimizu, 1970)}$$

$$k' = 17.9 \times 10^{-6} \text{ cm}^2 \quad \text{(Kuroiwa, 1968)}$$

$$k' = 45.0 \times 10^{-6} \text{ cm}^2 \quad \text{(Ishida and Shimizu, 1955)}$$

Of these the Shimizu (1970) estimate seems to apply best to the
Schefferville area, the snow in both areas having similar crystal
sizes. A consideration of these relative crystal sizes (see Table 8.1)
led to the adoption of an unsaturated layer permeability (k') of
$6.0 \times 10^{-6} \text{ cm}^2$. In order to make an estimate of the permeability of the
saturated layer (k_s) reference to the crystal sizes (Table 8.1) shows
that the crystal size in the saturated layer is approximately three
times that in the unsaturated layer.

It may be shown (Todd, 1959) by dimensional analysis that permeability
is proportional to the square of particle diameter, so that

$$k' = C_3 d_u^2$$

where C_3 = a constant

           d_u = mean crystal size in the unsaturated layer.

Table 8.1

Time Measured	Distance Downslope	Crystal Size in the Saturated Layer (mm)	Crystal Size in the Unsaturated Layer (mm)	Thickness Sat. Layer (mm)
08/05/73 'E' 1200 h	10	3-10	3-7	10
	20	1-3	2-7	8
	30	2-10	2-3	5-8
	40	3-10	5	3-10
08/05/73 1430 h	10	2-7	1-3	2-7
	20	3-7	0.5-2	15
	30	1-3	0.5-2	25
	40	3-7	7-3	27
08/05/73 1600 h	10	3-7	2-5	0
	20	0.5-2	1-4	7
	30	0.5-2	1-3	0
	40	1-3	1-3	15
09/05/73 1115 h	10	2-11	2-10	8
	20	1-5	1-3	0
	30	1-6	1-4	0
	40	1-9	2-4	0
09/05/73 1300 h	--	--	--	12
	--	--	--	20
	--	--	--	20
	--	--	--	20

Crystal Size and Saturated Layer Thicknesses

Similarly, in the saturated layer, we can write

$$k_s = C_3 d_s^2$$

where

d'_s = crystal diameter in the saturated layer

or

$$\frac{k_s}{k'} = \frac{d_s^2}{d_u^2} = \left(\frac{d_s}{d_u}\right)^2$$

or, since $d_s = 3 \times d_u$

$$k_s = .9 \times k'$$

using $k' = 6 \times 10^{-6}$ cm^2, this gives a value of $k_s = 54 \times 10^{-6}$ cm^2 for the permeability of the saturated layer.

Application of the model to a field case

In the case of site 'A' on the tundra on May 16th, 1972, we have (from measurement) the following parameters:

snow density (ρ_s) = 0.422 gm/cm^3

mean snow depth (z) = 100.9 cm

slope length (L_s) = 8530 cm

slope inclination(β) = 4.4°

Figure 8.2 shows the hourly computed surface melt in cm/hr for site 'A'. The total melt for the day was 3.55 cm. The "wave" of surface flux starts at 1100 EST, peaks at 1400 EST, and ceases at 0300 EST of the following day.

FIGURE 8.2

Calculated Surface Flux and Calculated Input to the Saturated Layer.
Site 'A', May 16th, 1972
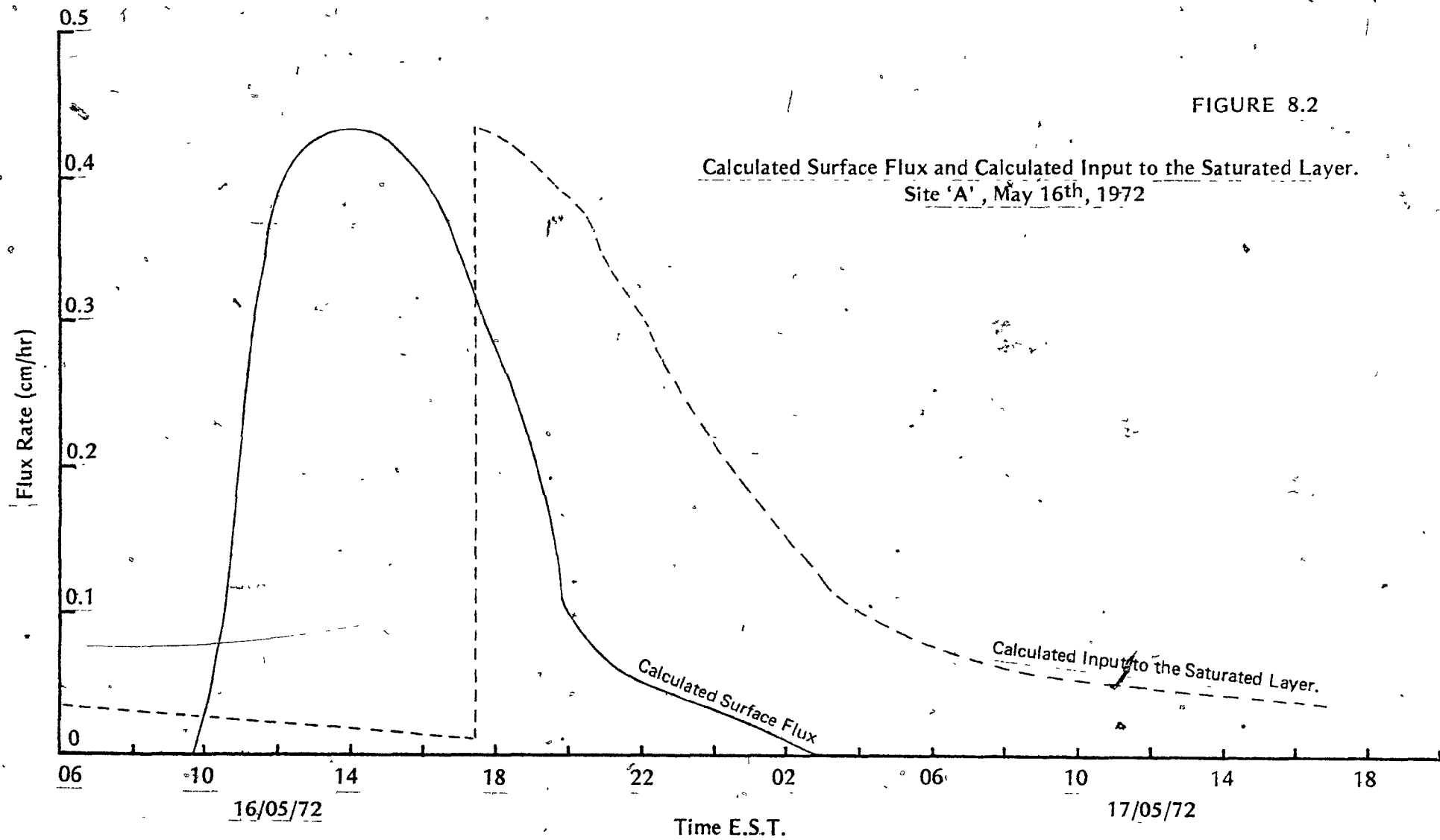
Equation 8.2 shows that for a constant flux v_w, the speed with which a parcel of water penetrates vertically into the snowpack can be determined if $\emptyset_e$ and k' are known. The previously mentioned estimate of $6.0 \times 10^{-6.}$ cm^2 was used for 'k' . To derive the effective porosity $\emptyset_e$, let us consider a unit volume of the snowpack containing only its irreducible water content (see Figure 8.3). Total mass in the unit is equivalent to the snow density (ρ_s)

$$\rho_s \times \text{ cm}^3 = \cdot 422 \times 1 \text{ gm}$$

or

$$0.422 \text{ gm} = \text{mass of water and mass of ice}$$

$$= \text{Swi} \cdot \emptyset \cdot \rho_w + (1 - \emptyset) \cdot \rho_i$$

where

ρ_s = snow density = 0.422 gm/cm^3

ρ_i = ice density = 0.917 gm/cm^3 (at 0°C)

ρ_w = water density = 1 gm/cm^3

Swi = irreducible saturation for snow

Swi was assumed to be 8% (Colbeck, pers. comm.)

Therefore

$$0.422 = 0.08 \emptyset = (1-\emptyset)(0.917)$$

or $\emptyset = 0.591$

and, since $\emptyset_e = (1-\text{Swi}) \cdot \emptyset$, $\emptyset_e = 0.544$.

We can now compute the rate with which the fluxes of water leaving the surface travel down into the snowpack. The term $\left[\dfrac{\rho_w \cdot g}{\mu}\right]$ reduces to a single constant, and Equation 8.2 gives the vertical velocity of a parcel of water with a given flux rate.

FIGURE 8.3

Water held at irreducible saturation (Pore space unavailable for flow).

Ice Crystals.

Scale

2 mm

Pore space available for flow.
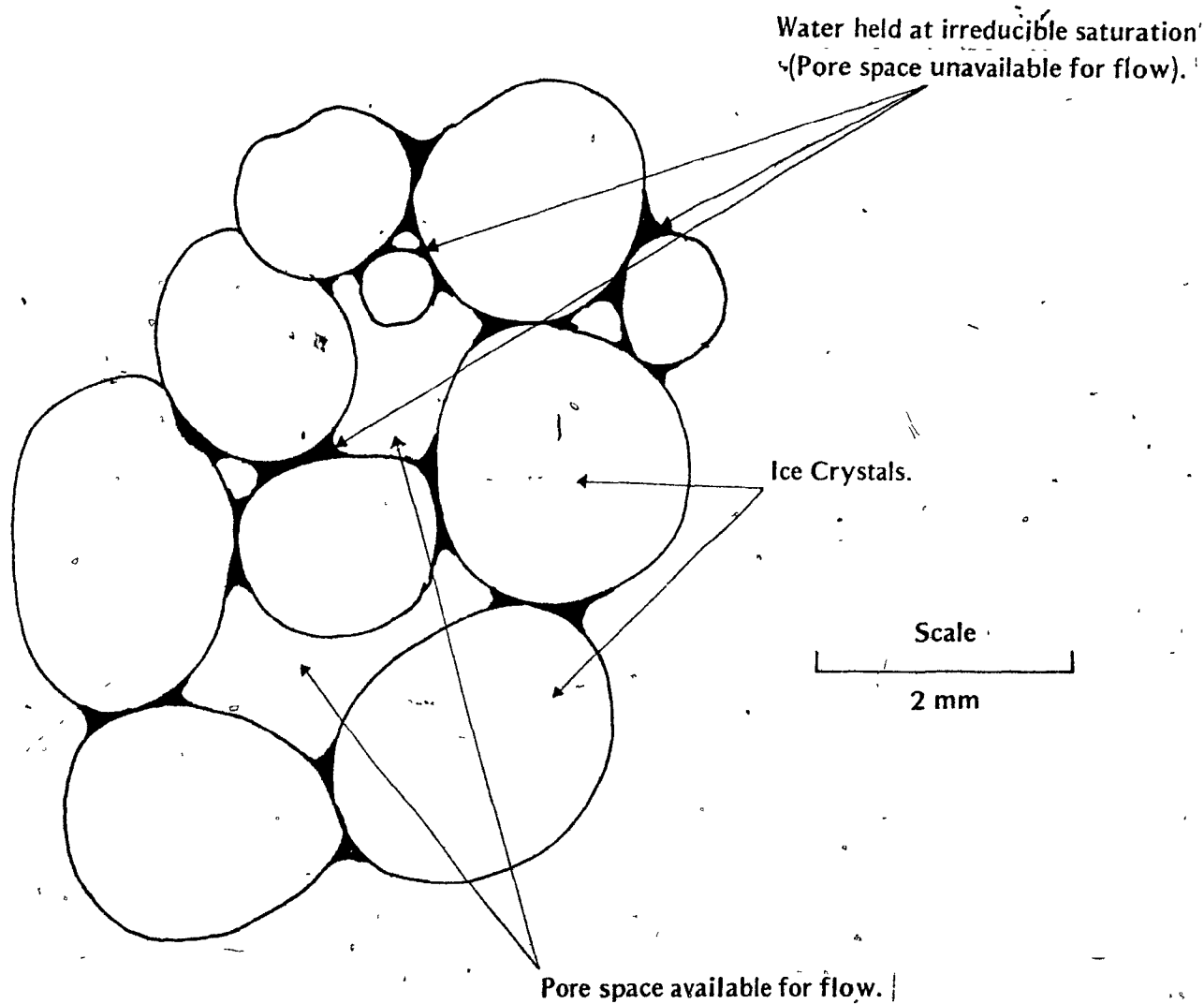
Section of Snowpack at Irreducible Saturation

Figure 8.2 shows the computed surface flux for May 16th 1972 for site 'A' on the tundra. Using this diagram, the departure times from the surface of various discrete levels of flux are derived. For example, from Figure 8.2, a flux of 0.025 cm/hr left the surface at 1006 EST, one of 0.05 cm/hr at 1015 EST, are of 0.100 cm/hr at 1021 EST, and so on. These departure times are derived for both the rising and falling limbs of the graphs of computed surface flux. The next step is to plot, for each flux level, the line describing the rate of vertical travel of the flux downwards from the surface.

In Figure 8.4, the horizontal axis is time, and the vertical axis is depth, with the snow surface at zero. We know the departure time of the first flux level (0.025 cm/hr), and its rate of vertical propagation, from Equation 8.2. Thus a line is drawn originating at $z = 0$ and time 1016 EST, with a slope such that after 1 hour, $z = 4.9$ cm (since $(dz/dt)_{v_w}$ for a 0.025 cm/hr flux is 4.9 cm/hr). This process is then repeated for the later flux levels, with differing times of origin and rates of travel. Since the velocity of vertical travel of a flux is related to its size (Equation 8.3), higher fluxes travel faster than lower ones. Thus the line representing the travel of the second flux ($v_w = 0.050$ cm/hr) will intersect the line describing the travel of the earlier flux ($v_w = 0.025$ cm/hr). This intersection gives rise to a "shock front", which is an instantaneous increase of flux with time. This shock front is caused by the over-riding of parcels of flux by succeeding parcels, and is analogous to a breaking sea wave. The rate of vertical propagation of the shock front is given (Colbeck, 1973) by,

FIGURE 8.4

0.125

0.100

0.050

0.025

--- z = 22 cm (Site 'C')

4   Time E.S.T.   06   12
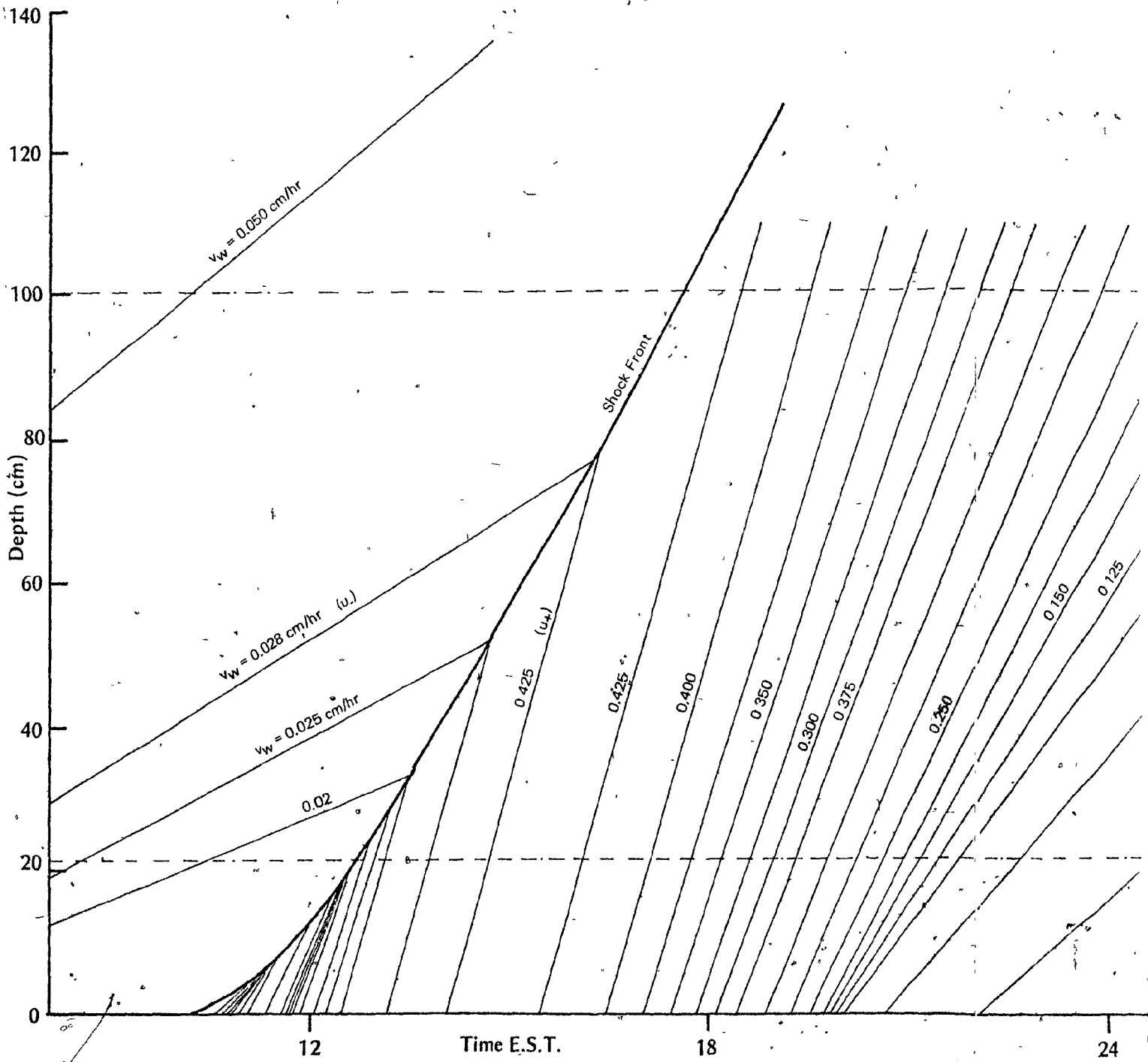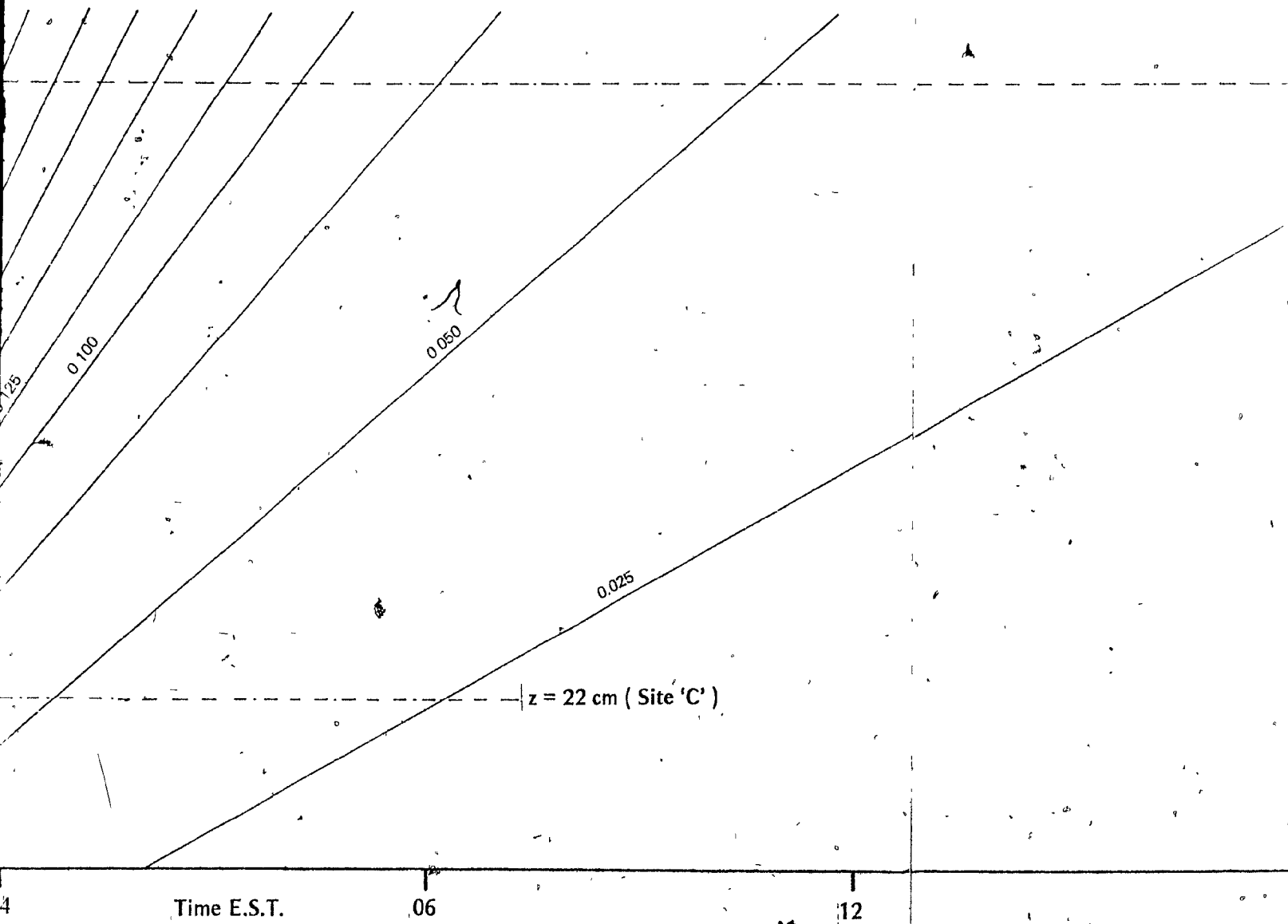
17/05/72

..racteristics $(dz/dt)_{u_w}$ and Shock Front $(d\xi/dt)$ for Site 'A' , May 16th, 1972

z = 100.9 cm (Site 'A')

'C')

12

17/05/72

)72

$$\frac{d\xi}{dt} = (\frac{\rho_w \cdot g \cdot k'}{\mu})^{1/3} \emptyset_e^{-1} (u_+^{2/3} + u_-^{1/3} \cdot u_+^{1/3} + u_-^{2/3}) \qquad 8.14$$

where

$\frac{d\xi}{dt}$ = rate of vertical propagation of the shock front   (cm/hr)

u_- = the lower flux level at the shock front   (cm/hr)

u_+ = the higher, later flux level at the shock front   (cm/hr)

The values of u_- and u_+ change continuously as the shock front moves downwards with time. At any time, u_+ is defined by a flux level from the current day's melting, and u_- by a flux level from the previous day. For example, in Figure 8.4, the rate of propagation of the shock front $(\frac{d\xi}{dt})$ at z = 101 cm is defined by u_- from the previous day of 0.028 cm/hr, and u_+ from the prsent day (v_w = 0.435 cm/hr). For each successive u_+ value defined where a flux intersects the shock front , there is a value of flux from the previous day which will pass through the intersection. This is u_-. For intersections of the shock front and new u_+ values where a previously plotted u_- does not pass through the point, a value of u_- is estimated from the graph. The process of constructing the shock front continues until the peak of melt is reached, in the case of site 'A' on May 16th, peak surface melt = 0.435 cm/hr. After the peak, the lines of slope $(dz/dt)_{v_w}$ describing the passage of parcels of flux down through the snowpack start to diverge, since later fluxes are lower, and therefore slower. Thus no shock front is generated . The end product of this process is shown in Figure 8.4.

To derive the variation of flux with time at any depth z, a horizontal line is drawn at the depth with which we are concerned. In the present example, for site 'A' on May 16th 1972, the snow depth was 100.9 cm. Thus a line at this level intersects the lines representing the fluxes and the shock front at the time of their arrival at z = 100.9 cm. The times of arrival are now read off giving Figure 8.2. This completes the first portion of the routing. If a slope were infinitely short, this input to the saturated layer would represent the slope hydrograph.

In the second part of Chapter 5, it was shown that the slope base hydrograph is given by Equation 4.44

$$q_L(x', t_L') = \frac{1}{t_L'} \int_{t_L'}^{t_L'} \dot{I}(0, t') \, dt'$$

this equation shows that the form of the slope-base hydrograph $q_L(x', t_L')$ will be given by integrating the input to the saturated layer $(I(x', t'))$ over a time period equivalent to the travel time in the saturated layer from the top of the hillside where

$$t_L' = \frac{L_s}{C_s} \text{ hours}$$

where

t_L' = time of travel (hr)

C_s = velocity of flow in saturated layer (cm/hr)

L_s = length of saturated path or slope length (cm)

We know from Equation 4.40

$$C_s = \frac{\rho_w \cdot g \cdot \beta \cdot k_s}{\mu \, \phi_e} \qquad\qquad 8.5$$

and since $k_s = 54.0 \times 10^{-6}$ cm^2, for slope 'A', $t_L' = 6.1$ hours.

The result of integrating the input to the saturated layer over 6.1 hours is shown in Figure 8.5. This is the predicted slope-base hydrograph. On site 'A' at this date, the upper third of the slope had little or no snow, so it is more realistic to smooth the input to the saturated layer over 4 hours rather than 6.1 hours. The result of doing this is also shown in Figure 8.5.

The same procedure as outlined for site 'A' was also applied to site 'C' on the same day (Figure 8.6). Using the parameters shown in Table 8.2, the analysis was applied to a series of days from the woods sites (Figures 8.7 to 8.17).

Results of the Application of the Runoff Model

In order to predict the slope-base hydrographs shown in Figure 8.5 to 8.17, values for the permeabilities of the unsaturated and the saturated layers of the snowpack had to be assumed. The value of the permeability for the unsaturated layer was taken as 6.0×10^{-6} cm^2, and that of the saturated layer as 54.0×10^{-6}. These two values affected the form of the predicted hydrograph a great deal.

The values of permeability assumed for the unsaturated layer affects the rate at which fluxes of water travel down through the snowpack. The effects of changing the permeability on the velocity of vertical travel of a flux are shown in Table 8.3. The effects are substantial.

FIGURE 8.5:

Snow Depth = 101 cm
Predicted Melt = 3.6 cm
Observed Melt = 3.2 cm

Predicted with travel time in the saturated layer = 4 hr.

Predicted with travel time in the saturated layer = 6 hr.

Observed

Time E.S.T.
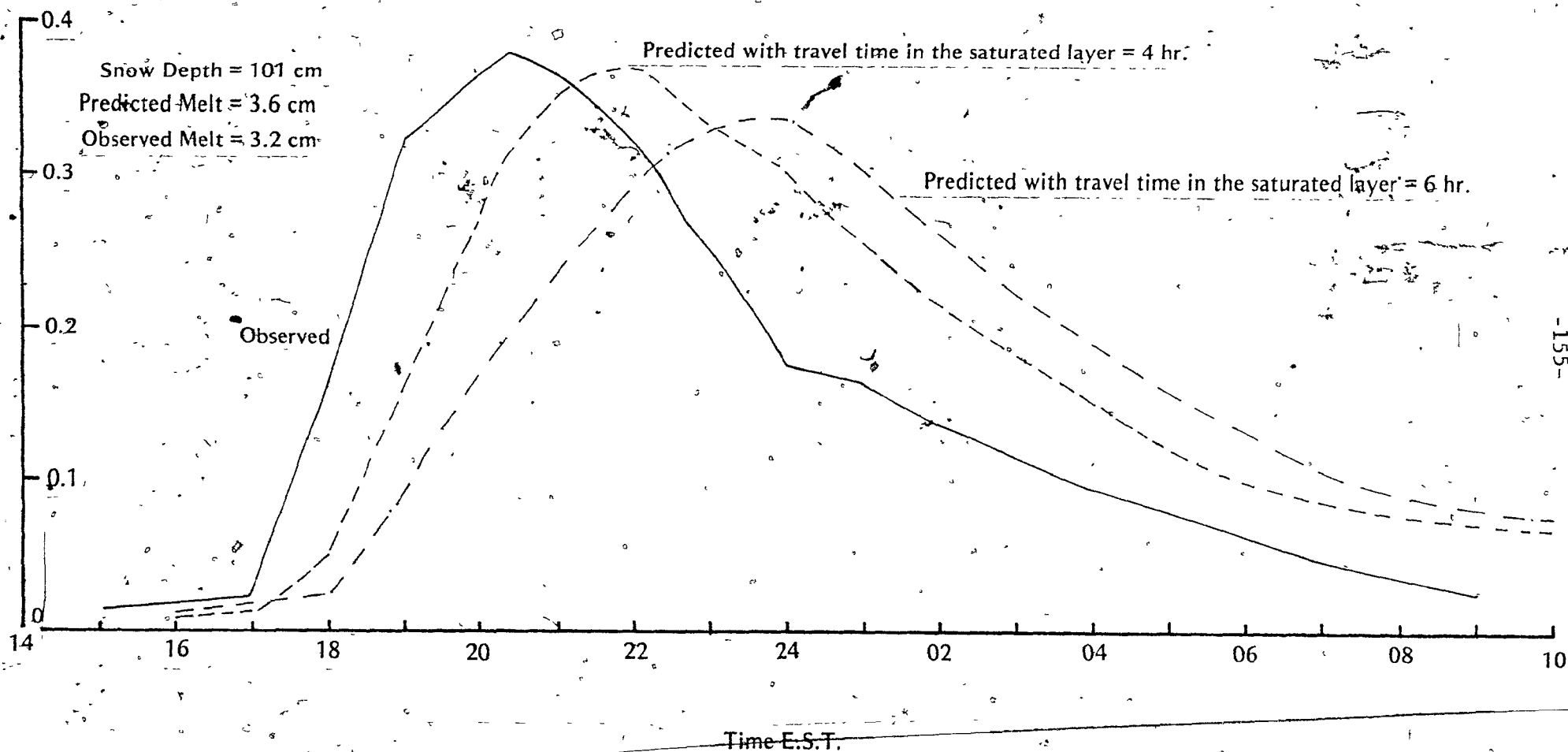
Predicted and Observed Hydrographs, Site 'A', May 16th, 1972

-155-

FIGURE 8.6

Snow Depth = 22 cm
Predicted Melt = 3.6 cm

Predicted

Observed

Discharge (cm/hr)

16/05/72

Time, E.S.T.

17/05/72

-156-
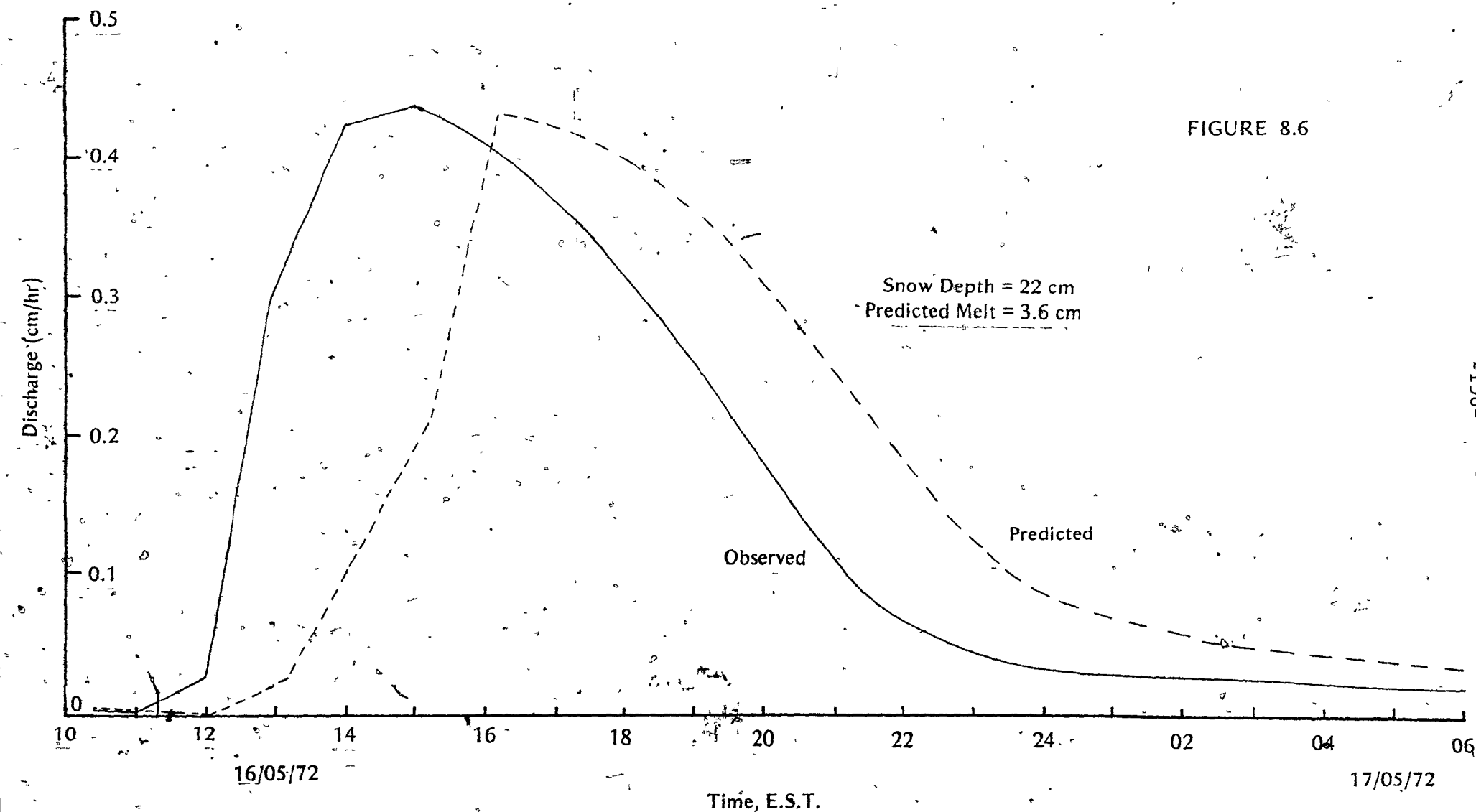
Predicted and Observed Hydrographs, Site 'C', May 16th, 1972
Peaks of Observed and Predicted Hydrographs tied.

Table 8.2

	Site	ϕ_e	k (cm^2)	k_s (cm^2)	L_s (m)	t'_L (h)
	A	.544	6×10^{-6}	54×10^{-6}	85	6.1
Tundra	B	.544	6×10^{-6}	54×10^{-6}	49	1.8
	C	.544	6×10^{-6}	54×10^{-6}	36.5	2.35
	D	.652	6×10^{-6}	54×10^{-6}	85	4.5
	E	.652	6×10^{-6}	54×10^{-6}	55	1.4
Woods	F	.652	6×10^{-6}	54×10^{-6}	61	4.2
	G	.652	6×10^{-6}	54×10^{-6}	76	4.1

Routing Parameters

FIGURE 8.7

Observed Hydrograph, Site 'E', May 16th, 1972, with Predicted Hydrographs at three depths.

Predicted Melt = 2.4 cm
Observed Melt = 2.5 cm (approx.)
Snow Depth = 56 cm (Site 'E')
Snow Depth = 130 cm (Site'F')

Predicted at 130 cm (Site F)

Predicted at 42 cm depth

Predicted at 56 cm depth

Observed

16/05/72

Time E.S.T.

17/05/72

FIGURE 8.8

Snow Depth = 22 cm
Predicted Melt = 3.1 cm
Observed Melt = 2.8 cm

Observed

Predicted

Discharge (cm/hr)

0.4

0.3

0.2

0.1

0

10   12   14   16   18   20   22   24   02   04

09/05/73   10/05/73

Time E.S.T.

Predicted and Observed Hydrographs, Site 'E', May 9th, 1973

-159-

Predicted and Observed Hydrographs, Site 'F', May 9th, 1973

FIGURE 8.10

Snow Depth = 69 cm
Predicted Melt = 3.1 cm
Observed Melt = 2.9 cm

Predicted

Observed

Discharge in cm/hr

0.4

0.3

0.2

0.1

0

-14   16   18   20   22   24   02   04   06   08

09/05/73   10/05/73

Time E.S.T.

−161−

Predicted and Observed Hydrographs, Site 'G', May 9th, 1973

FIGURE 8.11

Snow Depth = 89 cm
Observed Melt =1.9 cm.
Predicted Melt = 2.5 cm.

Predicted and Observed Hydrographs, Site 'D', May 8th 1973.

FIGURE 8.12
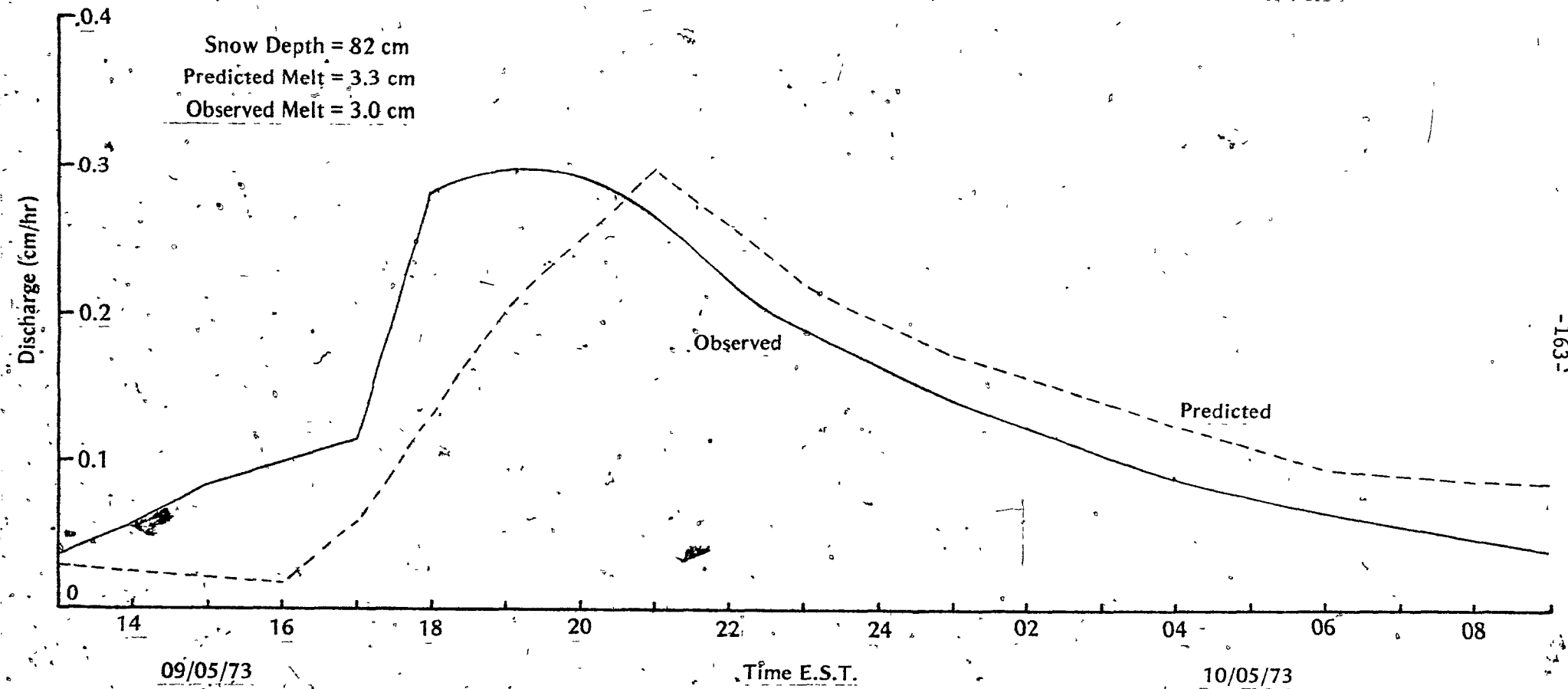
Predicted and Observed Hydrographs, Site 'D', May 9th, 1973

FIGURE 8.13

Snow Depth = 71 cm
Predicted Melt = 4.2 cm
Observed Melt = 4.2 cm
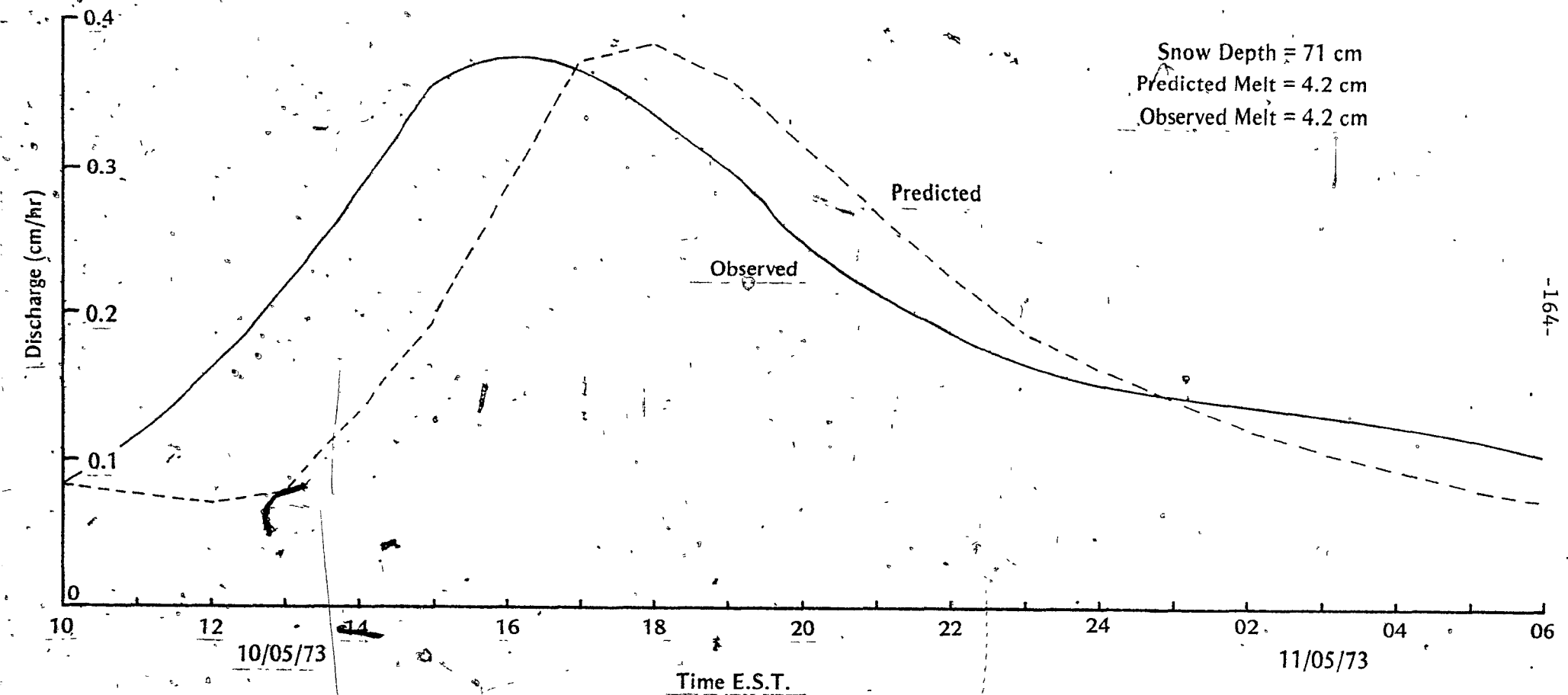
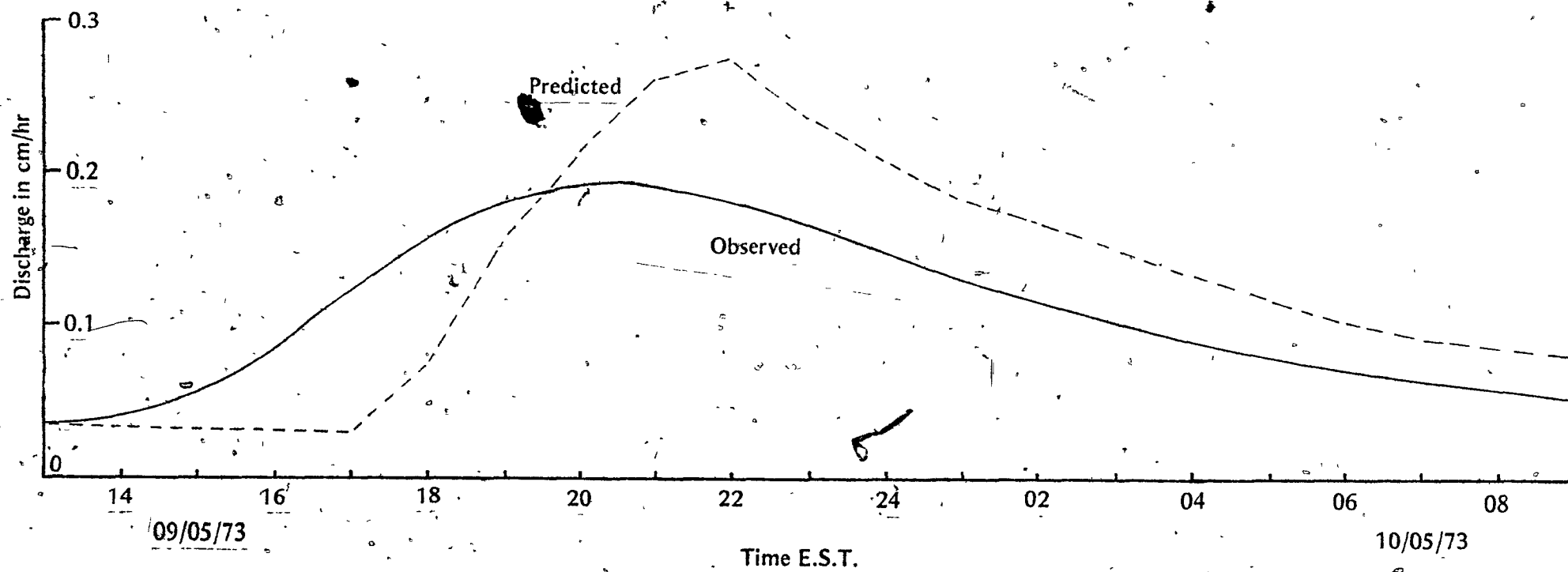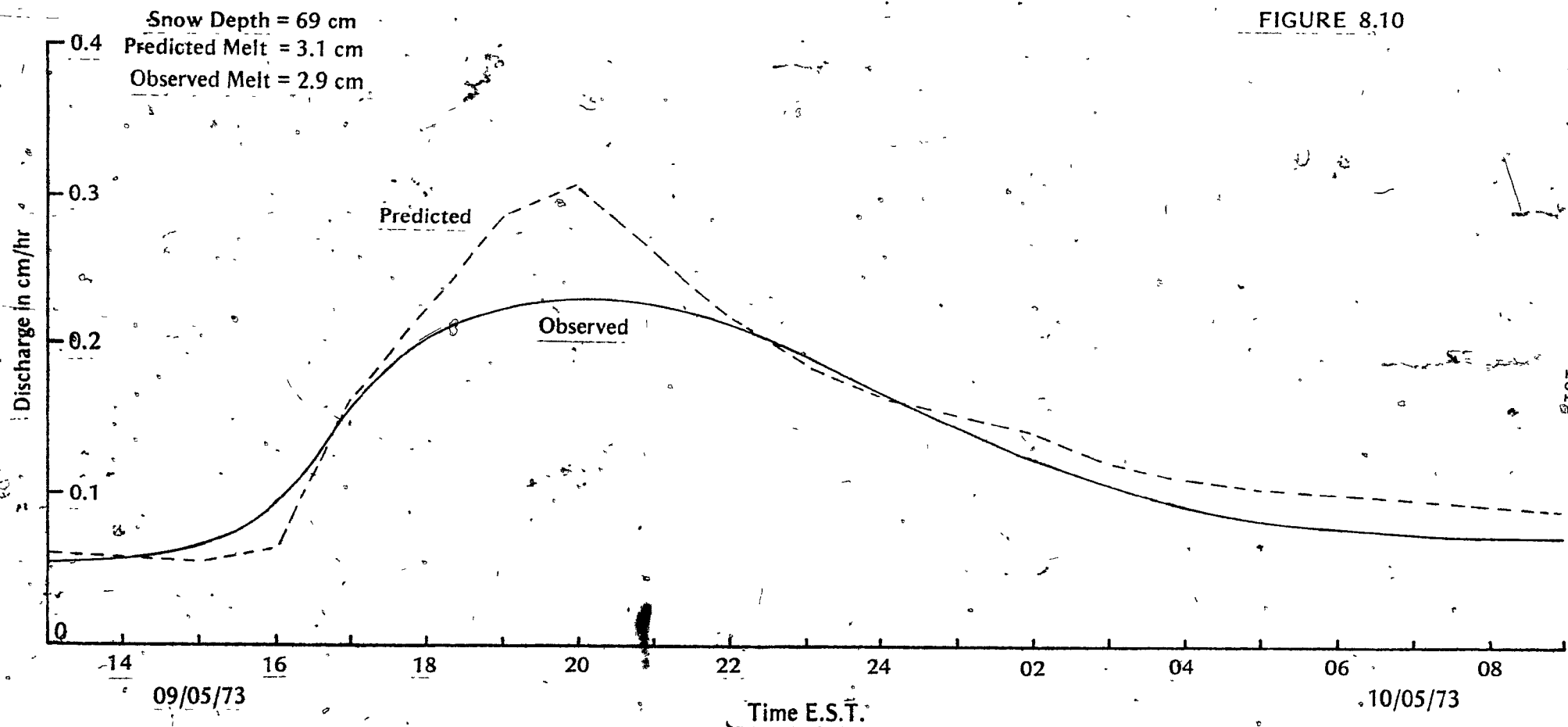Predicted and Observed Hydrographs, Site 'D', May 10th, 1973

-164-

FIGURE 8.14

Snow Depth = 58 cm

Predicted Melt = 3.9 cm

Observed Melt = 4.5 cm

Predicted using $z_0 = 0.015$ m

Observed

Predicted using $z_0 = 0.005$ m

Discharge (cm/hr)

0.4

0.3

0.2

0.1

0

10   12   14   16   18   20   22   24   02   04   06

11/05/73   12/05/73

Time E.S.T.

−165−
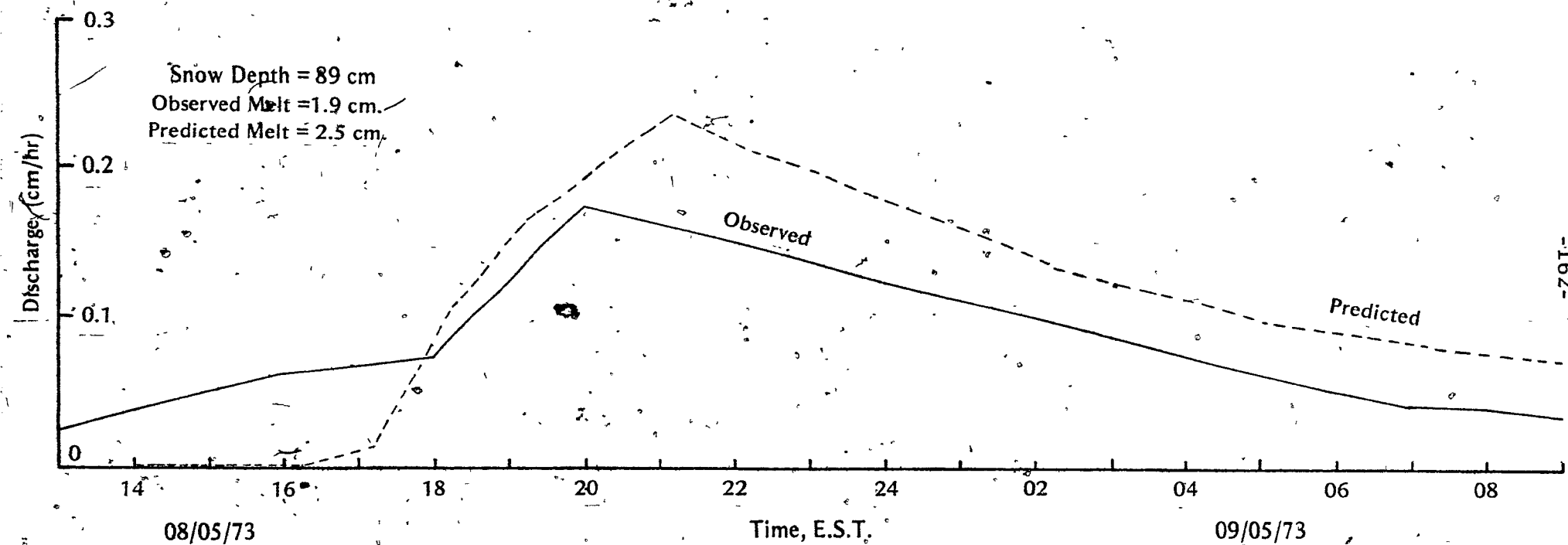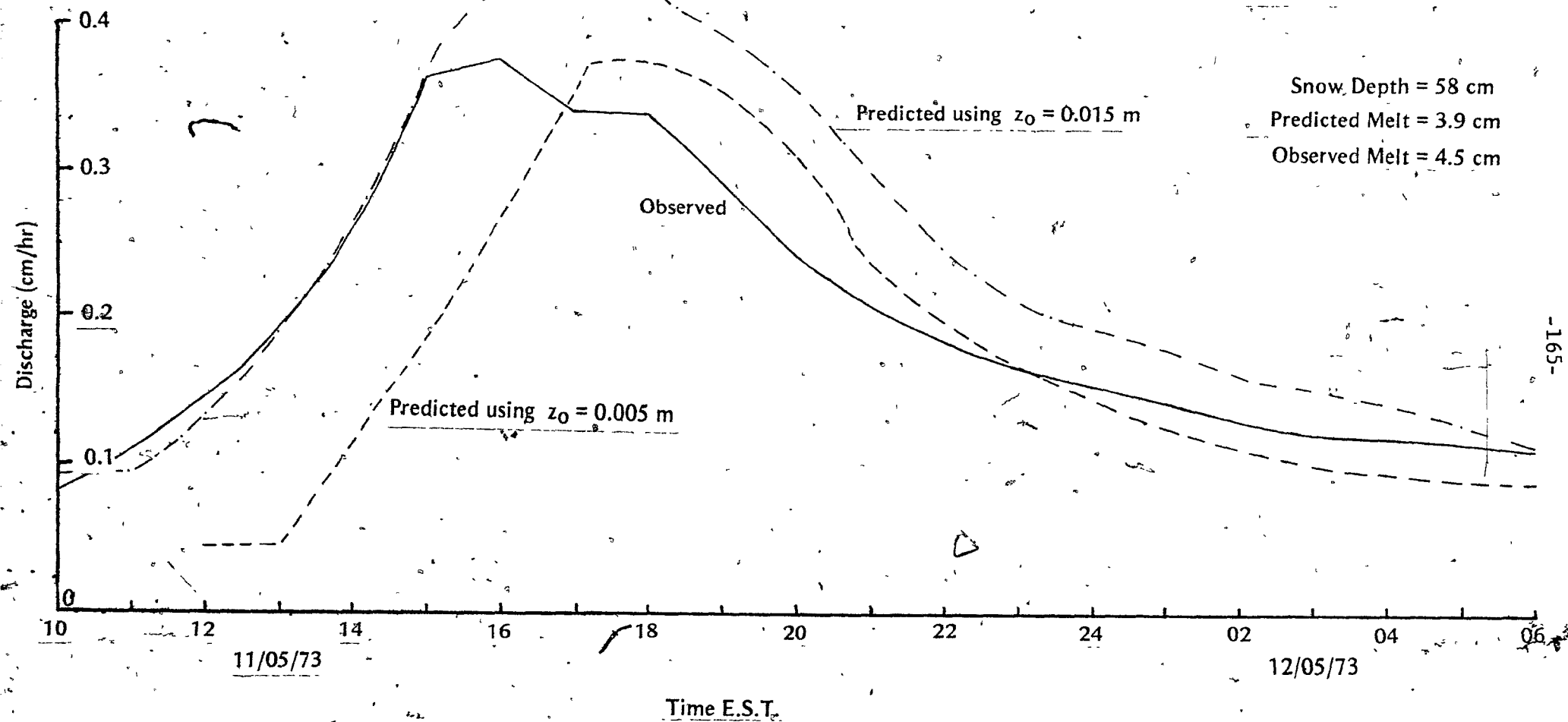
Predicted and Observed Hydrographs, Site 'D', May 11th, 1973
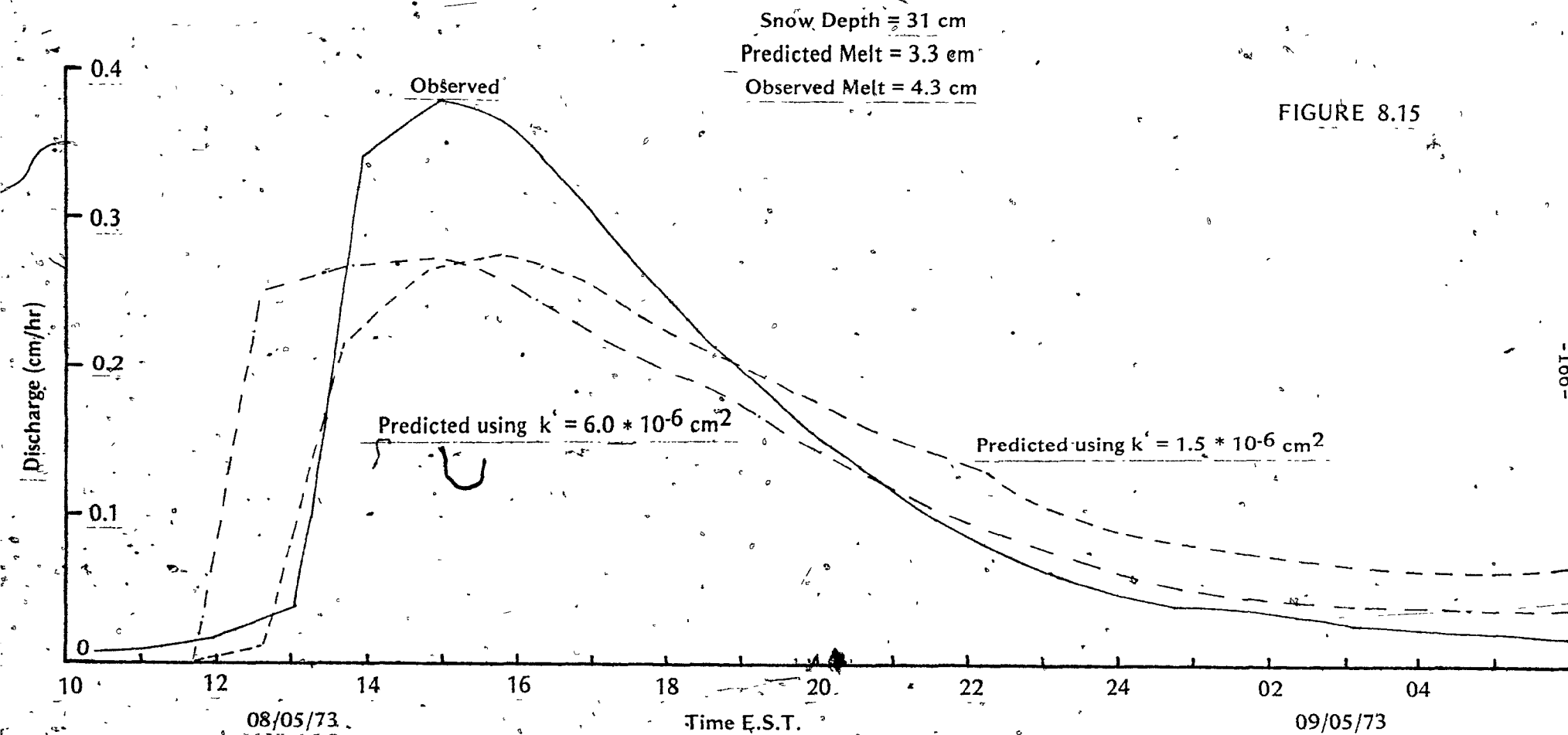
Predicted and Observed Hydrographs, Site 'E', May 8th,1973

FIGURE 8.16
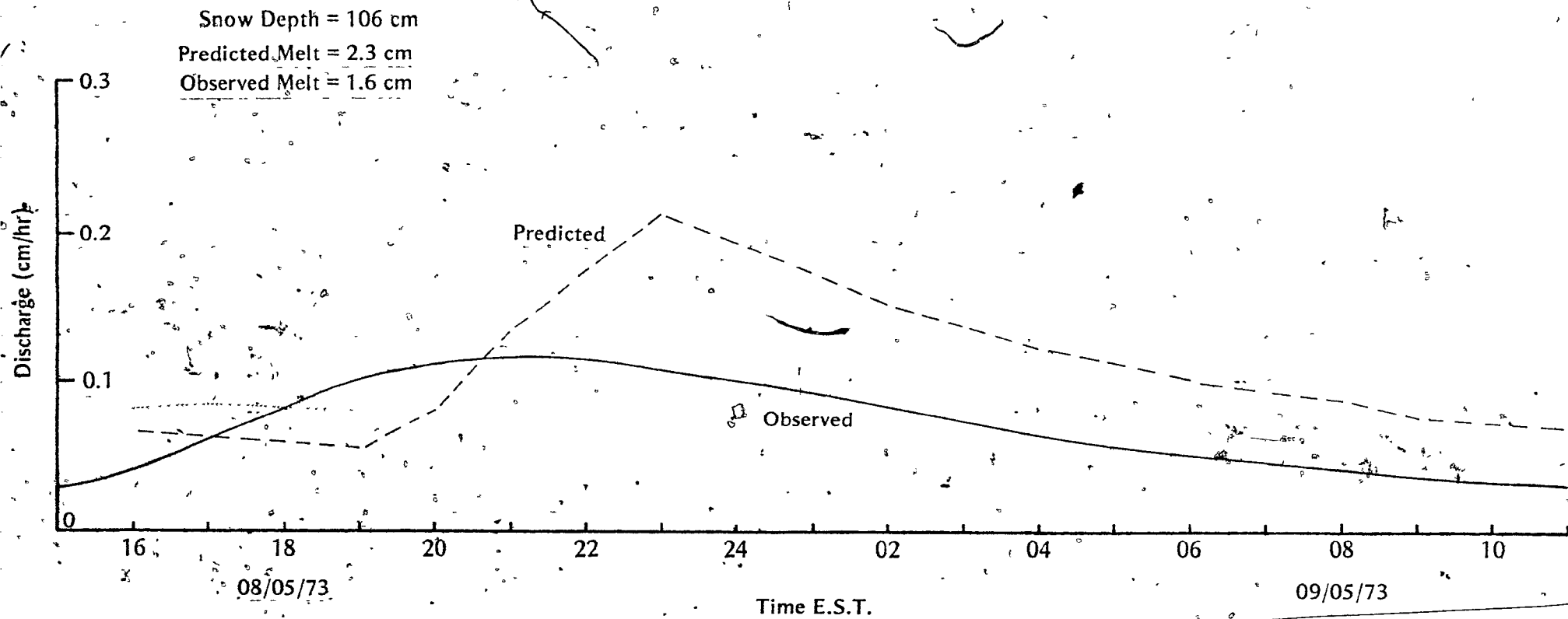
Predicted and Observed Hydrographs, Site 'F', May 8th, 1973

FIGURE 8.17

Snow Depth = 72 cm
Predicted Melt = 2.4 cm
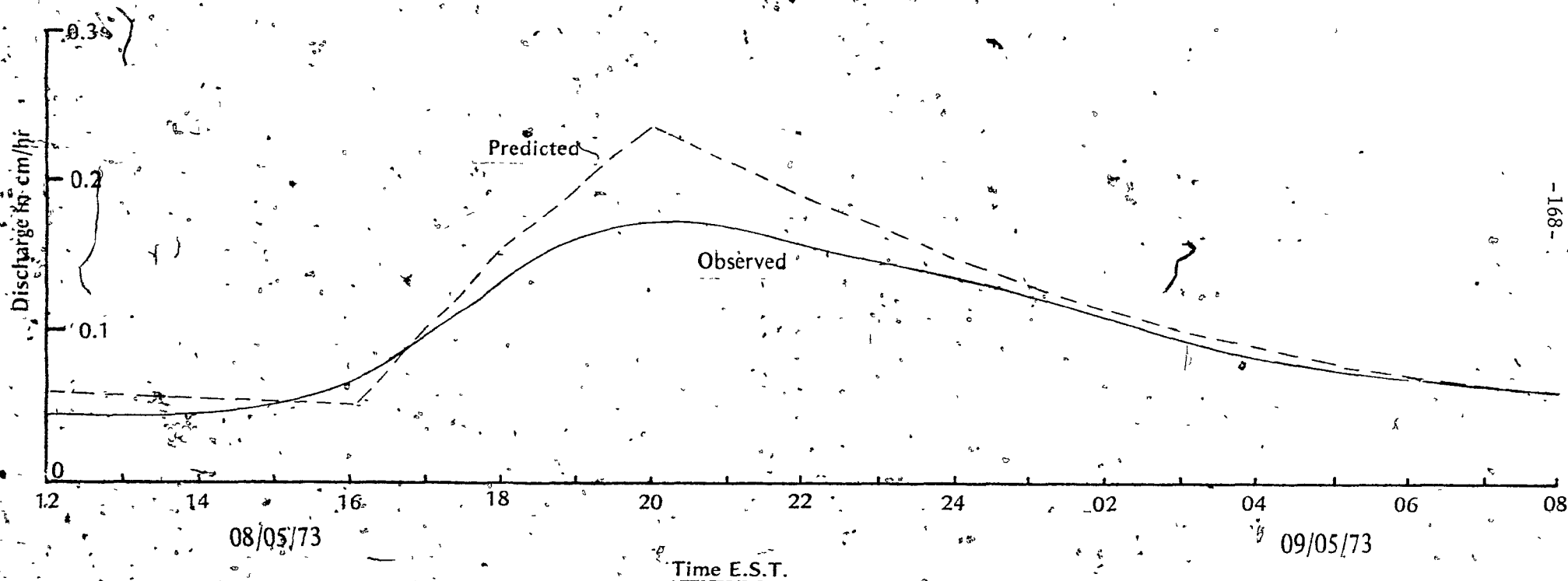Observed Melt = 2.3 cm

Predicted

Observed

Discharge in cm/hr

0.3

0.2

0.1

0

1.2   14   16   18   20   22   24   02   04   06   08

08/05/73

09/05/73

Time E.S.T.

Predicted and Observed Hydrographs, Site 'G', May 8th 1973

and it is easy to see that if Figure 8.4 were replotted using either the reduced or increased permeabilities, the resulting predicted flux at any level would be greatly changed.

The rate of vertical travel of the shock front ($\frac{d\xi}{dt}$) is also affected by the value of permeability (from Equation 8.4) as shown in Table 8.3. The changes in ($\frac{d\xi}{dt}$) caused by changes in permeability are also very large, and again would have profound effects on the form of the predicted input at any depth z.

Both ($\frac{d\xi}{dt}$) and ($\frac{dz}{dt}$) are affected by the estimate of effective porosity, ϕ_e (see Table 8.3). Since the estimates of density, and thus ϕ_e are quite precise, the probable limits within which ϕ_e could vary are relatively small, and thus the effects of ϕ_e on both ($\frac{d\xi}{dt}$) and $(\frac{dz}{dt})_{v_w}$ are small compared with the effects of changing permeability.

The value assumed for the permeability of the saturated layer is also important. It has been noted that the slope-base hydrograph is produced by integrating the input to the saturated layer over a time period equivalent to the time of travel through the saturated layer, such that (from Equation 8.5)

$$t'_L = \frac{L_s}{C_s} = \left[\frac{\mu \, L_s \, \phi_e}{\rho_w \cdot g \cdot k_s \cdot \beta} \right] \, hr \qquad 8.6$$

The value of t'_L will vary inversely with k_s. The effects of this are to increase or decrease the time span over which integration takes place (i.e. the interval t'_o to t'_L in Equation 4.44). As the integration interval increases, rates of rise and decline both decrease, and hydrographs become less peaked. Figure 8.5 shows the effects of increasing the permeability of the saturated layer by 50 percent.

Table 8.3

for V_w = 0.325 cm/hr

$\quad \phi_e$ = 0.652

k'	(dz/dt)(cm/hr)
6×10^{-6}	10.78
6×10^{-6}	23.00
60×10^{-6}	50.025

Effects of changing permeability on rate of propagation of flux $(\frac{dz}{dt})_{V_w}$

for V_w = .325

$\quad$ k' = 6×10^{-6}

ϕ_e	(dz/dt)
.552	26.54
.652	23.00
.752	19.46

Effects of changing porosity on rate of propagation of flux $(\frac{dz}{dt})_{V_w}$

for U_- = .025, U_+ = .325

$\quad \phi_e$ = .652

k' (cm^2)	dξ/dt (cm/hr)
6×10^{-6}	7.20
6×10^{-6}	15.37
60×10^{-6}	33.43

Effects of changing permeability on propagation of shock front $(\frac{d\xi}{dt})$.

Effects of Changing Parameters

The hydrograph using 4 hour smoothing has a higher peak, and quicker rates of increase and decline than the 6 hour smoothed hydrograph.

The general effects of the parameters discussed is as follows: higher unsaturated layer permeabilities give earlier, more rapid rates of rise, and peaked hydrographs. Lower values of k_s reduce the rates of rise, and delay the time of rise. High values of the saturated layer permeability give sharper, higher peaks, and low values of saturated layer permeability give flat-peaked hydrographs with slow rates of rise and fall. Any hydrograph is produced by a combination of these factors involving both the unsaturated and saturated layers.

The other variable which affects the form of the hydrographs is snow depth, this factor controls the time of rise, and the rates of rise and decline. Differences in snow depth also have a great effect on hydrographs produced by the same surface input.

A comparison of Figures 8:5 and 8.6 shows the effects of snow depth. On the tundra site 'C' Figure 8.6 peaks-earlier than 'A', since the snow depth is much greater on 'A'. The control of snow depth on time of peak can be seen by comparing Figure 8.5 with Figure 8.7 . On 'A' melting only commenced at 1100 EST, whereas on 'F' melting started at 0700 EST. Despite this 4 hour lead, 'F' still peaked 2 hours after 'A', as a result of greater snow depth. Figure 8.7 shows hydrographs produced by the same surface input at 42 cm depth, 56 cm, and 130 cm. The three hydrographs are quite distinct, and the 25% depth difference between 42 and 56 cm has a substantial effect on the timing of the predicted hydrograph.

A general consideration of differences between observed and calculated hydrographs shows that prediction is remarkably good. The worst predictions occur on days where the total volume of predicted melt is much lower than the observed melt. In Figure 8.16, the difference between calculated melt and observed melt is considerable (calculated is 30% greater than observed). This means that the surface fluxes from which the hydrograph is computed are in general 30% too high. This will lead to overestimation of the rate of travel of all fluxes, and also of the rate of propagation of the shock front. From the general remarks made earlier, this overestimate of fluxes should cause a more peaked hydrograph, peaking too early. This is the case in Figure 8.16, although the peak is not significantly early. In general the poorer predictions are on days where the predicted volumes are markedly greater than observed melt. Another case of this is Figure 8.11. Not only can the difference in total volume be clearly seen, but also the early rise and excessively peaked form.

A case of bad estimation of flux is also shown in Figure 8.14. In this case, calculated melt is too small. As was discussed in Chapter 7, there is some evidence that the estimation of heatflow may be corrected by using a larger z_0 value in the heatflow equations. Figure 8.14 shows the large differences between the two predicted hydrographs using two different surface fluxes, one with $z_0 = 0.005$ m, and one with $z_0 = 0.015$ m. It also shows clearly the much improved rising limb and peak timing prediction of the hydrograph produced using the modified surface flux, with $z_0 = 0.015$ m.

Figure 8.15 shows the effects of changing the unsaturated layer permeability from 6×10^{-6} cm^2 to 1.5×10^{-6} cm^2, a change well within the range of published values. The effect of this decrease can be seen in a later time of peak, and a less 'peaked' appearance. In the other cases (8.10, 8.17) better results would be obtained if the k' value were decreased, but there is no good a priori reason for doing this.

The form of the hydrographs is thus affected strongly by volume (and flux) prediction, by snow depth, by the unsaturated layer permeability, and by saturated layer permeability. Some of these factors, such as snow depth and permeability of the unsaturated layer, have similar effects, so that it is very difficult to separate the effects of different parameters.

However, it seems from the excellent form prediction on days when volume (and flux) predictions are good, that the model is a good description of the processes involved in the formation of snow melt hydrographs. The arguments outlined above emphasize the need for better knowledge of the snow properties, especially permeability, before better testing of the runoff model can be performed.

Another aspect of the model is that it postulates the existence of a saturated layer at the base of the snowpack. It predicts that this saturated layer showed increase in thickness downslope, and also fluctuates in thickness with time at a point. A saturated layer was observed in the field, and observations of it, given in Table 8.1 confirm

some of the predictions of the model. The measurements, both of crystal size and saturated layer thickness are somewhat equivocal, since both properties are extremely difficult to measure. Crystal boundaries are indefinite in both saturated and unsaturated zones, and it is very difficult to distinguish between grains and aggregates of snow crystals forming single grains. It is also difficult to measure the depth of the saturated layer. The layer is sometimes quite distinct as a black strip at the snow base, but in other cases the gradation between relatively dry snow and saturated snow is quite indistinct. The data do show, however, that the saturated layer tends to increase to a maximum in the middle of the day, and then to decrease later in the day, and also to increase with distance downslope at any one time in the day, which is what the model predicts.

The overall hydrograph prediction is good. Some low melt days on deep snowpacks show considerable differences between calculated and observed hydrographs, but these are attributable to the lack of permeability data. The excellent general similarity between the form of predicted and observed hydrographs suggests strongly that the model adequately explains the mechanisms involved in the forming of daily snow melt hydrographs.

CHAPTER 9

DISCUSSION OF RESULTS

Some suggestions have been made during the course of this study as to what measurements might improve the estimation of daily or hourly snowmelt. Some variables need not be so carefully measured - air temperature and vapour pressure, for example, were as well defined using a good hygrothermograph as by the use of an Assman aspirated psychrometer, and total global radiation measured with an actinograph proved to be extremely close to values derived from an Eppley solarimeter. In both cases in this study, results of the less sophisticated instrument were checked against those of the more sophisticated one, but results suggest that quality of the data was much the same in both cases. The mechanical instruments usually give a more complete record, since they are simpler and more reliable than electrical equipment.

The application of the regression lines developed between net radiation and global radiation seems to be an excellent technique, except during the final stages of melt. Under continuous snow conditions it makes the direct measurement of H_R unnecessary. In addition, the H_R versus (Q+q) lines when used in conjunction with the Garnier and Ohmura (1968) mapping technique, makes it possible to map net radiation. This spatial variation of H_R proved not to be of great importance in the Schefferville area, but could be extremely important in high radiation conditions. Two variables concerning the snow surface

should receive more attention. One is surface temperature. Snow surface temperature during the night was approximated by wet-bulb temperature, using observed times of surface freezing to fix the time when snow surface temperature ceased to be zero in the evening, and times of first observed thaw to fix the time the following-day when T_s again became zero.

The other snow surface variable somewhat neglected in this study is the roughness. The estimate of z_o made by the method of Lettau (1969) was probably good, since early predictions of daily melt were quite precise. The figure arrived at was the same as that used by Fohn (1973), and was within the usual range of figures. The roughness was qualitatively seen to change during the melt, and as demonstrated previously, probably accounts for much of the bad prediction of the heatflow model.

Another aspect of the energy balance which is ill-defined in this study is the ripening of the pack. Again, this problem could be overcome by measuring the snowpack temperature profile, to give an estimate of total pre-melt heat deficit.

The energy balance approach as used in this study is easy to use, given usually available meteorological data, and although daily totals show some unexplained patterns of over and under-prediction the general level of explanation is good. The corrections applied to the turbulent exchange terms in order to account for the modifying effects of stable air layers over the snow has been shown to make a great deal of difference to computed heatflows This better estimation of turbulent heatflows is

most important in view of the size of the turbulent exchanges at
Schefferville. Figure 9.1 shows the relative size of H_R, H_c and H_e
during two melt periods, óne at Schefferville, and one at the
Central Sierra Snow Laboratory (USACE, 1955), in the Sierŗás. Two
points should be made in comparing the two sets of data. First,
during the initial 6 days of melt at Schefferville the numerical
size of H_R, H_c and H_e are similar in pattern to the CSSL data,
with radiation dominant. The conditions between day 1 and day 6
were conditions of low vapour pressure and temperature, and so the
turbulent exchanges are small. Then, between days 6 and 7, a major
disturbance swept up from the Atlantic coast, bringing masses of
warm, moist air and windy conditions. This change in conditions
changes the proportions of melt caused by different factors com-
pletely, as can be seeñ from Figure 9.1. It should also be noted
that the generally low values of radiation at Schefferville are
caused mainly by cloudy conditions. The second point to be made
in reference to the differences between the Schefferville data
and the CSSL data is that even though conditions of melt may differ
greatly, either between areas or in the same area during one melt,
the physical model is sufficiently general to account for such
changes. This is an enormous advantage of the physical approach.

Another aspect of the energy balance approach which makes it
so useful in application is that because variations in radiation, and
windspeed may be defined, the spatial variation of energy input to
the snowpack may also be defined with some certainty. These local
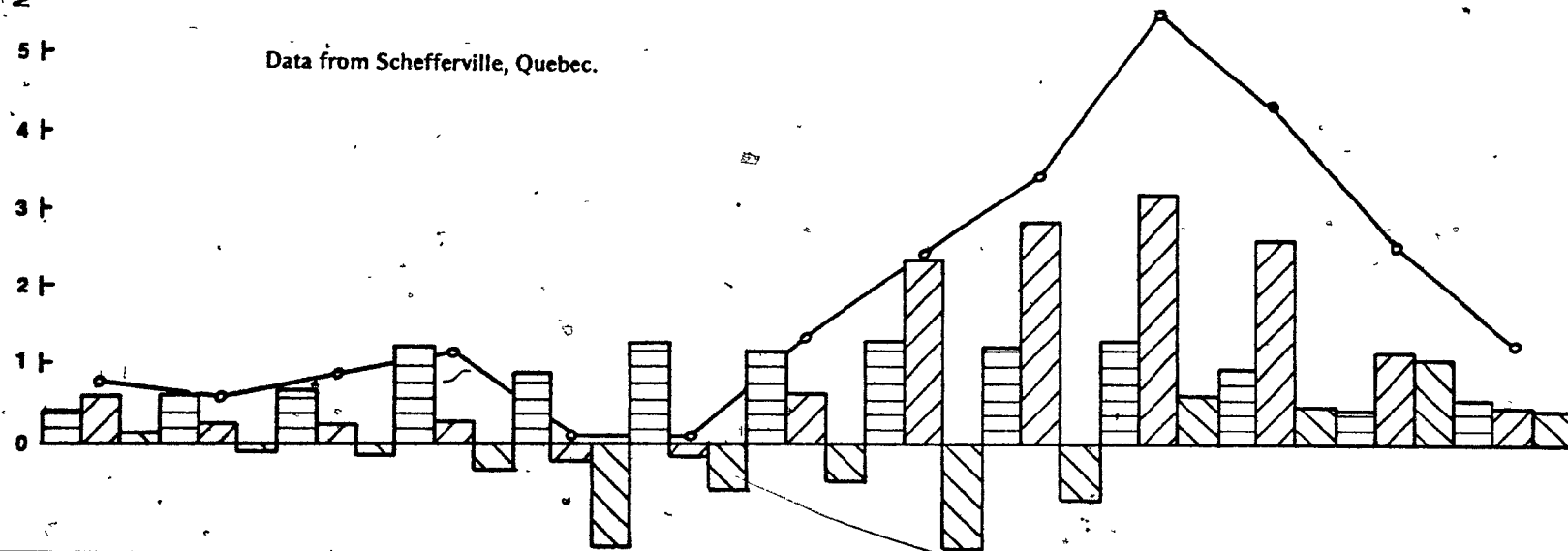
Comparative Snowmelt Data.

Data for Central Sierra Snow Laboratory
Soda Springs, California. (1955)

FIGURE 9.1

Total melt

1- Radiation melt
2- Sensible heat melt
3- Latent heat melt

Days into
melt season.
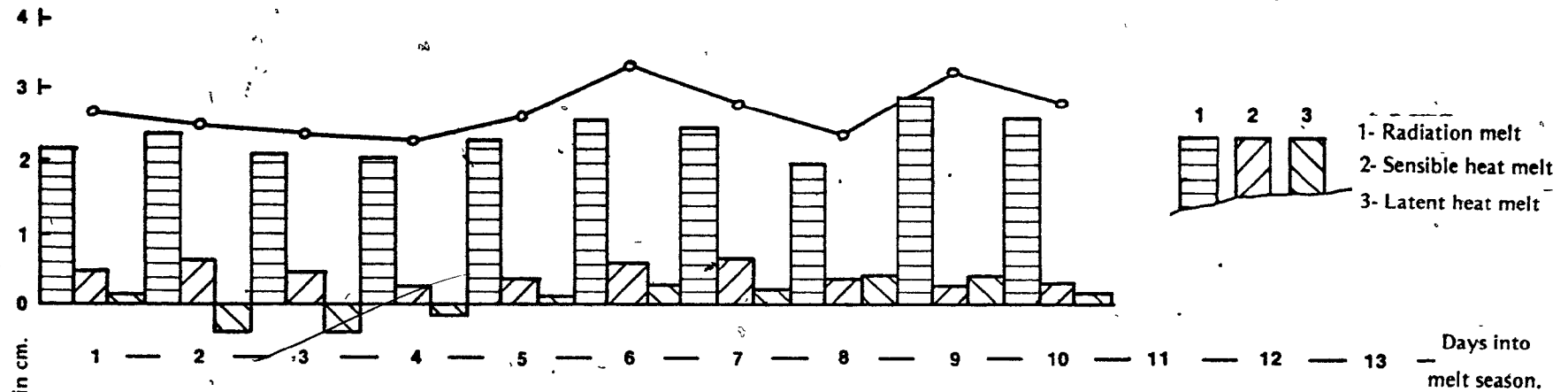
Data from Schefferville, Quebec.

variations in energy input to snow at thaw has been the object of some attention in recent snowmelt literature (Hendrick and Filgate, 1972). In many cases, differences may be very important, even though they were not in the Schefferville situation.

The prediction of hourly melt cannot be checked against direct measurements of runoff, but application of computed melts to runoff modelling gives good results. In addition the correspondence of daily sums of runoff with daily energy balance sums suggests that the estimates of hourly fluxes are good within relatively narrow limits. In any case, differences in timing of surface melt were as important for the routing exercise as were differences in volume, and differences in timing between slopes are well defined.

Further steps that should be taken in developing the energy balance approach include better definition of surface temperature and roughness, and a study of the effects on net radiation of vegetation and bare ground showing through the snow. This should also include the possible effects of ground absorption of radiation through the thinning snowpack.

The method used in the study for hydrograph prediction is important because it allows the prediction of snowmelt hydrographs at the slope scale. This is an obvious first step in the synthesis of snowmelt hydrographs for larger areas. The routing model is physically based, which makes it relatively simple to assess the importance of various factors in affecting the general form of hydrographs generated by daily melt cycles. There is, as mentioned above, some uncertainty about the value of the surface fluxes, and also the value of snow permeability is only an estimate, as is the

assumed value of 8% for the irreducible saturation. In addition to
these indirectly estimated variables, there are some assumptions im-
plicit in the use of the model which are known not to be true.

These are: (a) the assumption of constant snow depth

and ·(b) the assumption of constant slope .

Both of these assumptions are made in order to simplify the application
of the routing model to the field problem. It would be possible to
incorporate variations both in snow thickness and in slope angle into
the model, but this would be complex and time-consuming. Another assump-
tion made in the routing of the hydrographs is that flow in the saturated
layer is adequately described by Darcy's Law. Reynolds numbers computed
for the velocities of fluid flow encountered in the saturated layer place
the flow very near the laminar/turbulent transition zone (Todd, 1959).
Should higher velocities be the case, Darcy's Law would not describe the
flow adequately, but an alternative to Darcy's Law is not immediately
obvious.

Further improvement in hydrograph prediction would come from better
measurements of snow properties, in particular, measurement of the per-
meabilities of both the saturated and unsaturated layer. The value of k'
could be measured using the flux plates described in this study, and
saturated layer permeabilities possibly from dye tracing. In the case
of this study, infiltration was known to be insignificant, but the appli-
cation of the routing in other areas would require knowledge of the
infiltration rate.

In conclusion, it seems that the physically based models used in this work can be used with some success to describe the processes involved in the generation of snow melt hydrographs. Although the model does not explore such things as phase changes within the snowpack, crystal growth or changes in snow crystal structure, the treatment of the snowpack as a porous medium like other porous media sheds a great deal of light on the major controls of hydrograph generation, and indicates where the emphasis should be placed in further work.

REFERENCES

Anderson, E.A.
> 1968: Development and testing of snow pack energy balance equations.
> Water Resour. Res., 4(1), 19-37.

Bader, H.R., R. Haefeli, E. Bucher, J. Neher, O. Eckel, and C. Thams
> 1954: Snow and its metamorphism. U.S. Army Corps of Engineers,
> Snow, Ice and Permafrost Establishment, Translation 14,
> Willmette, Ill., 313 pp.

Bear, J., D. Zaslavsky, and S. Irmay
> 1968: Physical Principles of Water Percolation and Seepage. U.N.
> Educational, Scientific and Cultural Organisation, Paris.

Canadian National Committee for the International Hydrological Decade.
> 1968: Proceedings of the Workshop Seminar - Snow Hydrology.
> University of New Brunswick, Sept., 82 pp.

Colbeck, S.C.
> 1971: One-dimensional theory of water flow through snow. U.S.
> Army Cold Regions Research and Engineering Laboratory,
> Research Report 296.

> 1972: A theory of water percolation in snow. Jour. Glaciology,
> 11(63), 369-385.

> 1973: On predicting water runoff from a snow cover. U.S. Army
> Cold Regions Research and Engineering Laboratory, Research
> Note. Mimeographed, 11 pp.

> 1974: Water flow through snow overlying an impermeable boundary.
> Water Resour. Res., 10(1), 119-123.

Colbeck, S.C., and G. Davidson
> 1972: Water percolation through homogenous snow. Proceedings of
> the Symposium on the Role of Ice and Snow in Hydrology,
> Banff, Alta., Sept. WMO/UNESCO.

Collins, E.H.
> 1934: Relationship of degree-days above freezing to runoff.
> Trans. Amer. Geophys. Union, Part I, 624-629.

de La Casinière, A.C.
> 1974: Heat exchange over melting snow surface. Jour. Glaciology,
> 13(69), 55-72.

Dunne, T., and R. Black
> 1971: Runoff processes during snowmelt. Water Resour. Res.,
> 7(5), 1160-1172.

Fitzgibbon, J., and T. Dunne
    1973:   Photographic measurements of vegetation canopies for use
            in the computation of the radiation balance. Climatological
            Bull., 13, McGill University, Montreal, 8 pp.

Fohn, P.M.B.
    1973:   Short-term snowmelt and ablation derived from heat- and mass-
            balance measurements. Jour. Glaciology, 12(65), 275-289.

Garnier, B.J., and A. Ohmura
    1968:   Computation and mapping of the shortwave radiation on a slope.
            Jour. Applied Meteor., 2, 796-800.

Hendrick, R.L., B.D. Filgate, and W.D. Adams
    1971:   Application of environmental analysis to watershed snowmelt.
            Jour. Applied Meteor., 10(6), 418-429.

Ishida, T., and H. Shimizu
    1955:   Determination of the airflow resistance through a snow layer.
            Low Temperature Science Series, A14, 33-42.

Kuroiwa, D.
    1968:   Liquid permeability of snow. Low Temperature Science Series,
            A26, 29-52. (In Japanese with English summary).

Lettau, H.
    1969:   Note on aerodynamic roughness-parameter estimates on the
            basis of roughness-element description. Jour. Applied Meteor.,
            18(5), 828-832.

Light, P.
    1941:   Analysis of high rates of snow-melting. Trans. Amer. Geophys.
            Union, Part II, 195-205.

List, R.J. (editor)
    1966:   Smithsonian Meteorological Tables (Sixth Edition). Smith-
            sonian Institution, Washington, D.C., 527 pp.

Liu, B.Y.H., and R.C. Jordan
    1960:   The interrelationship and characteristic distribution of direct
            diffuse and total solar radiation. Solar Energy, 4(3), 1-19.

National Research Council
    1971:   Runoff from Snow and Ice - Hydrology Symposium No. 8.
            Associate Committee on Geodesy and Geophysics. Subcommittee
            on Hydrology, National Research Council of Canada, Ottawa,
            257 pp.

Nicholson, H.M.
    1973:   Pedological studies in a sub-arctic environment, Schefferville,
            Quebec. Unpublished M.Sc. Thesis, McGill University, Montreal,
            248 pp.

Petzold, D.E.
1974:   Solar and net radiation over snow. Climatological Research
        Series, 9, Dept. Geography, McGill University, Montreal,
        77 pp.

Petzold, D.E., and R.G. Wilson
1974:   Solar and net radiation over melting snow in the subarctic.
        Proceedings of the 31st. Eastern Snow Conference, Ottawa,
        Feb., 51-59.

Post, F.A., and F.R. Dreibelbis
1942:   Some influences of frost penetration and micro-climate on
        the water relationships of woodland, pasture and cultivated
        soils. Soil Science Soc. Amer., Proc., 7, 95-104.

Pysklywec, D.W., K.S. Davar, and D.I. Bray
1968:   Snowmelt at an index plot. Water Resour. Res., 4(5), 937-946.

Rose, C.W.
1966:   Agricultural Physics. Pergamon Press, London, 230 pp.

Scheidegger, A.E.
1957:   The Physics of Flow Through Porous Media. University of
        Toronto Press, Toronto, 236 pp.

Sellers, W.D.
1965:   Physical Climatology. University of Chicago Press, 272 pp.

Shimizu, H.
1970:   Air permeability of deposited snow. Low Temperature Science
        Series, A22, 1-32.

Szeicz, G., G. Endrodi, and S. Tajchman
1969:   Aerodynamic and surface factors in evaporation. Water Resour.
        Res., 5(2), 380-394.

Tajchman, S.
1971:   Evapotranspiration and energy balances of forest and field.
        Water Resour. Res., 7(3), 511-523.

Todd, D.K.
1959:   Groundwater Hydrology. John Wiley & Sons Ltd., London, 336 pp.

U.S. Geological Survey
1954:   Energy budget studies. U.S. Geol. Survey Prof. Paper, 296,
        300 pp.

U.S. Army, Corps of Engineers
1955:   Lysimeter studies of snowmelt. Snow Investigations, Research
        Note 25, 41 pp.

U.S. Army, Corps of Engineers
    1956:   Snow Hydrology: Summary Report of Snow Investigations.
            North Pacific Division, Portland, Oregon, 437 pp.

Viessman, W.
    1968:   The Synthesis of Snowmelt hydrographs. Snow Hydrology -
            Proc. Workshop Seminar, Can. National Comm. Int. Hydro.
            Decade, University of New Brunswick, 67-79.

Webb, E.K.
    1965:   Aerial microclimate. Amer. Meteor. Soc., Agricultural
            Meteorological Monographs, 6(28), 27-58.

    1970:   Profile relationships: the log-linear range and extension
            to strong stability. Quart. Jour. Roy. Meteor. Soc., 96,
            67-90.

Wilson, W.T.
    1941:   An outline of the thermodynamics of snowmelt. Trans.
            Amer. Geophys. Union, Part I, 182-195.